

# **Sum Frequency Generation Imaging Microscopy: Factor Analysis of Mixed Monolayers**

**By  
Aleksandr A. Pikalov**

**A Dissertation submitted to the Department of Chemistry,  
College of Natural Sciences and Mathematics  
in partial fulfillment of the Requirements for the degree of**

**Doctor of Philosophy**

**in Chemistry**

**Chair of Committee: Steven Baldelli**

**Committee Member: Shoujun Xu**

**Committee Member: Vassiliy Lubchenko**

**Committee Member: Chengzhi Cai**

**Committee Member: Laurent Pirolli**

**University of Houston  
December 2019**

“I want to know how God created this world.  
I am not interested in this or that phenomenon,  
in the spectrum of this or that element.  
I want to know His thoughts; the rest are details.”

**-Albert Einstein**

## ACKNOWLEDGEMENTS

I would like to thank my adviser Steve Baldelli for his long patience, guidance, and caring advice. His jokes lightened up my mood during difficult times and his critiques helped me deepen my understanding of science. I would also like to thank all previous and current members of the Baldelli group for all their support.

I especially would like to express my gratitude to Ming for the many hours he invested teaching me the ins and outs of the SFG microscope and to Dien for his advice and support using the factor analysis technique. Special thanks to Daniela for supplying the critical compounds for the experiments and reviewing my drafts, and to Shah for always taking care of the laser and OPG/OPA alignment for everyone's use.

Many thanks to my parents Anatoliy and Vera for their prayers and support.

This work is dedicated with great love and gratitude to my caring and loving wife Inna, my help meet, and my beloved children Timothy, Ephraim, Marita, Sarah, Nina, Jonathan, and Benjamin. None of this would have been possible without their love, support and great sacrifice.

Throughout my whole life and especially during graduate studies I saw the hand of God led and support me. All the achievements of my life are the result of the great love and mercy of my Heavenly Father, which He has bestowed upon me. All praise and glory belongs to Him.

## ABSTRACT

Surfaces and interfaces are considered as a boundary between a material and its surrounding environment and influence interactions with that environment. In order to gain a fundamental understanding of the underlying processes, it is critically important to know the chemical and physical properties of the surfaces or interfaces. To investigate surface properties, while controlling the surface chemically and spatially, a model system of multi-component patterned self-assembled monolayers (SAMs) with different terminal functional groups were produced by microcontact printing. The microcontact patterned self-assembled alkanethiol monolayers on gold surfaces were analyzed by sum frequency generation imaging microscopy (SFG-IM) technique to generate SFG images. The SFG-IM provides identity of surface molecular species, information about surface chemical structure, and spatial distribution overview of chemicals on the surface, which make it a useful technique in chemical imaging. The SFG images were then analyzed by factor analysis utilizing a library consisting of SFG alkanethiol spectra to determine the chemical identity and spatial distribution of the patterned monolayers over the images. By utilizing the spectral library as a target test for factor analysis, the monolayers were correctly identified and their spatial distributions were mapped. By analyzing a random pattern sample, factor analysis was able to identify an unknown monolayer region, vibrational spectra of which was not present in the target library. Additionally, it was determined by target factor analysis that the amount of solution deposited backfill mixing into the microcontact stamped region and the absorption kinetics correlate with previous studies. The 12 percent backfill monolayer mixing into the stamped monolayer region, quantified by target factor analysis, results are representative of low concentration solution studies. These results demonstrated the capability of factor analysis combined with the alkanethiol library to determine the chemical composition and spatial

distribution of alkanethiol monolayers on the surface of multi-component chemical system  
acquired by SFG-IM.

## Table of Contents

<b>EPIGRAPH</b>	ii
<b>ACKNOWLEDGMENTS</b>	iii
<b>ABSTRACT</b>	iv
<b>LIST OF FIGURES</b>	ix
<b>1 Introduction</b>	1
<b>2 Theoretical and Experimental Background</b>	7
2.1. SFG background	7
2.2. Picosecond PL2251 Ekspla laser	9
2.3. Optical parametric generator/amplifier (OPG/OPA)	10
2.4. 1064 nm, infrared and guide beam paths to SFGIM	11
2.5. Sum frequency generation imaging microscope	13
2.6. SFGIM signal collection	15
2.7. Factor analysis	18
2.8. Data processing	21
2.9. Microcontact printing	24
<b>3 Sum Frequency Generation Imaging Microscopy of Self-Assembled Monolayers on Metal Surfaces: Factor Analysis of Mixed Monolayers</b>	27
3.1. Introduction	27
3.2. Theoretical background	29
3.2.1. Sum frequency generation	29
3.2.2. Factor analysis	29
3.3. Experimental	30
3.3.1. Sample patterning by microcontact printing	30
3.3.2. Sum frequency generation imaging microscope	31

3.3.3. SFG image data processing with PFA and TFA application	31
3.4. Results and discussion	32
3.4.1. SFG imaging of ODT—MeOHT sample	32
3.4.2. Two component maps	34
3.4.3. Analysis of 5000 shots per image ODT—MeOHT sample	36
3.4.4. Analysis of ODT—MeOHT sample obtained with 500 laser shots per image	40
3.4.5. Analysis of ODT—Fluoro-ODT sample	43
3.5. Conclusion	46
<b>4 Multicolor Chemical Imaging by Sum Frequency Generation Imaging Microscopy of Monolayers on Metal Surfaces</b>	<b>49</b>
4.1. Introduction	49
4.2. Theoretical background	51
4.2.1. Sum frequency generation	51
4.2.2. Factor analysis	51
4.3. Experimental	52
4.3.1. Materials and sample preparation	52
4.3.2. Sum frequency generation imaging microscope	54
4.3.3. SFG image data processing with target factor analysis	54
4.4. Results and discussion	55
4.4.1. Five component patterned sample	57
4.4.2. Random pattern three component sample	60
4.5. Conclusion	65
<b>5 Quantification of Self-Assembled Monolayers by Sum Frequency Generation Imaging Microscopy: Factor Analysis</b>	<b>76</b>
5.1. Introduction	66

5.2. Experimental	68
5.2.1. Materials and sample preparation by microcontact printing	68
5.2.2. SFG image data processing with target factor analysis	69
5.3. Results and discussion	71
5.3.1. Mixing in stamped region	72
5.3.2. Effects of backfill time on mixing	74
5.4. Conclusion	75
<b>Bibliography</b>	76
<b>Appendix A Factor Analysis Codes</b>	90
A.1. Principle factor analysis	91
A.2. Target factor analysis	93
A.3. Loading factor analysis	95
A.4. Other MATLAB codes	97
A.4.1. Remove first line of .txt	97
A.4.2. Data matrix	98
A.4.3. Target test matrix	99
A.5. Data analysis	100
A.5.1. Spectra extraction from SFG images for data matrix and test target matrix	100
A.5.2. Data matrix and target test matrix construction in MATLAB	105
A.5.3. Data matrix analysis by significant factor analysis (sfa)	107
A.5.4. Generation of abstract factors from data matrix	108
A.5.5. Data matrix analysis by target factor analysis (tfa)	111
A.5.6. Chemical image construction by loadings factor analysis (lfa)	111
<b>Appendix B Supporting Information for Sum Frequency Generation Imaging Microscopy of Self-Assembled Monolayers on Metal Surfaces: Factor Analysis of Mixed Monolayers</b>	115

## List of Figures

2-1.	The optical layout of EKSPLA PL2251 laser head.	10
2-2.	Optical layout of LaserVision OPG/OPA system.	11
2-3.	Illustration of the 1064 nm and IR beam paths for the SFG imaging microscope.	12
2-4.	Illustration of the guide beam path for the SFG imaging microscope.	13
2-5.	SFG imaging microscope illustration.	14
2-6.	Princeton Instrument PI-MAX4 iCCD detector.	15
2-7.	Quantum Efficiency curve of the PI-MAX4 Gen III HRf intensifier. The circle indicates the quantum efficiency at 810 nm.	16
2-8.	LabView program for wavenumber range and tuning rate control of OPG/OPA.	17
2-9.	Outline of target transformation of abstract factors into real factors by TFA. The real factors are obtained by adding the factors obtained by PFA using various weightings of the factors.	20
2-10.	Image Spectra Extraction code used for spectral extraction from ROIs.	22
2-11.	Illustration of the microcontact printing process.	24
2-12.	Schematic diagram of the preparation procedure of the five component patterned sample.	26
3-1.	ODT–MeOHT sample SFG images at (a) 2810 $\text{cm}^{-1}$ (b) 2875 $\text{cm}^{-1}$ , (c) 2950 $\text{cm}^{-1}$ (d) MeOHT SFG spectrum, (e) SFG spectrum of ODT stamped region.	33
3-2.	ODT—MeOHT sample SFG images acquired with (a) 5k shots per image at 2875 $\text{cm}^{-1}$ and (b) 0.5k shots per image at 2875 $\text{cm}^{-1}$ . PFA resulting maps of 6.5-by-6.5 $\mu\text{m}$ ROI (c) 5k shots per image 2 <sup>nd</sup> abstract factor and (d) 0.5k shots per image 3 <sup>rd</sup> abstract factor.	35
3-3.	MeOHT and ODT chemical maps. (a) MeOHT using 2.5-by-2.5 $\mu\text{m}$ ROIs (b) MeOHT from 6.5-by-6.5 $\mu\text{m}$ ROIs (c) ODT using the 2.5-by-2.5 $\mu\text{m}$ ROIs (d) ODT from 6.5-by-6.5 $\mu\text{m}$ ROIs. Note: data matrix containing the 2.5-by-2.5 $\mu\text{m}$ ROIs was too large for the computer calculations as a whole. It was divided into six equal fractions and TFA calculations were performed on each individually. The TFA results were then combined to produce the final images shown in (a) and (c).	37

<b>3-4.</b>	First and second abstract factors from row matrix (a, b) and column matrix (c, d) obtained by PFA of ODT—MeOHT sample data matrix.	38
<b>3-5.</b>	Resulting SFG spectrum of ODT and MeOHT after normalized ODT SFG spectrum was subtracted from the normalized MeOHT SFG spectrum and compared with the second abstract factor obtained from PFA.	39
<b>3-6.</b>	500 shot ODT—MeOHT sample SFG images at (a) 2810 $\text{cm}^{-1}$ (b) 2875 $\text{cm}^{-1}$ and TFA resulting maps of 6.5-by-6.5 $\mu\text{m}$ ROI (c) MeOHT and (d) ODT.	41
<b>3-7.</b>	First three abstract factors from row matrix (a-c) and column matrix (d-f) obtained by PFA of 500 shot ODT—MeOHT sample data matrix.	42
<b>3-8.</b>	(a) ODT and FODT molecular structure. ODT—FODT sample SFG (b) spectra and (c) image at 2875 $\text{cm}^{-1}$ and (d) 2880 $\text{cm}^{-1}$ with 5000 shots.	43
<b>3-9.</b>	First three abstract factors from row matrix (a-c) and column matrix (d-f) obtained by PFA of ODT—FODT sample data matrix.	45
<b>3-10.</b>	(a) First abstract factor compared with SFG spectrum of ODT, (b) resulting SFG spectrum of ODT and FODT after normalized FODT SFG spectrum was subtracted from the normalized ODT SFG spectrum compared with the third abstract factor obtained from PFA.	46
<b>4-1.</b>	Schematic diagram of the preparation procedure of the (a) five component patterned sample and (b) random pattern sample.	53
<b>4-2.</b>	(a) SFG spectra of octadecanethiol (ODT), 16-methoxy-hexadecane-1-thiol (MeOHT), 16,16-difluoro-octadecane-1-thiol (H2FODT), 16-phenyl-hexadecane-1-thiol (PhHDT), m-1-carboranethiol (M1CT), and bare Au compared to averaged SFG signal, and (b) respective MeOHT, ODT, PhHDT, H2FODT, and M1CT alkanethiol structures.	56
<b>4-3.</b>	SFG spectra overlaid with the corresponding target transformed spectra predicted by TFA (a) ODT, (b) MeOHT, (c) H2FODT, (d) PhHDT, (e) M1CT, and corresponding re-constructed TFA chemical images of (f) ODT, (g) MeOHT, (h) H2FODT, (i) PhHDT, and (j) M1CT.	58
<b>4-4.</b>	Normalized SFG spectrum (a), averaged over the full image, and images of the five component sample at (b) 2805 $\text{cm}^{-1}$ , (c) 2850 $\text{cm}^{-1}$ , (d) 2870 $\text{cm}^{-1}$ , (e) 2950 $\text{cm}^{-1}$ , and (f) 3060 $\text{cm}^{-1}$ .	59
<b>4-5.</b>	SFG spectra overlaid with the corresponding target transformed spectra predicted by TFA (a) ODT, (b) MeOHT, (c) H2FODT, (d) PhHDT, (e), M1CT and	62

	corresponding reconstructed TFA chemical images of (f) ODT, (g) MeOHT, (h) H2FODT, (i) PhHDT, and (j) M1CT.	
<b>4-6.</b>	Normalized SFG spectrum (a) averaged over the full image, and images of the random pattern sample at (b) 2805 cm <sup>-1</sup> , (c) 2870 cm <sup>-1</sup> , and (d) 2950 cm <sup>-1</sup> .	63
<b>4-7.</b>	(a) SFG spectrum extracted from the border region of the random pattern sample and (b) SFG image at 2850 cm <sup>-1</sup> . (c) Border region SFG spectra overlaid with the corresponding target transformed spectra predicted by TFA and (d) corresponding chemical map.	64
<b>5-1.</b>	Illustration of image stacking and spectra extraction from ROIs.	70
<b>5-2.</b>	ODT-MeOHT mixed sample SFG images at (a) 2810 cm <sup>-1</sup> (b) 2875 cm <sup>-1</sup> , (c) 2945 cm <sup>-1</sup> (d) MeOHT SFG spectrum, (e) ODT SFG spectrum.	71
<b>5-3.</b>	SFG spectra of stamped ODT and solution deposited MeOHT, and stamped ODT pure, without backfill.	72
<b>5-4.</b>	(a) SFG spectra of patterned sample extracted from ROI (b) Component weight of MeOHT in ODT stamped region.	73
<b>5-5.</b>	(a) SFG spectra of time varied backfill and (b) the TFA results.	74
<b>A-1.</b>	Image Spectra Extraction code used for spectral extraction from ROIs.	100
<b>A-2.</b>	ImageJ Stack Reverser Plugin used for image stack reversing.	101
<b>A-3.</b>	ImageJ image spectra extraction code	102
<b>A-4.</b>	ImageJ (a) Spectral Microscopy Plugin, (b) starting energy, (c) step size selection, and (d) brightness and contrast (B&C) adjustment.	103
<b>A-5.</b>	Region of interest (ROI) was selected using selection tools.	104
<b>A-6.</b>	ImageJ (a) spectra extraction using Gen Spectrum function and (b) obtaining a list of wavenumber–intensity values.	105
<b>A-7.</b>	Matrix construction using MATLAB EDITOR.	106
<b>A-8.</b>	Adding the factor analysis code to Path in MATLAB.	107
<b>A-9.</b>	Application of sfa on data matrix.	108
<b>A-10.</b>	Application of singular value decomposition to obtain abstract factors of data matrix.	109

<b>A-11.</b>	Steps to visualize the decomposed abstract factors of ‘u’ matrix.	109
<b>A-12.</b>	Steps to select abstracts factors from ‘v’ matrix.	110
<b>A-13.</b>	Reconstruction of abstract factor to generate distribution map.	110
<b>A-14.</b>	Application of target factor analysis (tfa) on data matrix.	111
<b>A-15.</b>	Steps to visualize the decomposed abstract factors of ‘u’ matrix.	112
<b>A-16.</b>	Application of lfa on data matrix.	112
<b>A-17.</b>	Steps to select predicted components from ‘loadings’ matrix.	113
<b>A-18.</b>	Steps to produce component distribution map of selected component.	114
<b>B-1.</b>	Illustration of image stacking and spectra extraction from 50-by-50 pixels ROIs. The SFG images are arranged into a stack according to decreasing IR wavenumber after which it is cut into user specific region of interest (ROIs) size and vibrational spectra is extracted from each respective ROI.	116
<b>B-2.</b>	SFG spectra of ODT and MeOHT extracted from 500 shots per image 6.5-by-6.5 $\mu\text{m}$ ROI.	117
<b>B-3.</b>	100 shot ODT—MeOHT sample SFG images at (a) 2810 and (b) 2875 $\text{cm}^{-1}$ .	117
<b>B-4.</b>	First five abstract factors from row matrix (a-e) and column matrix (f-j) obtained by PFA of 100 shot ODT—MeOHT sample data matrix. The first two abstract factors resemble the combined average of the ODT and MeOHT SFG signal response on gold substrate with the beam profile. Abstract factors 3 through 5 resemble some change to the average spectra. None of the abstract factors resembles the difference spectra of ODT and MeOHT peak positions.	118
<b>B-5.</b>	Outline of target transformation of abstract factors into real factors by TFA. The real factors are obtained by adding the factors obtained by PFA using various weightings of the factors.	119
<b>B-6.</b>	Stamped ODT, backfilled MeOHT SFG spectra, and the difference of the two regions (backfilled – stamped).	120

## Chapter 1: Introduction

Surfaces and interfaces are present everywhere we look around us. They are considered as a boundary between materials or a material and its surrounding environment, which influence interactions with that environment. At the molecular level, the surface or interface atoms, the top 1-10 atomic layers, experience a different chemical and physical environment than atom in the bulk.<sup>1-2</sup> Atoms inside the bulk are surrounded on all sides by other atoms of the same material, while, surface and interface atoms are surrounded by the same atoms on one or two sides but different atoms, or nothing, on the other. Every day phenomena like corrosion, friction, adhesion, tarnishing of metals, conductivity, lubrication of moving parts, and surface tension are influenced by surface properties.<sup>3-4</sup>

A common assumption in surface chemistry was that surfaces and interfaces are spatially homogeneous. More recently, researchers have realized that many surfaces are spatially inhomogeneous. The spatial surface heterogeneity is either natural, an inherent property of the material, or induced by surrounding environmental factors. As a result, this will affect the physical and chemical properties of the surface. These microscopic changes can have macroscopic effects that can be observed by changes in temperature, pressure, concentration, or reaction kinetics. Since surfaces and interfaces play an important role in many of the chemical, physical, and biological processes, it is critically important to gain a fundamental understanding of the underlying processes of chemical and physical properties and also to be able to distinguish and characterize the heterogeneity of the studied surface.

Heterogeneous or patterned surfaces have been characterized by many techniques, but each technique has its advantages and disadvantages.<sup>5</sup> X-ray photoelectron spectroscopy (XPS) can probe the chemical composition, oxidation state and can also provide coverage and thickness of

SAMs.<sup>6-7</sup> Secondary Ion Mass spectrometry (SIMS) provides surface chemical composition and bonding information about surface monolayer while low energy electron diffraction (LEED) gives surface structure information, but both are limited to ultra-high vacuum (UHV) conditions.<sup>8-9</sup>

Scanning probe microscopy techniques, scanning tunneling microscopy (STM) and atomic force microscopy (AFM), are used to determine the 2D structure of SAMs in UHV, liquids and ambient conditions. These techniques show the spatial structures of the monolayers but require other techniques, such as vibrational spectroscopy, to determine the molecular composition of the surface.<sup>10</sup> Vibrational microscopy techniques such as Fourier transform infrared (FT-IR), Raman, stimulated Raman scattering (SRS), and coherent anti-stokes Raman scattering (CARS) microscopies can provide spatial structures and chemical information.<sup>11-19</sup> The limitation of these techniques as surface microscopy techniques is that they are not interface specific and monolayer sensitive, and cannot distinguish surface from bulk signal.

Sum frequency generation (SFG) spectroscopy is a second-order, non-linear technique that provides vibrational spectra of the molecules at the interface.<sup>10, 20</sup> Chemical identification, molecular orientation, monolayers' conformational order, and vibrational dynamics can be studied by SFG spectroscopy.<sup>21-22</sup> This technique is very useful in providing information about the interfacial structure of a surface. However, SFG typically only provides the average information of the sampled area and does not show local characteristics due to the spatial averaging.

The sum frequency generation imaging microscopy (SFG-IM) technique, based on SFG, provides chemical images of the surface.<sup>23-26</sup> The chemical contrast is based on the vibrational frequencies of the adsorbed molecules on the surface. It can be used successfully to probe in-situ the solid-liquid, solid-gas, liquid-liquid, and liquid-gas interfaces. The advantage of using SFG-IM to study patterned surfaces is that it not only provides identity of interface molecular species,

and information about interface chemical structure, but it also provides spatial distribution overview of chemicals on the surface, which make it a useful technique in chemical imaging.<sup>24, 27-</sup>

28

The SFG process is achieved by spatially and temporally overlapping two incident beams, usually a visible and a tunable mid-infrared (IR) beam, which generates a new beam, which is at the sum of the two incident frequencies.<sup>10</sup> The vibrational spectra of the molecules on the surface is obtained by scanning the IR wavelengths. The intensity of the SFG signal enhances when the frequency of the IR incident beam is in resonance with the vibrational mode of a surface molecule. The SFG signal is collected by a charge-coupled device (CCD) camera, which allows spatial analysis of the surface.

To investigate heterogeneous/patterned surface properties, model systems such as self-assembled monolayers (SAMs) have been utilized.<sup>29-31</sup> A self-assembled monolayer is an organized layer of organic molecules adsorbed on a substrate surface. The molecular self-assembly is a spontaneous self-organization of amphiphilic molecules on surfaces into well-ordered arrays. The molecules that form SAMs are composed of three parts, a 'headgroup', 'spacer' and a 'tailgroup'. The hydrophilic 'headgroup' is a functional group that has a strong chemical affinity and binds to the substrate surface. The 'spacer' is often composed of an alkyl chain and is important for the self-assembly process due to van der Waals interactions.<sup>32</sup> The 'tailgroup' is oriented away from the surface of the substrate and being exposed to the environment, controls the surface properties. The interface properties can be controlled by changing the headgroup, spacer, and tailgroup of the SAMs.<sup>33-34</sup>

Alkanethiols are one of the most studied SAMs. These alkanethiol SAMs are easy to prepare, they are molecularly ordered and are robust under many conditions of use. The alkanethiol

SAMs are typically prepared by solution deposition. A common solvent for alkanethiol SAMs preparation is ethanol. The self-assembly begins once the metal substrate is submerged in a dilute solution of alkanethiol. A well-formed thiol monolayer requires a period of 12-48 hours.

In order to control the surface chemically and spatially, patterned systems of mixed SAMs have been utilized. These patterned SAMs systems have been produced by many different techniques like microcontact printing, photolithography, lift-off-lithography and ink-jet printing. Microcontact printing ( $\mu$ CP) is a form of soft lithography method that uses a polydimethylsiloxane (PDMS) stamp to form patterns of SAMs on the metal surface in a patterned and controlled fashion. The advantage of using PDMS is that it absorbs SAMs onto its surface and releases them during stamping. It is also nontoxic, commercially available, compatible with wide variety of organic and organometallic molecules and unreactive towards most chemicals.

The SAMs patterns are generated by 'inking' the surface pattern of the PDMS stamp with a SAM and printed on the metal surface. The SAMs are transferred from the stamp onto the region that comes into contact with the stamp, while unstamped region remain bare. The bare regions can be stamped by a different terminal functional group or backfilled by solution deposition of SAMs. By using multiple stamps, it is possible to pattern by multiple different SAMs simultaneously.

Metal surfaces patterned by  $\mu$ CP, by two different terminated functional groups alkanethiol SAMs have been successfully studied by SFG-IM previously.<sup>24-25, 28, 34-36</sup> The observed SFG image contrast of the patterned thiols was due to the different vibrational modes of the terminal functional groups of the thiols. Analyzing the SFG vibrational spectra of different regions-of-interests (ROIs) of the image, the identity and orientation of the functional groups can be determined. The SFG image analysis have been performed by fitting the spectra and constructing chemical maps based

on the fitting results. Spectral fitting requires sufficient signal-to-noise ratio of the individual spectra. This limits the spectral curve-fitting to larger ROIs or longer signal acquisition times.

Chemometrics and analytical techniques, such as partial least squares, principal component analysis, multivariate analysis, and factor analysis, have been utilized in spectral and image analysis in many spectroscopic techniques.<sup>37-45</sup> Factor analysis (FA) is a statistical method that uses mathematical procedures to investigate whether a number of observed variables are linearly related to some smaller number of unobservable factors. Application of FA in chemistry has been pioneered by Malinowski in 1980s.<sup>37</sup> The FA method has been applied in Raman spectroscopy, infrared spectroscopy, nuclear magnetic resonance, mass spectrometry, to determine reaction mechanics, kinetics, and the number and identities of components in a series of related multicomponent mixtures.<sup>37-41, 46-53</sup>

In order for a data set to be factor-analyzable, each data point in the matrix must be some linear sum of product terms. The first step in factor analysis is principal factor analysis (PFA) which utilizes singular value decomposition (SVD) to decompose the data matrix into abstract factors. Singular value decomposition is often used in a wide array of application such as data reduction, compressing, and denoising. The matrix decomposition produces abstract factors that are considered to contain no physically meaningful information. Since the results produced by SVD are purely mathematical, a transformation of the abstract factors is required, which is the second step is FA, called target factor analysis (TFA). The transformation is achieved by first testing known targets to find a target that is a real component of the data matrix, which then can be used to determine the correct linear combination of the abstract factors need to produce physically meaningful results. Utilizing correct targets in combination with the right number of abstract factors, vibrational spectra and chemical maps of the analyzed sample can be predicted.

The goal of the work outlined in this dissertation is to provide a chemometrics approach to SFG–IM data analysis. In Chapter 2 a short background theory on SFG and factor analysis are given, including descriptions of the laser system, SFG microscope and experimental sample preparation procedures. Chapter 3 lays out the framework for the application of FA on SFG images of two component patterned alkanethiol monolayer on gold by  $\mu$ CP. The focus was to investigate the application of FA on SFG images and to assess the chemical maps and abstract factors produced by FA. Chapter 4 expands the investigation of FA application on SFG images to multi–component patterned and random pattern systems to determine the chemical identities and spatial distributions of the monolayers. Chapter 5 focuses on the quantification of SAMs mixing into  $\mu$ CP regions and the absorption kinetics of mixing from data obtained by SFG–IM and analyzed by FA.

## Chapter 2: Theoretical and Experimental Background

### 2.1. SFG background

Sum frequency generation (SFG) spectroscopy is a second-order nonlinear optical process that is generated by two high-energy laser beams mixing at an interface.<sup>20</sup> In a typical SFG system, a fixed visible beam and a tunable IR beam are used to generate the SFG beam but for the SFG microscope system utilized here, a fixed 1064 nm fundamental beam was used. The reason for utilizing 1064 nm beam instead of a visible beam is due to the signal detector's higher sensitivity in the visible wavelength range compared to 1064 nm. The SFG process is achieved when a laser pulse of fixed wavelength of 1064 nm ( $\omega_{1064nm}$ ) overlaps with a tunable wavelength infrared pulse ( $\omega_{IR}$ ) at a surface and interact with the molecules on the surface. This interaction induces a nonlinear polarization of the molecules,<sup>21, 54</sup>

$$E_{SF} = P_{SF}^{(2)} = \epsilon_0 \chi^{(2)} : E_{1064nm} E_{IR} \quad (2.1)$$

which generate the sum frequency output beam at the frequency of the sum of the tunable infrared wavelength and the fixed 1064 nm beam frequencies,  $\omega_{SF} = \omega_{1064nm} + \omega_{IR}$ . The second-order nonlinear polarization is the product of the second-order susceptibility,  $\chi^{(2)}$ , the electric vacuum permittivity,  $\epsilon_0$ , and the electric fields of the 1064 nm and IR beams,  $E_{1064nm} E_{IR}$ , shown in Equation 2.1. In order to achieve SFG, spatial and temporal overlap of the IR and 1064 nm beams on the surface is essential. A coherent SFG signal is generated at a specific angle,  $\theta_{SF}$ , from the surface normal, which can be calculated using the conservation of momentum of all three beams parallel to the interface given by:<sup>55</sup>

$$n_{SF}\omega_{SF} \sin \theta_{SF} = n_{1064nm}\omega_{1064nm} \sin \theta_{1064nm} + n_{IR}\omega_{IR} \sin \theta_{IR} \quad (2.2)$$

where  $n$  is the refractive index of the medium through which the relevant beam propagates, and  $\theta$  is the angle to the surface normal of each beam.

The SFG intensity is proportional to the square of the induced polarization:<sup>10, 21, 56-57</sup>

$$I_{SF} \propto |P^{(2)}|^2 \propto |\chi_{eff}^{(2)}|^2 I_{1064nm} I_{IR} \quad (2.3)$$

where  $\chi_{eff}^{(2)}$  is the second-order nonlinear effective susceptibility and  $I_{1064nm}$  and  $I_{IR}$  are the intensities of the respective electric fields. The effective susceptibility,  $\chi_{eff}^{(2)}$ , relates the interface response to the input light fields and consists of resonant susceptibility,  $\chi_{res}^{(2)}$ , and a nonresonant susceptibility,  $\chi_{nr}^{(2)}$ . The nonresonant susceptibility arises from the nonresonant background response of the metal surface to the input beams. The resonant susceptibility arises from the response of the molecules on the surface and contains the vibrational information,<sup>21</sup>

$$\chi_{res}^{(2)} = \sum_q \frac{A_q}{(\omega_{IR} - \omega_q - i\Gamma_q)} \quad (2.4)$$

where  $\omega_{IR}$  and  $\omega_q$  refer to the frequency of the incoming infrared and  $q^{\text{th}}$  vibrational normal mode, respectively, and  $\Gamma_q$ , the damping constant for the corresponding  $q^{\text{th}}$  vibrational mode. The  $A_q$  term contains information on the Raman and IR transition moments.<sup>21, 58-59</sup> In order for SFG signal to be generated the vibrational mode must be Raman and IR active. When the IR frequency is at a resonance frequency of one of the vibrational modes, this results in an enhanced SFG signal. Plotting the SFG intensity as a function of the IR wavenumber results in a vibrational spectrum.<sup>10,</sup>

60

The SFG signal acquired is a convolution of the resonant and nonresonant susceptibilities of the surface. Since the susceptibilities are complex quantities, the overall SFG signal is dependent on the non-resonant susceptibility,  $\chi_{nr}^{(2)}$ , of the substrate, the resonant susceptibility,  $\chi_{res}^{(2)}$ , of the molecules on the surface, and the cross-term,

$$I_{SF} \propto |\chi_{eff}^{(2)}|^2 \propto \left| \chi_{nr}^{(2)} e^{i\varepsilon} + \chi_{res}^{(2)} e^{i\delta(\omega_{IR})} \right|^2 \quad (2.5)$$

$$|\chi_{eff}^{(2)}|^2 = |\chi_{nr}^{(2)}|^2 + |\chi_{res}^{(2)}|^2 + 2|\chi_{nr}^{(2)}||\chi_{res}^{(2)}|\cos[\varepsilon - \delta(\omega_{IR})] \quad (2.6)$$

where  $\varepsilon$  is the fixed nonresonant phase, which varies little with IR frequency, but is dependent on the intrinsic properties of the metal substrate, and  $\delta(\omega_{IR})$  is the resonant phase, which is IR frequency dependent. Due to the electronic nature, gold substrate exhibits a relatively larger non-resonant signal compared to the resonant signal.<sup>61</sup> The observed magnitudes of the spectral peaks or dips are governed by the convolution of all the terms and highly dependent on the relative phases. The signal magnitude of the first two terms is positive, while the cross-term may be positive or negative. A positive cross-term results in a spectral peak and negative cross-term results in a spectral dip. Therefore, the relative phase difference in the cross-term between the susceptibilities, and metal substrate properties give rise to peaks, dips or semi-interference peaks or dips.<sup>62-64</sup>

## 2.2. Picosecond PL2251 Ekspla laser

An EKSPLA PL2251 series laser was employed for SFG imaging. The laser system used a passive mode-locked neodymium-doped yttrium aluminum garnet (Nd:Y<sub>3</sub>Al<sub>5</sub>O<sub>12</sub>, Nd:YAG) picosecond-pulsed laser with a fundamental output of 1064 nm to generating pulses of 20-30 picoseconds. It generated a maximum energy output of about 40 mJ to pump the optical parametric generation and optical parametric amplification system (OPG/OPA) with a repetition rate of 20 Hz. This laser was composed of a laser head (PL2251A-20-G-X), a power supply (PS5050) and a cooling unit (PS1222CO).<sup>65</sup>

The three main parts of the laser head are the master oscillator, regenerative amplifier, and power amplifier, as shown in Figure 2-1. The master oscillator generates the fundamental 1064 nm beam using a 808 nm diode pumped Nd:YVO<sub>4</sub> laser material to seed the regenerative amplifier stage. The seed beam is amplified inside the cavity of the regenerative amplifier using a diode

pumped Nd:YAG rod. After reaching maximum amplification, the pulse is sent out of the regenerative amplifier cavity into the power amplifier where it is further amplified using a flash lamp pumped Nd:YAG rod. A detailed description of the EKSPILA laser system is found elsewhere.<sup>66</sup>

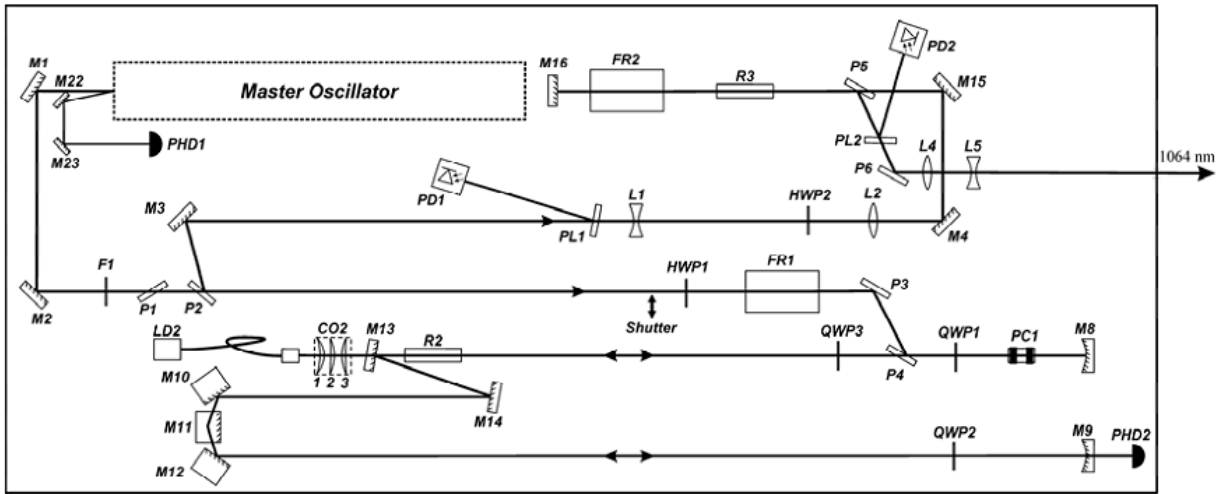


**Figure 2-1.** The optical layout of EKSPILA PL2251 laser head.<sup>65</sup>

### 2.3. Optical parametric generator/amplifier (OPG/OPA)

The fundamental 1064 nm beam from the Ekspla Nd:YAG laser was split into two beams using a 90:10 split ratio beam splitter (BS1). The beam containing 90% energy was sent into the optical parametric generator/amplifier (OPG/OPA), which was built by LaserVision, Inc.<sup>67</sup> The OPG/OPA was utilized to generate a tunable infrared laser pulse from 2000  $\text{cm}^{-1}$  to 4000  $\text{cm}^{-1}$  as shown in Figure 2-2.<sup>68</sup> This process was achieved by sending the 1064 nm beam through a beam splitter (BS2), where one part of the beam was used for the difference frequency generation process, and the other part was used to generate a 532 nm beam using a potassium titanyl arsenate (KTA) crystal. The 532 nm beam was split into two beams using beam splitter (BS3), where one

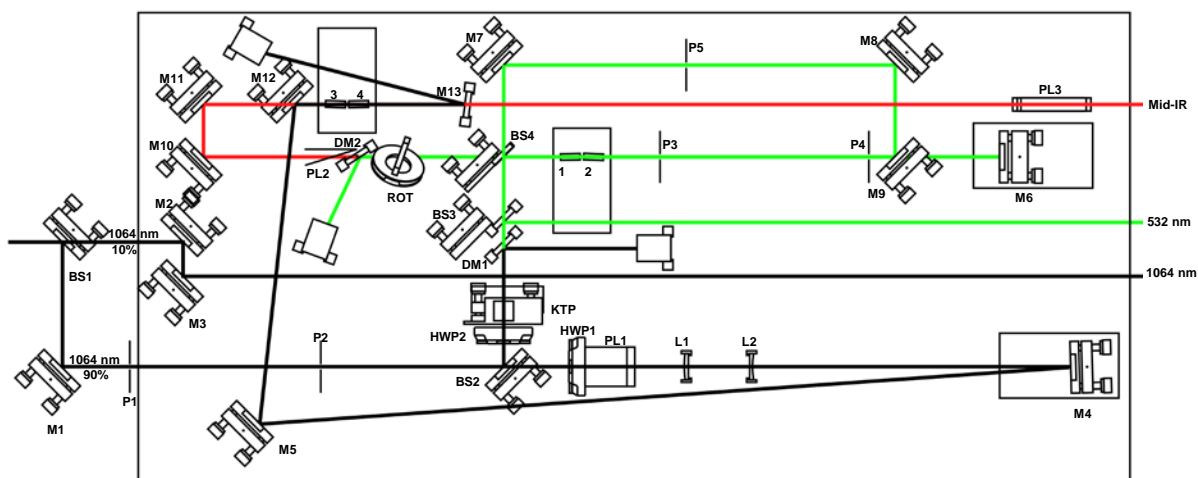


**Figure 2-2.** Optical layout of LaserVision OPG/OPA system.

part of the beam was sent to the first stage of the OPG/OPA, and the other part of the beam was used as a fixed visible beam.

The 532 nm beam that was sent to the first stage of the OPG/OPA was split again by beam splitter (BS4). One beam was sent through two potassium titanyl phosphate (KTP) crystals (1 and 2) to generate the signal and idler beams, while the other beam went through a delay stage and recombined with the idler beam for amplification of the signal beam. After the first stage, the signal beam was directed to the second stage, which contained two KTA crystals (3 and 4) and was overlapped with the 1064 nm beam to promote difference frequency generation mixing process. By rotating the KTP and KTA crystals from the first and second stage, respectively, a tunable mid-infrared beam from  $2000\text{ cm}^{-1}$  to  $4000\text{ cm}^{-1}$  can be generated. A detailed alignment procedure is given elsewhere.<sup>34</sup>

#### **2.4. 1064 nm, infrared and guide beam paths to SFGIM**

The 1064 nm fundamental beam and the tunable infrared beam generated by the OPG/OPA were employed for the SFG imaging microscope. The layout of the 1064 nm and IR beams optical

path are illustrated in Figure 2-3. The fundamental 1064 nm beam from the Ekspla Nd:YAG laser was split into two beams using a 90:10 split ratio beam splitter (BS1). The beam containing 10% energy was sent to the SFG microscope by mirrors M1 through M11. The beam arrived at the surface with a 60° incidence angle from the surface normal. The polarization of the IR beam was purified by a germanium Brewster's angle polarizer (P), and directed to the sample stage using mirrors M2 through M4. A calcium fluoride lens was used to focus the IR beam onto the surface.

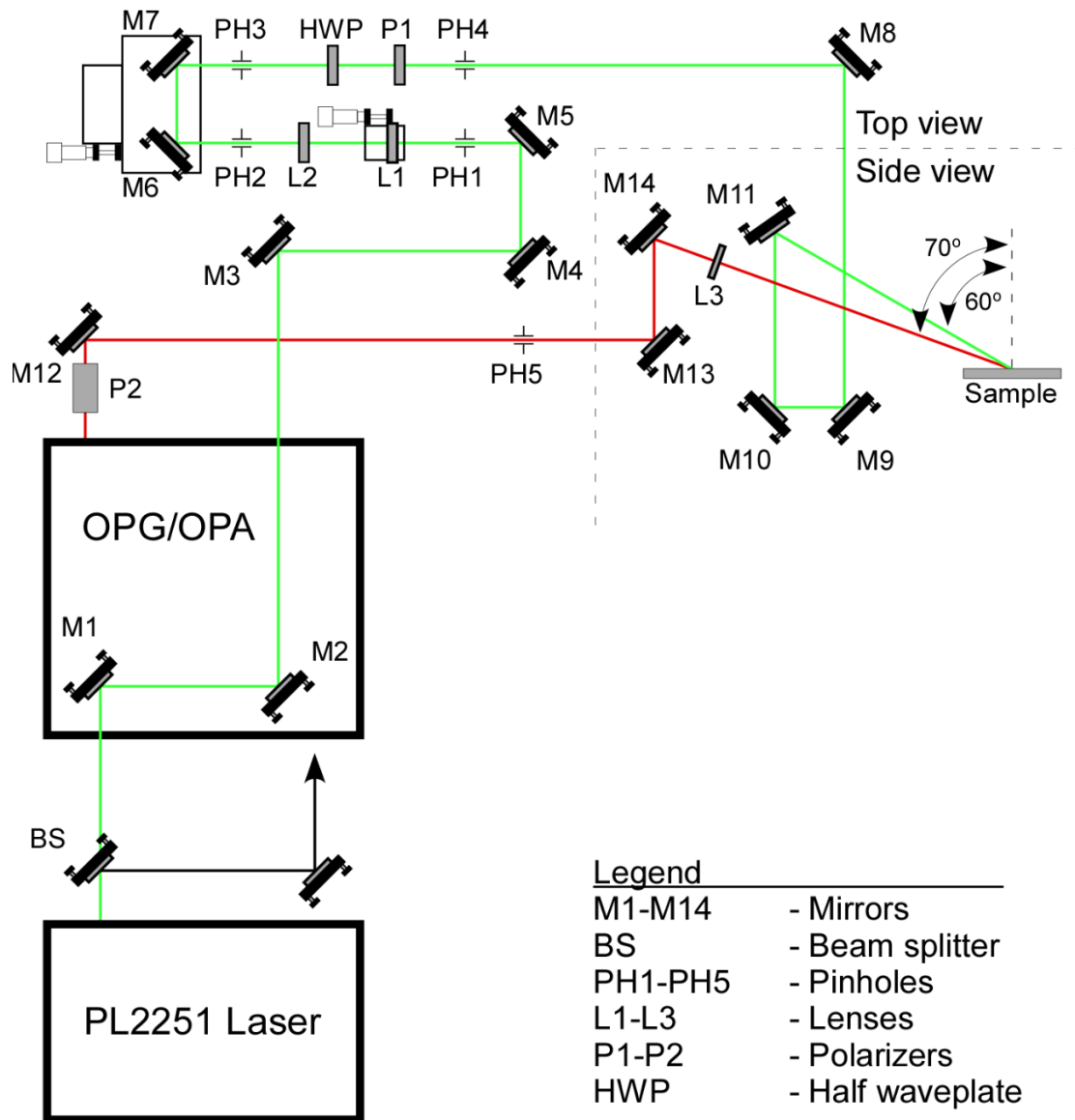


**Figure 2-3.** Illustration of the 1064 nm and IR beam paths for the SFG imaging microscope.

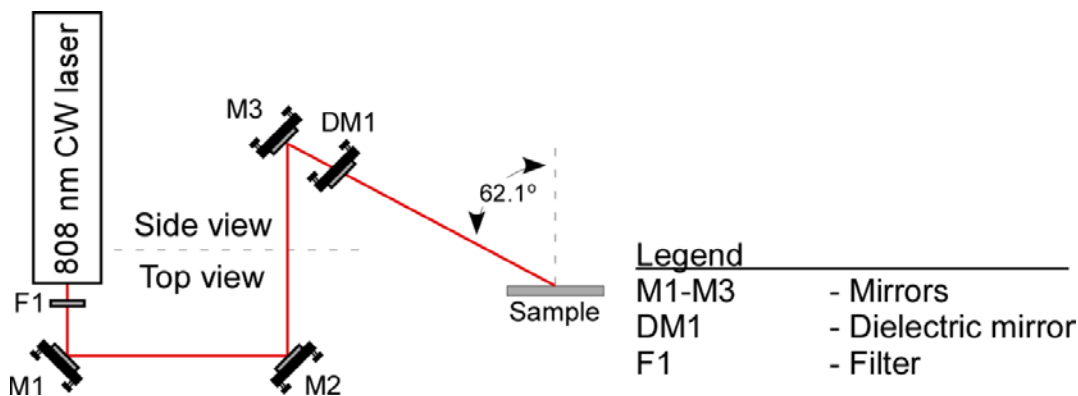


**Figure 2-4.** Illustration of the guide beam path for the SFG imaging microscope.

The beam arrived at the surface with a  $70^\circ$  incidence angle from the surface normal, at the same position and time as the 1064 nm beam.

The alignment of the sample and the detection side of the SFG microscope was achieved by employing a 808 nm continuous wave laser as a guide beam. As shown in Figure 2-4, the guide beam's energy was first attenuated using a filter to protect the relay lens and the detector from damage. The beam was reflected by mirrors M1 through M3, went through dielectric mirror DM1 and arrived at the sample surface with an incident angle of  $62.1^\circ$ . After the guide beam passed the filter, an IR viewer was used to aid in aligning the guide beam. A detailed description of the optical components and alignment procedure is given elsewhere.<sup>25, 68-69</sup>

## 2.5. Sum frequency generation imaging microscope

A pulsed picosecond, 20Hz, 1064 nm Nd:YAG laser (EKSPLA) was used to pump an optical parametric oscillator/amplifier (OPG/OPA) to generate a tunable mid-IR beam. The incident angles of the 1064 nm and mid-IR beams was set to  $60^\circ$  and  $70^\circ$  from the surface normal, respectively, and generated the SFG beam at around 800 nm. The polarization of the input beams and the SFG beam were p-polarized. Sample alignment was aided by the 808 nm guide beam.

Once the guide beam was reflected off the sample, it followed the SFG beam's path shown in Figure 2-5.

The generated SFG output beam followed a path that was at an angle of approximately  $62.1^\circ$  from the surface normal, and passed through a relay lens (Edmund optics 45-760) to maintain the size and focus of the beam. A short pass filter (900 AESP Omega Optical) with the cut off wavelength of 890 nm was positioned on the front side of the relay lens to filter out the strong 1064 nm beam. After passing through the relay lens the SFG signal was reflected off a diffraction grating (Newport, 33B75FL02-701R), which was used to correct for the distortion of the image.<sup>70</sup> The SFG beam was then passed through a 10 $\times$  objective lens (Mitutoyo 378-824-1) to magnify the image, then gold mirrors were used to reflect the SFG beam in the direction parallel to the CCD

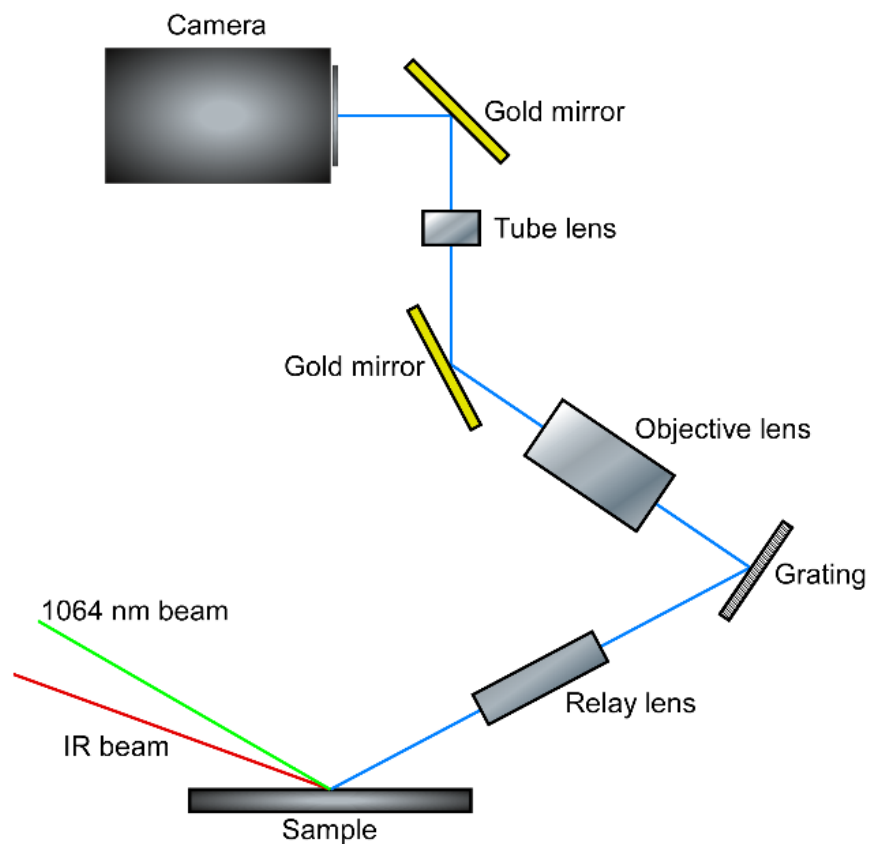


**Figure 2-5.** SFG imaging microscope illustration.

optical axis. A tube lens (Edmund, NT56-073) was used to collimate the image before going to the CCD camera. The SFG signal was collected using an intensified charge-coupled device (iCCD) camera (Roper Scientific, PI-MAX:1024i) with a 1024 x 1024 pixel chip. The captured SFG images had a spatial resolution of 2  $\mu\text{m}$ . The iCCD camera was used in a gating mode with the gate width of 10 ns to avoid integration over background light. In order to reduce the dark counts, the detector temperature was maintained at -20  $^{\circ}\text{C}$ .<sup>25</sup>

## 2.6. SFGIM signal collection

The detector used for the SFGIM was a Roper Scientific, PI-MAX4:1024i, intensified charged-coupled device (iCCD) shown in Figure 2-6. PI-MAX4 uses a proximity-focused micro-channel plate (MCP) image intensifier (Gen III HRf intensifier) fiber-optically coupled to a CCD array.<sup>71</sup> The image intensifier used in the iCCD camera was a Gen III HRf intensifier with the efficiency curve shown in Figure 2-7. Based on the efficiency curve in Figure 2-7, the quantum efficiency for the SFG wavelengths acquired for these studies was about 25%.<sup>72</sup>



**Figure 2-6.** Princeton Instrument PI-MAX4 iCCD detector.

The data acquired by the iCCD camera was sent to the computer for processing and display. WinSpec/32 software (version 2.6.23, password: 5FJ5MG) was used for data acquisition and system configuration. The iCCD camera was controlled by the WinSpec/32 program via a supplied GigE Ethernet card (INTEL® PRO/1000 GT desktop adapter) that was installed into the computer's PCI Slot. The Ethernet card required the EbDriverTool32.exe driver, which was downloaded and installed from Princeton Instruments website.<sup>71</sup> The intensifier gain on the detector was manually adjusted between the values of 1 and 100. Intensifier gain setting of 1 corresponds to no gain and a setting of 100 corresponds to maximum gain. The camera was utilized in mode which was triggered by the Nd:YAG laser. A gate width of 100 nsec and 10 gates per

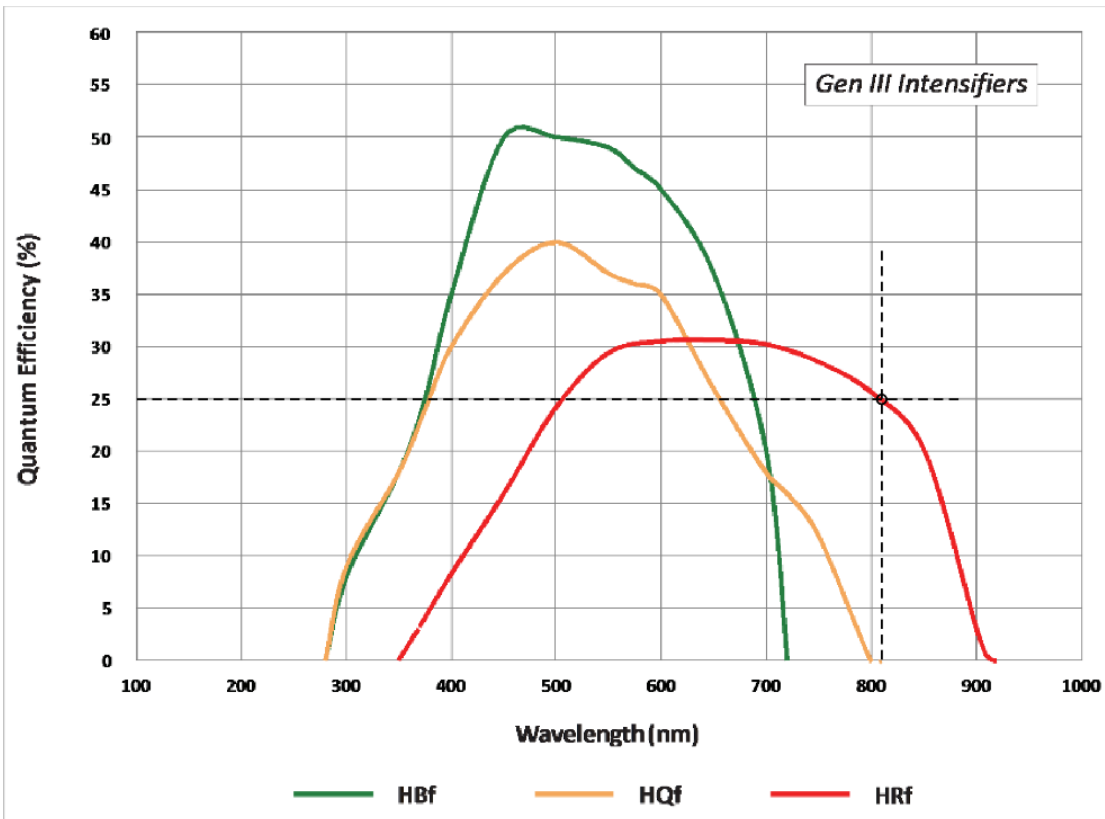


**Figure 2-7.** Quantum Efficiency curve of the PI-MAX4 Gen III HRf intensifier. The circle indicates the quantum efficiency at 810 nm.<sup>72</sup>

exposure integration was used for sample alignment purposes by the guide beam. For SFG signal acquisition in spectral mode, the gate width was set to 10 nsec with 10 gates per integration, in imaging mode, the gates per integration was set between 1000 to 5000, dependent on the signal to noise requirements.

Using a National Instruments LabView program on the LaserVision computer, which controlled the LaserVision OPG/OPA via the LaserVision motor controls program, the IR frequency range and tuning speed were specified (see Figure 2-8). The LabView program controlled the scanning rate of the IR frequencies of the OPG/OPA while simultaneously the Winspec/32 program collected the SFG signal as images in a sequence. For every 5  $\text{cm}^{-1}$  interval

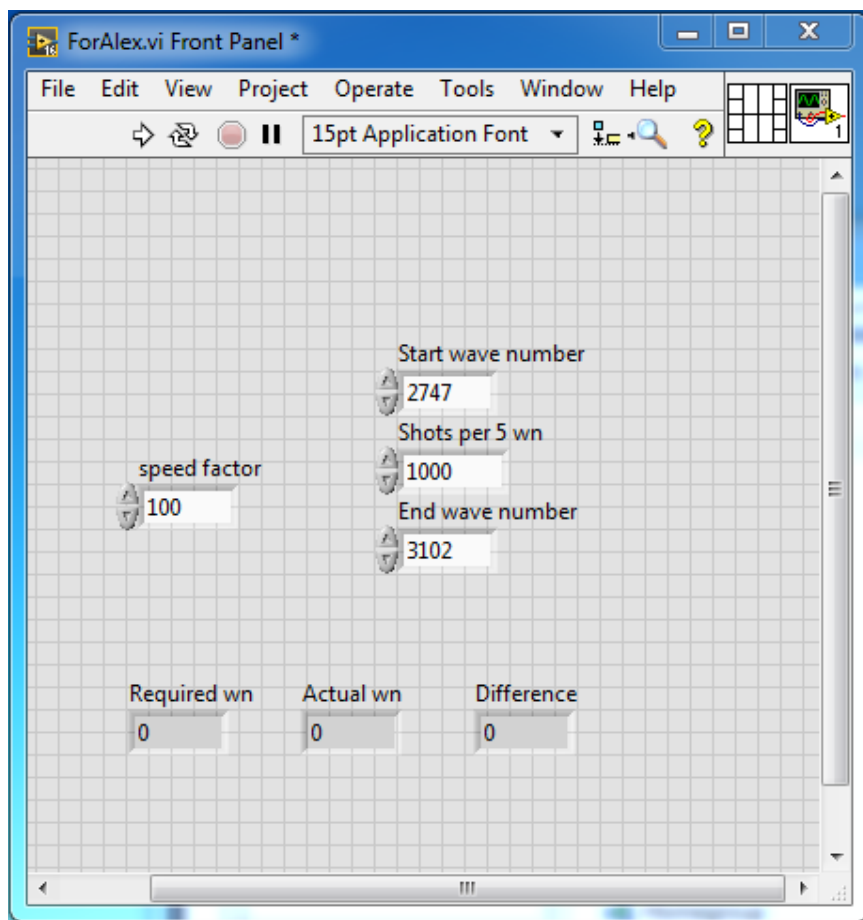


**Figure 2-8.** LabView program for wavenumber range and tuning rate control of OPG/OPA

of the specified wavenumber range an SFG image was saved which contained the total SFG signal of that interval.

## 2.7. Factor analysis

Factor analysis is performed by taking a data set of interest  $D$ , consisting of  $r$  rows and  $c$  columns,<sup>37, 73</sup>

$$D = [d_{ik}]_{r \times c} \quad (2.7)$$

where  $d_{ik}$  represents a data point associated with the  $i^{\text{th}}$  row and  $k^{\text{th}}$  column designee of the matrix, and obtaining a mathematical “abstract” solution by decomposition. Each point,  $d_{ik}$ , of the data matrix modeled by equation (1), after decomposition, is expressed as a linear sum of product terms

$$d_{ik} = \sum_{j=1}^s r_{ij} c_{jk} \quad (2.8)$$

where the number of terms in the sum,  $s$ , is called the number of factors, or components,  $r_{ij}$  and  $c_{jk}$  are row factors and column factors, respectively. The data matrix can be decomposed using singular value decomposition (SVD) into two matrices:<sup>74</sup>

$$D_{r \times c} = U_{r \times s} S_{s \times s} V'_{c \times s} = R_{abstract} C_{abstract} \quad (2.9)$$

$$US = R_{abstract}, V' = C_{abstract} \quad (2.10)$$

where  $U$  and  $V$  are unitary matrices and the columns of  $U$  are left-singular vectors and rows of  $V'$  (transpose of  $V$ ) are right-singular vectors of  $D$ .  $S$  is a diagonalized matrix where the diagonal entries are the singular values of  $D$ .<sup>37</sup> Applying SVD results in two abstract matrices,  $R$  (row) and  $C$  (column) matrices. Since this factor analytical solution is purely mathematical having no physical or chemical meaning, resulting matrices are termed “abstract” matrices.

The row and column factors obtained by SVD are to be referred to as abstract factors in this thesis. The outlined mathematical process is referred to as principal factor analysis (PFA)

within the FA technique. Principal factor analysis, principal component analysis (PCA), and SVD produce essentially the same result and have been used interchangeably in literature.<sup>37</sup>

To acquire physically or chemically recognizable factors (referred to as real factors), a transformation of the abstract factors is required. Target testing is a unique transformation method which tests potential factors, known as target factor analysis (TFA).<sup>37</sup> Target testing serves as a mathematical bridge between abstract and real factors. The target transformation matrix,  $T$ , is obtained from a least-squares operation involving the PFA solution and the individual targets being tested. Target factor transformation is accomplished by carrying out the following mathematical operation:<sup>37</sup>

$$D = R C = R T T^{-1} C = X Y \quad (2.11)$$

$$X = R T \text{ and } Y = T^{-1} C \quad (2.12)$$

where  $T$  and  $T^{-1}$  are the target transformation and inverse target transformation matrices and  $X$  and  $Y$  are the transformed matrices that contain the real factors with physically meaningful information such as the concentration of each component, and spectrum of component. The transformation involves finding linear combinations (weighted sums) of the abstract factors, which produce meaningful physically significant spectra. Mathematically, transformation is generally described as:<sup>42</sup>

$$c'_1 = w_1 c_1 + w_2 c_2 + \cdots + w_n c_n \quad (2.13)$$

where  $c'_1$  is the real factor obtained by target transformation,  $c_1$  through  $c_n$  are the original abstract factors obtained by PFA, and  $w_1$  through  $w_n$  are the weighting terms which are determined by the target transformation matrix  $T$ . The target transformation of abstract factor to real factors is graphically shown in Figure 2-9.

In order to determine the correct number of significant factors to employ, Malinowski's empirical factor indicator function was used. The factor indication function (IND) is able to pick out the correct number of factors and is defined as:<sup>37</sup>

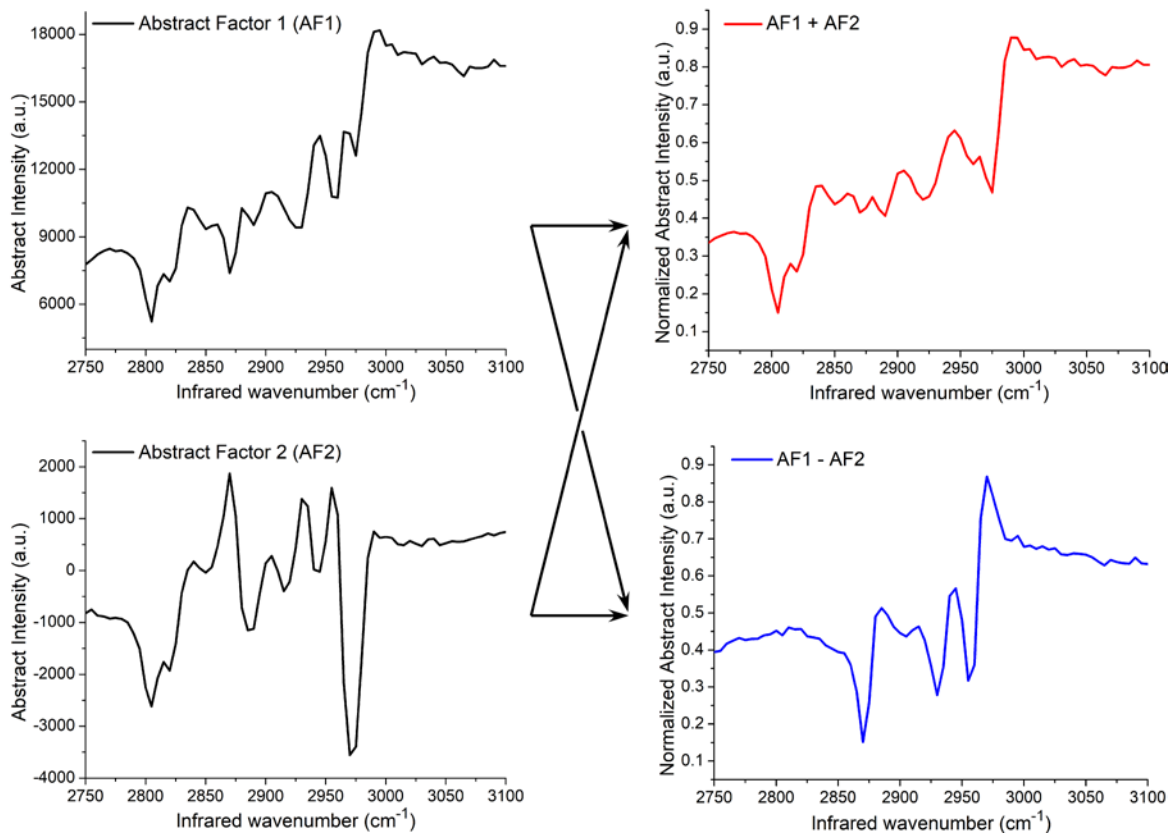


**Figure 2-9.** Outline of target transformation of abstract factors into real factors by TFA. The real factors are obtained by adding the factors obtained by PFA using various weightings of the factors.<sup>42</sup>

$$IND = \frac{RE}{(s-n)^2} = \sqrt{\frac{\left[ \frac{\sum_{j=n+1}^s \lambda_j^{01}}{l(s-n)} \right]}{(s-n)^2}} \quad (2.14)$$

where  $RE$  is the real error,  $\lambda$  is the eigenvalue,  $n$  is the number of eigenvalues and eigenvectors associated with the true factors,  $s$  is the number of eigenvalues and eigenvectors obtained after factor analyzing the raw data, where it is equal to the number of row or column entries, whichever

is smaller, and  $l$  equals or column entries, whichever is larger. By examining the IND function behavior as  $n$  varies, it is possible to determine the true number of factors. The IND function decreases as more and more primary eigenvectors are employed in data reproduction. However, once the primary set is exhausted and secondary eigenvectors are included in the reproduction, the IND function increases. The IND function reaches a minimum value when the correct number of factors are employed.

To confirm that target is a real factor in the chemical system, a SPOIL function was used to evaluate all the targets used.<sup>37</sup> The SPOIL function is defined as:

$$SPOIL = \frac{RET}{EDM} \approx \frac{RET}{REP} \quad (2.15)$$

where  $RET$  is the real error in the target spectra,  $EDM$  is the error contributed by the data matrix, and  $REP$  is the root mean square of the target transformed factor. Experimental data error makes the pure test spectra different from the target transformed spectra. Since the error in the target transformed spectra comes from error in the data matrix,  $EDM$  is similar to  $REP$ . For the data here, a SPOIL value below 20 indicates that the tested target spectra is acceptable, while a value between 20 and 30 is moderately acceptable. A SPOIL value above 30 indicates an unacceptable target spectra, meaning it is not a real factor in the chemical system.

## 2.8. Data processing

During the SFG imaging, the iCCD camera acquires a sequence of SFG images which include a background correction. Once a set of images was acquired, the images were stacked in ImageJ software according to decreasing IR wavenumber using the stack reverser plugin. The vibrational spectra from a specified region of interest (ROI) of the image stack was extracted using the spectra microscopy plugin.<sup>68</sup> By utilizing a macros plugin, which runs a code written for spectral extraction of specified ROIs, the image stack was divided into specified ROIs and the

corresponding spectra was extracted and saved as .txt files with a reference to image position. The macros program code is shown in Figure 2-10. The code specifies the number of pixels per ROI size, spectral wavenumber range, the target folder where the extracted file are saved to, and file name with image position identification.

The extracted spectra from ROIs were then used to construct a data matrix, where each spectrum is a column of the data matrix, on which the PFA and TFA were performed using

```

Image Spectra Extraction - Notepad
File Edit Format View Help
// close() only works for Image Windows
// selectWindow() works for Image Windows and some Tool Windows

//  selectWindow("B&C");
//  selectWindow("Plot Values");
//  selectWindow(title + "-" + x + "-" + y);

var x = 0;
var y = 0;

var title = getTitle();
var savename = title;

// Use any value of 2^n: 2, 4, 8, 16, 32, 64, 128, 256, 512, 1024 for the step-size
var step=5; ← Number of pixels per ROI in x and y direction

for (j=0; j<1019; j+=step)
{
  wait(800);
  for (i=0; i<1019; i+=step)
  {
    makeRectangle(x, y, step, step);
    run("Spectral Microscopy", "starting=3100 step=5");
    ← Spectral wavenumber range with wavenumber interval size per image

    savename = "C:\\Users\\User_name\\Desktop\\folder_name\\file_name" + "-" + x + "-" + y;
    ← Target save to folder and file name

    selectWindow(title + "-" + x + "-" + y);
    close();
    selectWindow("Plot Values");
    saveAs("text", savename);
    run("Close");

    selectWindow(title);
    x+=step;
  }

  x=0;
  y+=step;
}

```

**Figure 2-10.** Image Spectra Extraction code used for spectral extraction from ROIs

MATLAB software. The .txt spectra files were imported into MATLAB and arranged into a matrix in a known sequence for image reconstruction. The data matrix was first checked for cosmic ray spikes, which were removed by MATLAB 'hampel' function for removing outliers.

The data matrices were first analyzed by significant factor analysis (SFA) code to determine the number of significant factors using factor (empirical) indicator function (IND).<sup>37</sup> The IND function reaches a minimum when the correct number of factors were employed and are considered significant factors. The significant abstract factors can be obtained by specifying the desired number of factors as a second input of the SFA function. To obtain all the abstract factors, the data matrices can be decomposed using the singular value decomposition (SVD) function in MATLAB. The SVD decomposition results in two abstract matrices, R (row) and C (column) matrices (see Equation. 2.10). The first column of R and C matrix represent the spectra and spatial distribution, respectively, of the first abstract factor. The second column of R and C matrix represent the spectra and spatial distribution, respectively, of the second abstract factor, and so on. The significant abstract factors from the C matrices were used to reconstruct maps of each abstract factors' contribution weight in each ROI by shaping the columns into the right image size.

In order to obtain real factors, the data matrix was analyzed by target factor analysis (TFA) code. The TFA requires a target matrix containing the desired test spectra, as columns, as an input along with a specified number of abstract factors desired for the target transformation. When it is possible, test (target) spectra of pure components were used to produce the transformation matrix to convert abstract factors into physically significant real factors. The TFA results indicated how well the target transformed real factors represent the test spectra. The resulting real factors were used to construct the respective chemical maps by using the loading factor analysis (LFA) code. Each real factor was presented as a column of the resulting LFA matrix. By separating the

reshaping the columns, the respective chemical maps were obtained. The MATLAB codes for SFA, TFA and LFA were modified codes provided by Malinowski.<sup>37</sup> All MATLAB codes used are presented in Appendix A.

## 2.9. Microcontact printing

Microcontact printing ( $\mu$ CP) is a special form of soft lithography method that uses a polydimethylsiloxane (PDMS) stamp to form patterned self-assembled monolayers (SAMs) on metal surfaces in a controlled fashion.<sup>25, 35, 75-79</sup> The advantage of using  $\mu$ CP is that it is simple and inexpensive to produce the PDMS stamp, which absorbs SAMs onto its surface and releases them during stamping. The resulting patterned SAMs formed are a mirror image of the pattern on PDMS stamp. The process by which a patterned surface is fabricated is illustrated in Figure 2-11. The PDMS stamp used for  $\mu$ CP was produced by combining the PMDS prepolymer with its curing agent in a 10:1 mass ratio. After stirring for about 5 minutes, the mixture was placed under house vacuum for about an hour to remove bubbles produced during mixing. Then it was poured onto a clean, ridged master template containing the target pattern(s), which was previously treated with

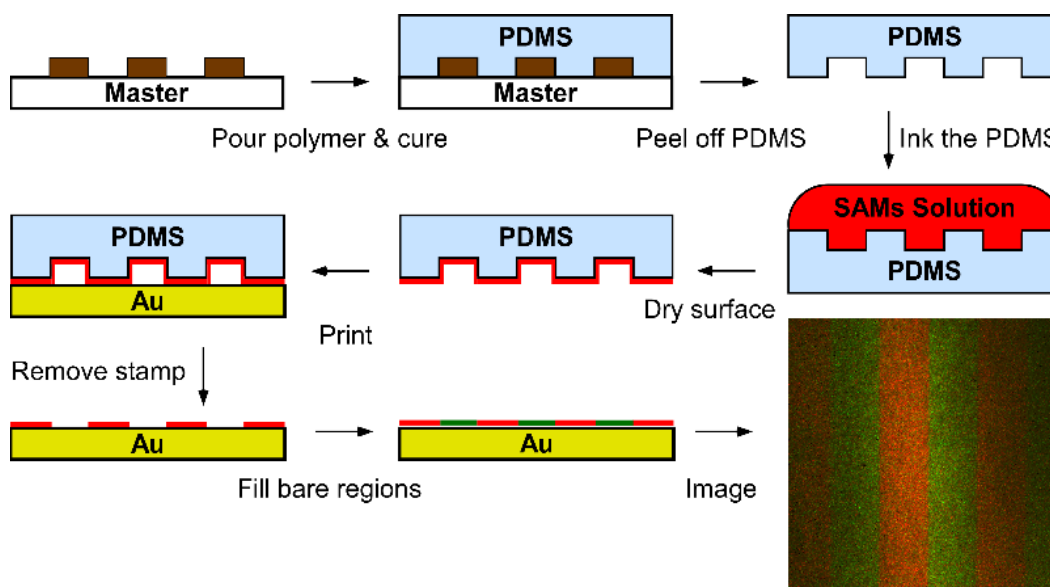


**Figure 2-11.** Illustration of the microcontact printing process.

octadecyltrichlorosilane as an anti-adhesion layer for easy peeling of PDMS from the master pattern. The master pattern with the PDMS mixture was then placed into an oven to cure for 2 hours at 80 °C. After curing, the PDMS was carefully peeled off from the master pattern and cleaned by sonicating in ethanol for about 10 minutes. The stamped was then dried inside the oven.

5 mM alkanethiol solutions with different terminal functional groups in ethanol were prepared. To prepare the two component monolayer sample, a drop of the thiol solution was placed on top of the PDMS stamp and then nitrogen gas was used to dry the surface of the stamp. The stamp was then carefully placed on the surface of evaporated gold on silicon wafer for 15 minutes. After the stamp was removed, the sample was placed minutes into an alkanethiol solution with a different functional group to backfill bare gold regions. After 15 minutes, the sample was taken out, rinsed with ethanol and dried with nitrogen gas.

For the preparation of the five component monolayer samples, a pattern from the PDMS stamp was selected and cut into four pieces by cutting the pattern in half and then cutting again perpendicularly. Each individual piece of the PDMS stamp was inked with a different alkanethiol solution by placing a drop of the respective alkanethiol solution on top of the PDMS stamp and then dried by nitrogen gas. The four PDMS pieces were brought together and carefully placed on the surface of evaporated gold on silicon wafer. Light pressure was applied to the PDMS stamp and left on the surface for 15 minutes. After the stamp was removed, the sample was placed into the alkanethiol solution not used for stamping, to backfill bare gold regions. After 15 minute solution deposition, the sample was taken out and rinsed with ethanol and dried with nitrogen. The sample was placed into the SFG imaging microscope, aligned to the target pattern and SFG images were taken. The preparation procedure of the five component sample is schematically shown in Figure 2-12.

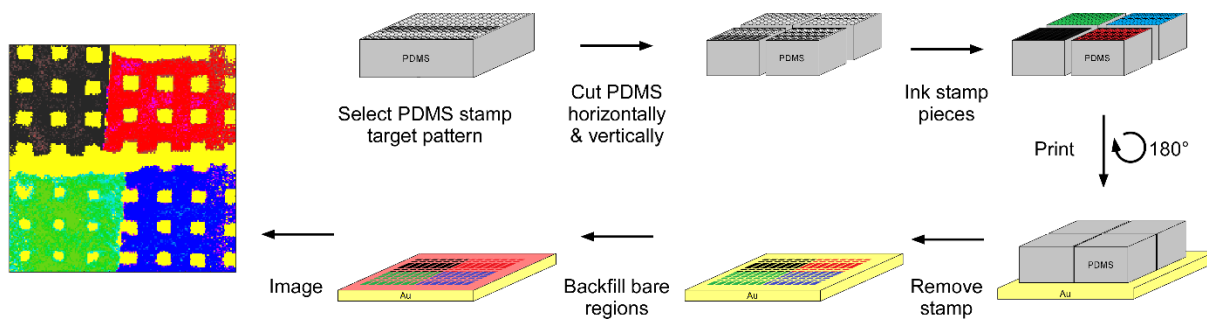


**Figure 2-12.** Schematic diagram of the preparation procedure of the five component patterned sample.

# **Chapter 3: Sum Frequency Generation Imaging Microscopy of Self-Assembled Monolayers on Metal Surfaces: Factor Analysis of Mixed Monolayers**

## **3.1. Introduction**

Surfaces and interfaces are considered as a boundary between a material and its surrounding environment and influence interactions with that environment. At the molecular level, the surface atoms, the top 1-10 atomic layers, have a different chemical and physical environment than atom in the bulk and play an important role in many of the chemical, physical, and biological processes.<sup>1-2</sup> In order to gain a fundamental understanding of the underlying processes it is critically important to know the chemical and physical properties of the surfaces or interfaces. To investigate surface properties, model systems like self-assembled monolayers (SAMs) have been used.<sup>29-30</sup> A self-assembled monolayer is an organized layer of organic molecules adsorbed on a substrate surface. These SAMs are easy to prepare, are molecularly ordered and are robust under many conditions of use. In order to control the surface chemically and spatially, patterned systems of mixed SAMs have been utilized. These patterned SAMs systems have been produced by many different techniques like microcontact printing<sup>80-82</sup>, photolithography<sup>83</sup>, lift-off-lithography<sup>84</sup> and ink-jet printing<sup>85</sup>. Microcontact printing ( $\mu$ CP) is a form of soft lithography method that uses a polydimethylsiloxane (PDMS) stamp to form patterns of SAMs on the metal surface in a patterned and controlled fashion.<sup>80-82</sup> The advantage of using PDMS is that it absorbs SAMs onto its surface and releases them during stamping. It is also nontoxic, commercially available, compatible with wide variety of organic and organometallic molecules and unreactive towards most chemicals.<sup>80</sup>

Self-assembled monolayer patterned surfaces have been characterized by techniques such as X-ray photoelectron spectroscopy (XPS), Secondary Ion Mass Spectrometry (SIMS), low energy electron diffraction (LEED), and Scanning probe microscopy techniques (STM, AFM), but each technique has advantages and disadvantages.<sup>5-7, 86-87</sup> These techniques show the structures of the monolayers but require other techniques, such as vibrational spectroscopy, to determine the molecular composition of the surface.<sup>10</sup> Sum frequency generation (SFG) spectroscopy is a second-order, nonlinear optical technique that provides vibrational spectra of the molecules at the interface.<sup>20</sup> Chemical identification, molecular orientation, monolayers' conformational order, and vibrational dynamics can be studied by SFG spectroscopy.<sup>21-22</sup> The technique is very useful in providing information about the interfacial structure of a surface. However, it typically only provides the average information of the sampled area and does not show local characteristics due to the spatial averaging. The sum frequency generation imaging microscopy (SFG-IM) technique, based on SFG, provides chemical images of the surface.<sup>23-26</sup> The chemical contrast is based on the vibrational frequencies of the adsorbed molecules on the surface. The advantage of using SFG-IM to study patterned surfaces is that it not only provides identity of surface/interface molecular species, information about surface/interface chemical structure, but it also provides a spatial distribution overview of chemicals on the surface, which make it a useful technique in chemical imaging.<sup>24, 27</sup>

In this study, SFG-IM was used to acquire SFG images of patterned alkanethiol monolayer on gold by  $\mu$ CP. The images were then analyzed by factor analysis (FA). It is a statistical method that uses mathematical procedures to investigate whether a number of observed variables are linearly related to some smaller number of unobservable factors.<sup>73</sup> The method has been applied in Raman and infrared spectroscopy to determine the number and identities of components in a

series of related multicomponent mixtures.<sup>38-40, 88-89</sup> The focus of these experiments was to investigate the application of FA on SFG images and to assess the chemical maps and abstract factors produced by FA.

## **3.2. Theoretical Background**

### **3.2.1. Sum frequency generation.**

The theory of SFG has been described previously in detail.<sup>10, 21</sup> The sum frequency generation process in this study is achieved when two coherent laser pulses, a fixed wavelength of 1064 nm ( $\omega_{1064\text{nm}}$ ) and a tunable wavelength infrared pulse ( $\omega_{\text{IR}}$ ), are spatially and temporally overlapped on a surface. The induced nonlinear polarization at the surface generates the coherent sum frequency output beam at the sum of the two input beam frequencies ( $\omega_{\text{SF}} = \omega_{1064\text{nm}} + \omega_{\text{IR}}$ ). When the IR frequency is at a resonance frequency of one of the vibrational modes, an enhanced SFG signal is observed.

### **3.2.2. Factor analysis.**

The theory and application of factor analysis (FA) are discussed fully by Malinowski.<sup>90</sup> A short description of the main steps are given in the Supporting Information. Factor analysis is a mathematical technique for studying matrices of data. It is a highly useful method for furnishing the number of components, concentrations, and spectral information via a purely mathematical route.<sup>90</sup> It is performed by taking a data set of interest  $D$ , and after decomposition, expressing it as a linear sum of product terms. The resulting terms are purely mathematical ‘abstract’ column and row factors that contain no physical or chemical meaning. To acquire physically or chemically recognizable factors, a transformation of the abstract factors is required. Target testing is a unique transformation method which tests potential factors, known as target factor analysis (TFA).<sup>90</sup> Target testing serves as a mathematical bridge between abstract and real factors. Factor analysis

includes principle component analysis (also known as principal factor analysis (PFA)) and TFA<sup>90</sup> and their use for this study is outlined in the Experimental section.

### **3.3. Experimental**

#### **3.3.1. Sample patterning by microcontact printing**

The system of study consisted of patterned SAMs on gold substrate manufactured by microcontact printing ( $\mu$ CP). The PDMS stamp used for  $\mu$ CP was produced by combining the PDMS prepolymer and curing agent in a 10:1 volume ratio. After stirring for about 5 minutes, the mixture was placed under house vacuum for about an hour to remove bubbles produced during mixing. It was then poured onto a clean surface of the rigid master pattern, previously treated with octadecyltrichlorosilane as an anti-adhesion layer for easy peeling of PDMS from the master pattern. Then, the master pattern with the PDMS mixture was placed inside the oven to cure for two hours at 80 °C. After curing, the PDMS was carefully peeled off from the master pattern and cleaned by sonicating in ethanol.

Pure solutions of 5 mM octadecanethiol (ODT), methoxy-hexadecanethiol (MeOHT), and 15,15-difluoro-octadecane-1-thiol (FODT) in ethanol were prepared. To prepare the two component monolayer samples, a drop of the ODT solution was placed on top of the PDMS stamp and then nitrogen gas was used to dry the surface of the stamp. The stamp was then carefully placed on the surface of evaporated gold on silicon wafer for 15 minutes. After the stamp was removed, the sample was placed into the backfill solution (MeOHT or FODT) for 15 minutes. Target samples for TFA application were prepared from the same solutions as the two component samples. The stamped ODT target sample was prepared by the same procedure described above but without backfilling. MeOHT and FODT target samples were prepared by solution deposition, with no stamping, for 15 minutes of the respective MeOHT or FODT solution on evaporated gold

silicon wafer. All samples were rinsed with ethanol solvent and dried with nitrogen gas before taking images.

### **3.3.2. Sum frequency generation imaging microscope.**

A picosecond pulsed, 20 Hz, Nd:YAG laser was used to generate the 1064 nm, which pumped the optical parametric generator/amplifier (OPG/OPA) to generate the tunable mid-IR beam. The incident angles of the 1064 nm and mid-IR beams were set to 60° and 70° from the surface normal, respectively, and generated the SFG beam at around 800 nm with an angle of approximately 62.1° from the surface normal. An intensified charge-coupled device (iCCD) camera with a 1024 x 1024 pixel chip was used to acquire the SFG images. A more detailed description of the SFG-IM is given in Chapter 2.5.

### **3.3.3. SFG image data processing with PFA and TFA application.**

During the SFG imaging the iCCD camera acquires a sequence of SFG images while the infrared frequency is continuously scanned at a set scan rate. Each image is an average of five IR wavenumbers, with user specified number of laser shots per image. No processing of the presented SFG images were performed except for background correction. Once a set of images was acquired, the images were stacked according to decreasing IR wavenumber using ImageJ software. The image stack was cut into region of interests (ROIs) of 5-by-5 and 2-by-2 pixels, which corresponds to 6.5-by-6.5  $\mu\text{m}$  and 2.5-by-2.5  $\mu\text{m}$  respectively, and vibrational spectra were extracted from each ROI (see Appendix B Figure B-1).<sup>91</sup> The extracted spectra from ROIs were then used to construct a matrix, where each spectrum is a column of the data matrix, on which the PFA and TFA were performed using MATLAB software. The MATLAB codes for PFA and TFA are provided by Malinowski.<sup>90</sup>

The data matrices were first analyzed by PFA to determine the number of significant factors using factor (empirical) indicator function (IND).<sup>90</sup> The IND function reaches a minimum when the correct number of factors were employed and are considered significant. A more detailed explanation is given in the Supporting Information. To obtain abstract factors, the data matrices were decomposed using the singular value decomposition (SVD) function in MATLAB. The significant abstract factors from the *C* (column) matrices were used to construct maps of each abstract factors' contribution weight in each ROI; *R* (row) matrices abstract factors were used to produce the corresponding abstract factors' spectra. No further processing was performed on the abstract factors' spectra and maps presented. When it is possible, test (target) spectra of pure components were used to produce the transformation matrix to convert abstract factors into physically significant real factors. The resulting real factors were used to construct the respective chemical maps. The chemical maps were constrained to positive values only with no other constraints or processing.

### **3.4. Results and Discussion**

#### **3.4.1. SFG imaging of ODT-MeOHT sample.**

The SFG images and spectra given in Figure 3-1 represent the ODT—MeOHT on evaporated gold substrate sample. Figures 3-1a – 3-1c show SFG images taken at 2810  $\text{cm}^{-1}$ , 2875  $\text{cm}^{-1}$ , and 2950  $\text{cm}^{-1}$ , respectively. The spectra shown in Figures 3-1d and 3-1e were extracted from the ROI highlighted in Figures 3-1a and 3-1b, respectively. The observed SFG image contrast is due to the vibrational contrast in the SFG spectra, where the dark areas in the images correlate to the resonance peaks in the SAMs. ODT and MeOHT have distinct vibrational spectra in the 2800-3000  $\text{cm}^{-1}$  region that can be used to distinguish the two molecules. Figures 1d and 1e are the characteristic SFG MeOHT and ODT spectra, respectively, on gold. The MeOHT shows 6 peaks

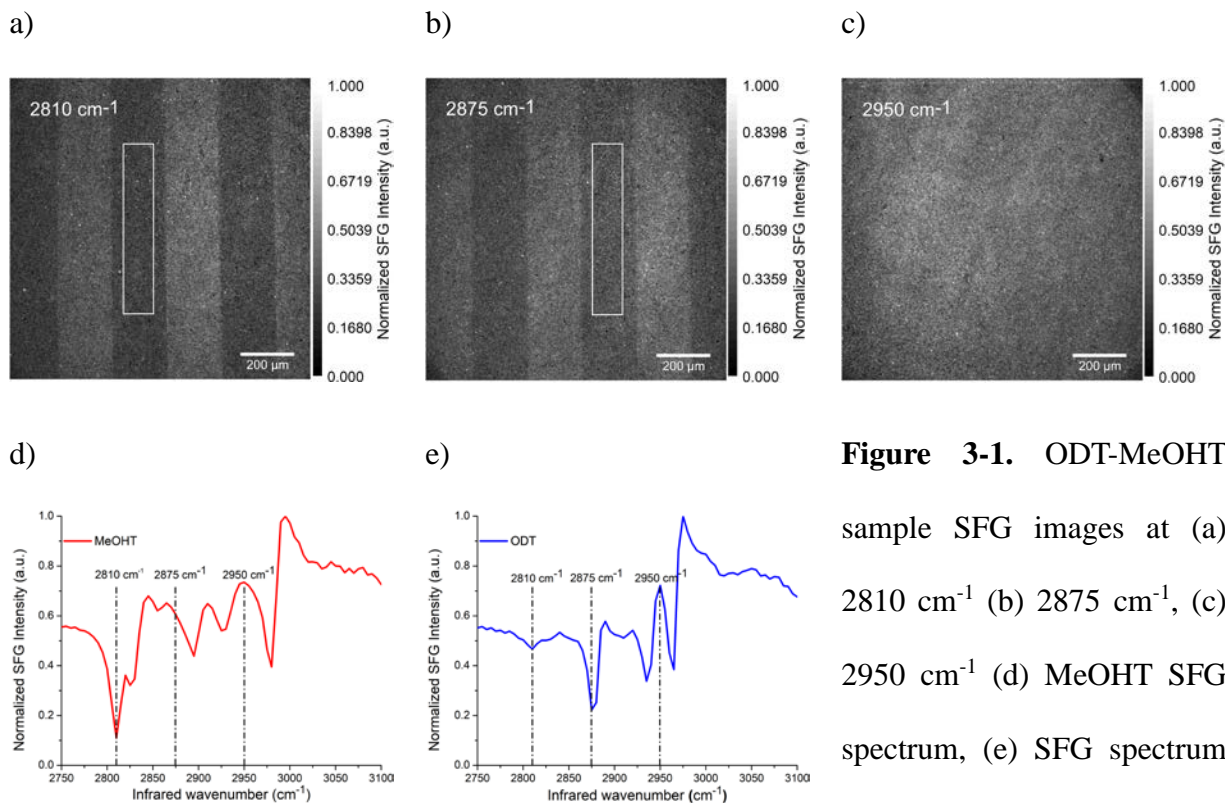


**Figure 3-1.** ODT-MeOHT sample SFG images at (a) 2810  $\text{cm}^{-1}$  (b) 2875  $\text{cm}^{-1}$ , (c) 2950  $\text{cm}^{-1}$  (d) MeOHT SFG spectrum, (e) SFG spectrum of ODT stamped region.

in the C-H stretching region, a doublet at 2810/2830, 2855, 2900, 2930, and 2980  $\text{cm}^{-1}$  which correspond to the symmetric stretch of the  $\text{CH}_3$  in the terminal methoxy group,  $\text{CH}_2$  symmetric stretch,  $\text{CH}_2$  asymmetric stretch, Fermi resonance and the  $\text{CH}_3$  antisymmetric stretch, respectively.

The peaks in Figure 3-1e at 2875 and 2935  $\text{cm}^{-1}$  are the methyl symmetric C-H stretch and its Fermi resonance, respectively, and at 2965 and 2975  $\text{cm}^{-1}$  are the methyl antisymmetric in-plane and out of plane stretching, respectively. The observed methoxy peak at 2810  $\text{cm}^{-1}$  in the ODT spectrum is due to the MeOHT mixing in the ODT stamped region during the backfill step which is most likely due to stamp defects and also that the overall monolayer formed by microcontact printing is less densely packed than those from solution-deposited films.<sup>25</sup> The observed dark areas of the SFG image at 2810  $\text{cm}^{-1}$  correspond to the MeOHT covered surface, which has a symmetric methoxy stretch at that frequency, and lighter areas correspond to the ODT surface, which has no

vibrational modes at that frequency and signal is due to Au non-resonant response. The image contrast inverts at  $2875\text{ cm}^{-1}$  due to MeOHT being off resonance while the methyl-terminated ODT is at resonance. When both the MeOHT and ODT are off vibrational resonant frequencies, little image contrast is observed. An example of an off vibrational resonant image is shown in Figure 3-1c.

### 3.4.2. Two component maps.

Chemical maps have been constructed from SFG images using spectral fitting which requires sufficient signal-to-noise ratio of the individual spectra. This limits the spectral curve-fitting to larger ROIs or long signal acquisition times.<sup>79, 91-92</sup> In order to reduce signal acquisition time without resorting to larger ROIs or sacrificing image resolution, factor analysis was utilized. SFG images of ODT—MeOHT sample were acquired at 5000 shots per image (5k) and also at 500 shots per image (0.5k). The SFG images were processed as outlined in the SFG imaging data processing with PFA and TFA application. The SFG and resulting PFA images are shown in Figure 3-2. Figures 3-2a and 3-2b are the raw SFG images acquired at  $2875\text{ cm}^{-1}$  with 5k and 0.5k, respectively. The contrast between the ODT and MeOHT regions in Figure 3-2b is not as high as in Figure 3-2a and is difficult to determine where the regions boundary edge is due to low edge resolution. However, the images obtained after PFA processing of the 5k and 0.5k, Figures 3-2c and 3-2d respectively, show an improved region contrast and edge resolution. As observed in Figures 3-2b and 3-2d, PFA significantly improves the image contrast between the ODT and MeOHT regions for the 0.5k data compared to the 5k data.

The extracted SFG spectra of ODT and MeOHT of the 0.5k sample using  $6.5\text{-by-}6.5\text{ }\mu\text{m}$  ROI size for PFA do not contain sufficient signal to show obvious vibrational modes that could be used to differentiate ODT from MeOHT (see Appendix B Figure B-2) required for spectral fitting.

To understand and be able to determine the significance of PFA and TFA results, the 5k SFG data was analyzed to determine what each significant real and abstract factor represented. Then, 0.5k real and abstract factors were compared to the 5k factors to determine if the real and abstract factors represented the same information in the 0.5k as the 5k data set. To test the limit of PFA, 100 shots per image SFG data was analyzed with PFA but due to the low SFG signal, PFA was unable to

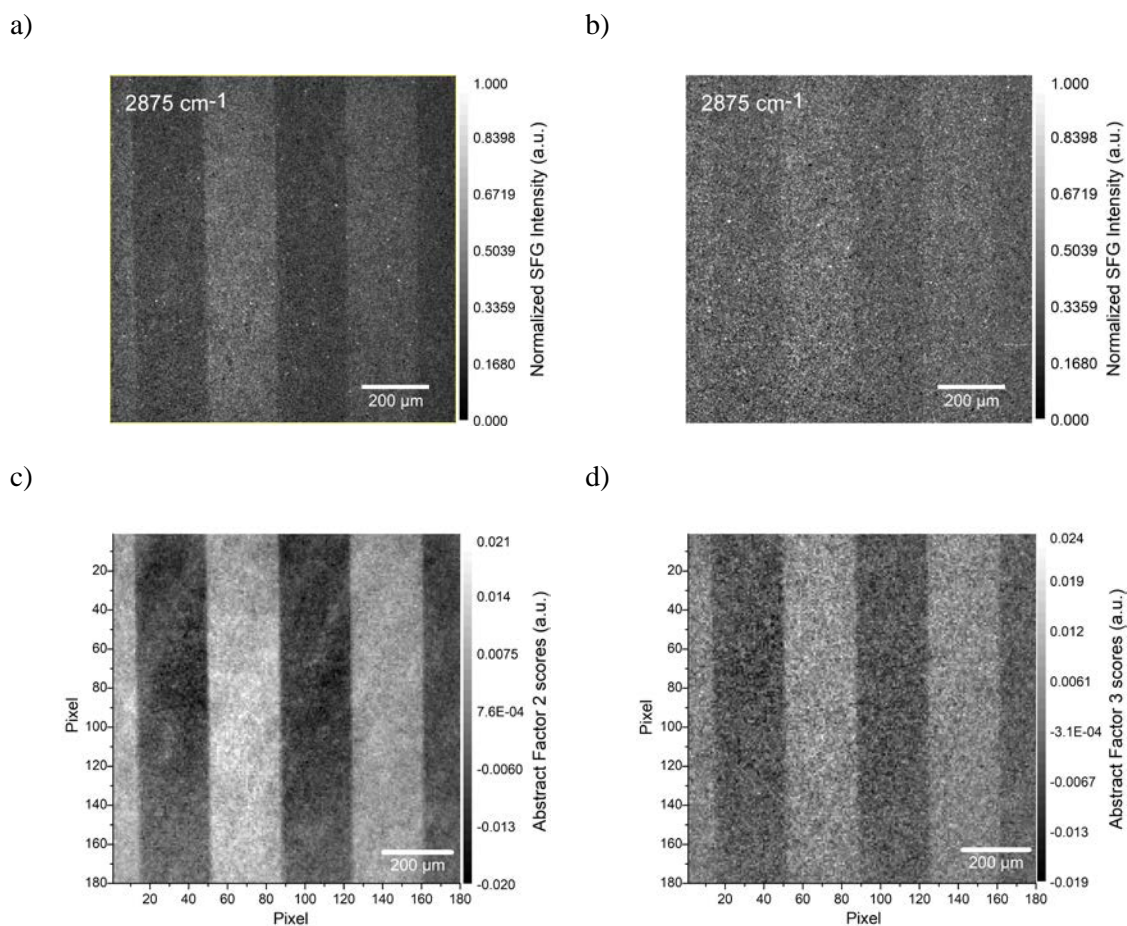


**Figure 3-2.** ODT—MeOHT sample SFG images acquired with (a) 5k shots per image at 2875 cm<sup>-1</sup> and (b) 0.5k shots per image at 2875 cm<sup>-1</sup>. PFA resulting maps of 6.5-by-6.5 μm ROI (c) 5k shots per image 2<sup>nd</sup> abstract factor and (d) 0.5k shots per image 3<sup>rd</sup> abstract factor.

determine the number of significant factors nor produce satisfactory results (see Appendix B Figures B-3 and B-4).

### **3.4.3. Analysis of 5000 laser shots per image ODT—MeOHT sample.**

Principal factor analysis produced 71 abstract factors, due to each spectrum used for the data matrix consisting of 71 data points, but IND function indicated only two significant abstract factors that account for 91.7% of data variance. The 69 non-significant abstract factors account for 8.3% of data variance and are assumed to contain only noise. The percent contribution of each abstract factor was calculated from eigenvalues. After target transformation by TFA of the abstract factors using ODT and MeOHT target spectra, the resulting component weights of ODT and MeOHT were obtained in each ROI. The component weight results were then mapped back onto the surface to provide a spatial distribution of the MeOHT and ODT shown in Figures 3-3a-3-3d. Figures 3-3a and 3-3b are the MeOHT chemical maps constructed from 2.5-by-2.5  $\mu\text{m}$  and 6.5-by-6.5  $\mu\text{m}$  ROIs, respectively, where the MeOHT regions are represented by lighter shaded region. Figures 3-3c and 3-3d are the ODT chemical maps constructed from 2.5-by-2.5  $\mu\text{m}$  and 6.5-by-6.5  $\mu\text{m}$  ROIs, respectively, where the ODT regions are represented by lighter regions. The chemical maps of MeOHT and ODT obtained by TFA are in good agreement with the observed SFG image in Figure 3-1b. The TFA results of ODT and MeOHT images shown in Figure 3-3 are the physically significant real factors obtained by target transformation of the abstract factors. The mathematical process by which the significant abstract factors are target transformed to produce the real factors is graphically shown in Appendix B Figure B-5. The MeOHT and ODT were obtained by taking weighted fractions of the two significant factors and subtracting the second abstract factor from the first one to obtain MeOHT image or adding them together to obtain ODT image.

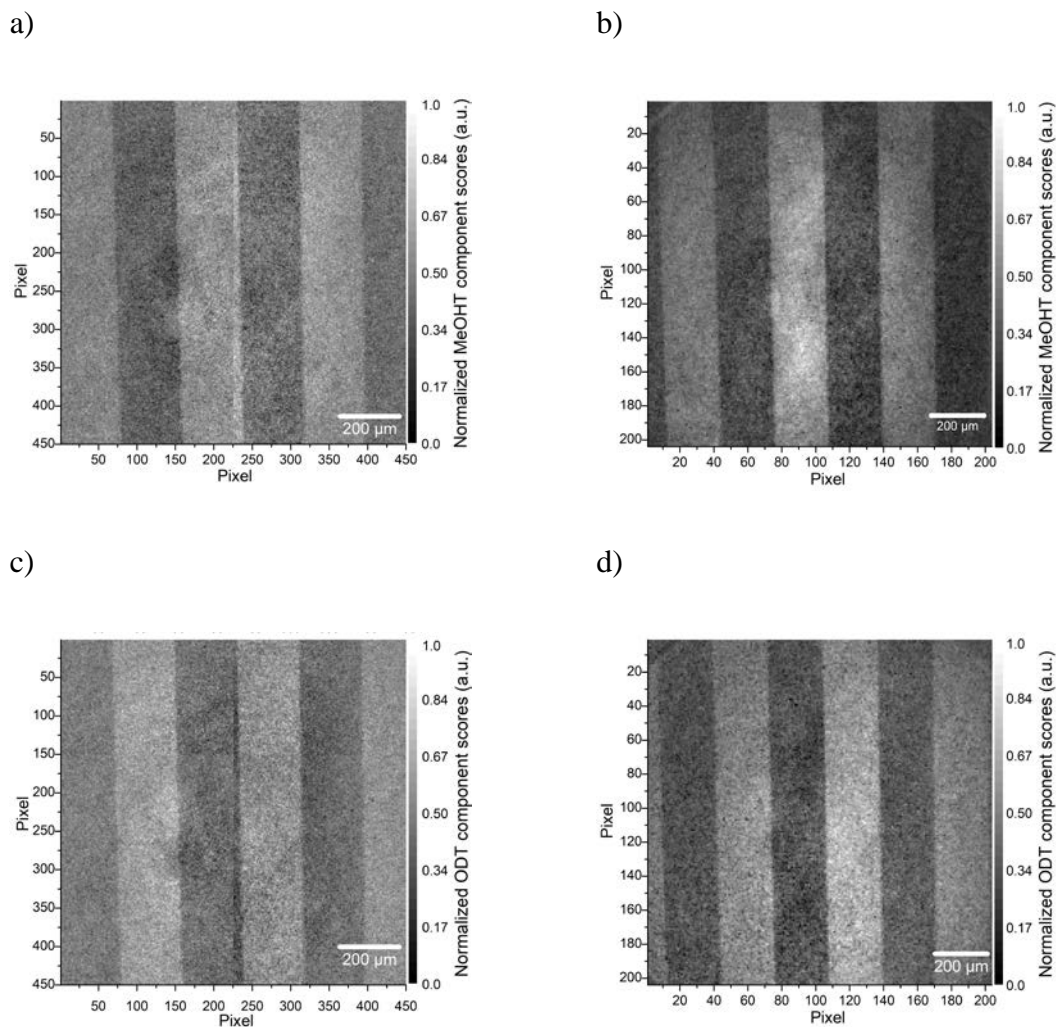


**Figure 3-3.** MeOHT and ODT chemical maps. (a) MeOHT using 2.5-by-2.5  $\mu\text{m}$  ROIs (b) MeOHT from 6.5-by-6.5  $\mu\text{m}$  ROIs (c) ODT using the 2.5-by-2.5  $\mu\text{m}$  ROIs (d) ODT from 6.5-by-6.5  $\mu\text{m}$  ROIs. Note: data matrix containing the 2.5-by-2.5  $\mu\text{m}$  ROIs was too large for the computer calculations as a whole. It was divided into six equal fractions and TFA calculations were performed on each individually. The TFA results were then combined to produce the final images shown in a and c.

The two significant abstract factors obtained by PFA as are shown in Figure 3-4. First abstract factor accounts for 91% of the data matrix variance and since the spectra was not mean centered, it represents the average spectrum of the sample analyzed.<sup>93</sup> Figures 3-4a and 3-4c show the first abstract factor extracted from the *R* and the corresponding *C* matrix, respectively. In Figure 3-4a, the observed mathematical results are the combined average of the ODT and MeOHT SFG signal response on gold substrate, where all the ODT and MeOHT vibrational peaks observed in Figures 3-1d and 3-1e are present. Figure 3-4c represents overall beam profile over the imaged

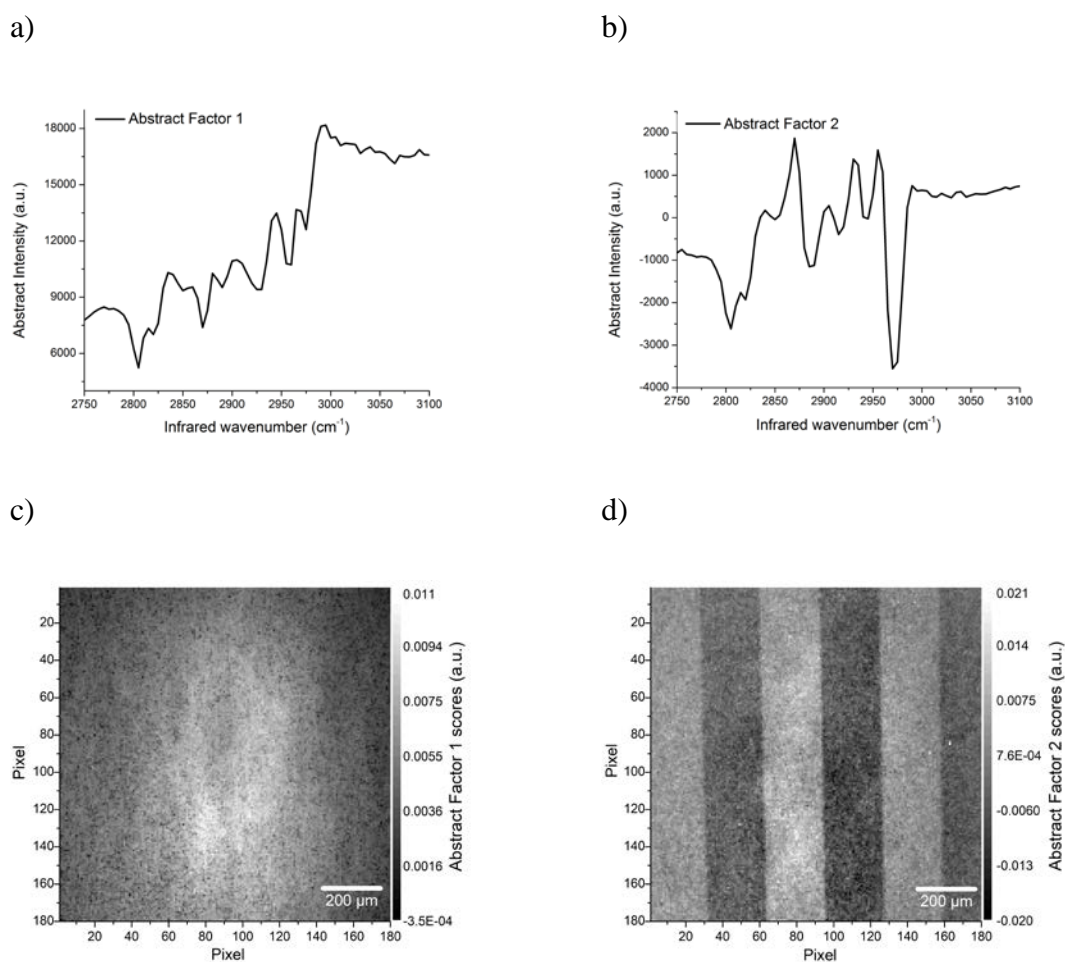


**Figure 3-4.** First and second abstract factors from row matrix (a, b) and column matrix (c, d) obtained by PFA of ODT—MeOHT sample data matrix.

area with no image contrast between the ODT and MeOHT regions. The second abstract factor accounts for 0.74% of data variance. The  $R$  matrix component of the second factor is shown in Figures 3-4b and represents the spectral difference between the observed ODT and MeOHT peak positions.<sup>93</sup> It also contains both the ODT and MeOHT spectral features but in derivative-like shape where the ODT peaks are pointing up and MeOHT peaks are pointing down. In Figure 3-5, the abstract factor is overlaid with the SFG difference spectrum of ODT and MeOHT, showing that the second abstract factor represents the difference spectra of ODT and MeOHT. The SFG difference spectrum of ODT and MeOHT was acquired by subtracting normalized ODT spectrum from normalized MeOHT spectrum (see Appendix B Figure B-6).<sup>34</sup> It has been observed that one vibrational band disappearing relative to another in the spectrum will produce a factor containing one negative and one positive weighted peak.<sup>93</sup> The corresponding second factor from the  $C$

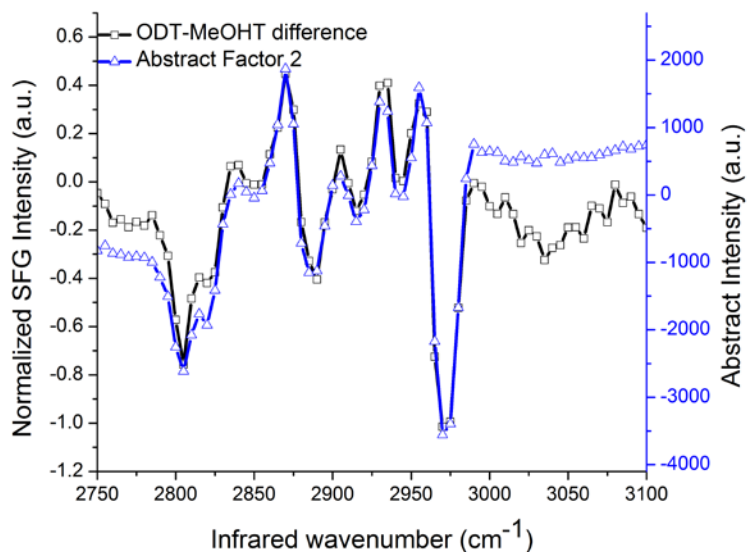


**Figure 3-5.** Resulting SFG spectrum of ODT and MeOHT after normalized ODT SFG spectrum was subtracted from the normalized MeOHT SFG spectrum and compared with the second abstract factor obtained from PFA.

matrix, Figure 3-4d, contains the image contrast between the ODT and MeOHT regions. Darker strips are the ODT regions and lighter stripes are the MeOHT regions. The contrast is maximized between the two regions by expressing one as positive values and the other one as negative values.<sup>93</sup> The PFA results shown in Figure 3-4 are considered abstract mathematical results that contain no physically meaningful information but based on Figures 3-4 and 3-5, they do contain real physical information.<sup>93</sup> In order to determine the significance of the information contained in the abstract factors, one must have some insight into the system analyzed. By analyzing the abstract factors one can narrow down the potential targets to test.

#### **3.4.4. Analysis of ODT—MeOHT sample obtained with 500 laser shots per image.**

SFG images acquired of ODT—MeOHT sample with 500 laser shots per image are shown in Figure 3-6. The contrast between the ODT and MeOHT regions in Figures 3-6a and 3-6b are not as high as in Figures 3-1a and 3-1b which were taken with 5000 shots per image. The 0.5k ODT—MeOHT stack was treated in the same manner as the 5k ODT—MeOHT stack. The IND function indicated three significant abstract factors, not two as was expected and observed for the 5k data. The first three abstract factors obtained by PFA are shown in Figure 3-7 and account for 81.2% of data variance. The first abstract factor shown in Figures 3-7a and 3-7d contains 79.2% of data variance and is almost identical to the first factor of 5k (Figures 3-4a and 3-4c). It also represents the combined average spectrum of the ODT and MeOHT spectra and the beam profile of the imaged area, containing both the ODT and MeOHT peaks but showing no image contrast between the two regions. The second abstract factor, shown in Figures 3-7b and 3-7e, represents 1.3% of data variance and is different than the second abstract factor of 5k sample (Figures 3-4b and 3-4d). The second abstract factor is assumed to represent some change to the combined average spectrum that has not been fully determined yet or might be a result of increased noise in data. The

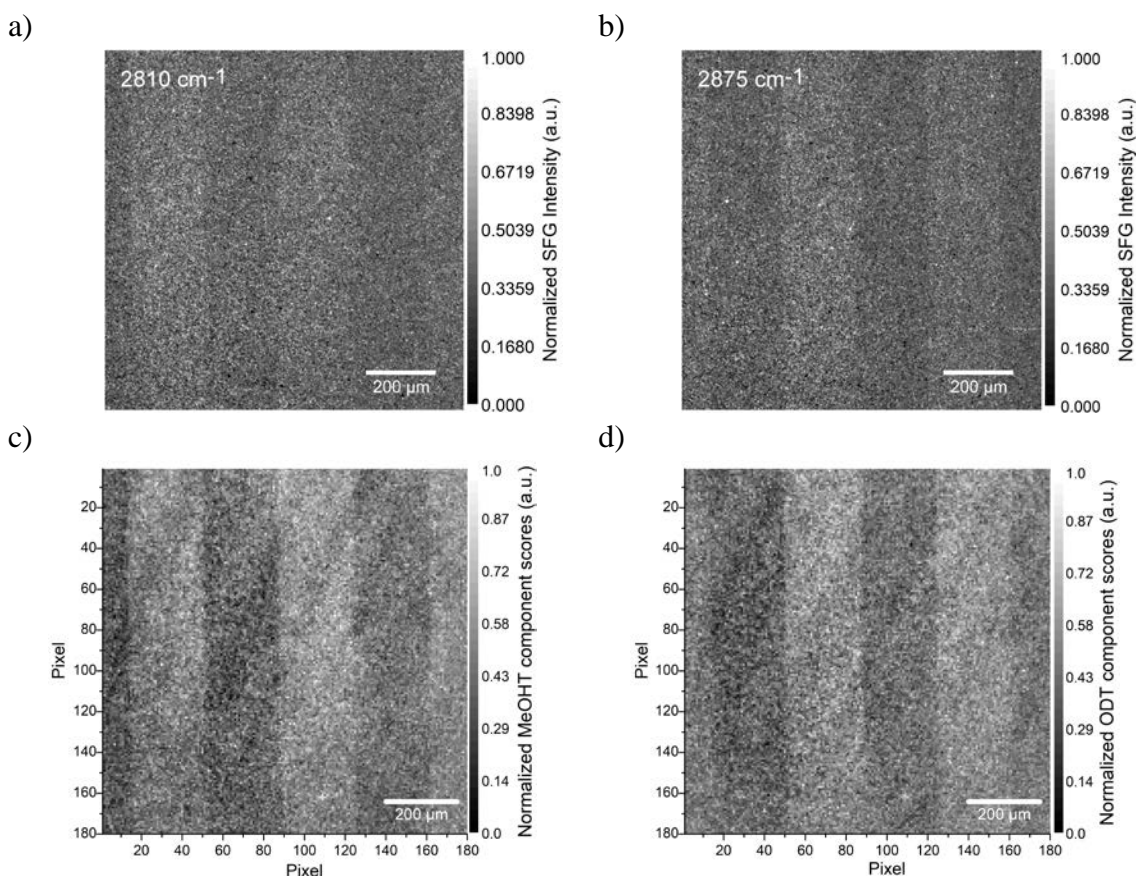


**Figure 3-6.** 500 shot ODT—MeOHT sample SFG images at (a)  $2810\text{ cm}^{-1}$  (b)  $2875\text{ cm}^{-1}$  and TFA resulting maps of  $6.5\text{-by-}6.5\text{ }\mu\text{m}$  ROI (c) MeOHT and (d) ODT.

third abstract factor accounts for 0.72% of the input data matrix. The  $R$  matrix component, Figure 3-7c, is very similar to the second abstract factor of the 5k (Figure 3-4b) which represents a difference like spectrum of ODT and MeOHT, where SFG spectrum of ODT was subtracted from MeOHT spectrum. The contrast between ODT and MeOHT regions observed in Figure 3-7f is maximized by expressing one as positive values and the other one as negative values, which is similar to what was previously observed for the second abstract factor of 5k (Figure 3-4d). The abstract image obtained from the 0.5k data set (Figure 3-7f) is not as detailed and lacks the resolution, especially between the boundary of ODT and MeOHT regions, when compared to the image obtained from the 5k data set (Figure 3-4d). These results demonstrate that PFA can provide

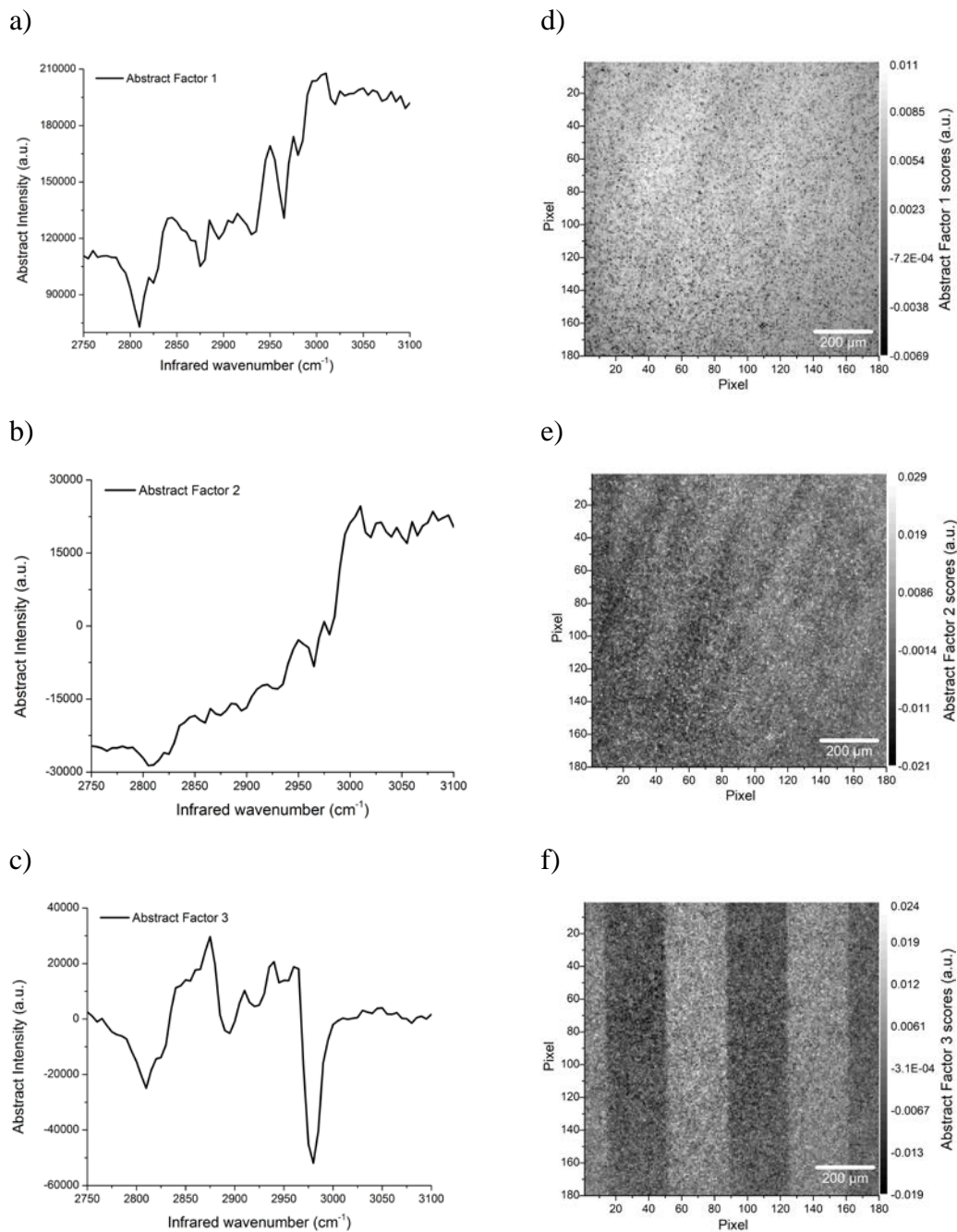


**Figure 3-7.** First three abstract factors from row matrix (a-c) and column matrix (d-f) obtained by PFA of 500 shot ODT—MeOHT sample data matrix.

very similar qualitative chemical mapping results from data obtained with  $1/10^{\text{th}}$  the shots per spectral point as originally obtained. This also demonstrates that FA can be used as an alternative chemical mapping to spectral fitting. The FA and TFA results of smaller ROIs and shorter acquisition time data indicate that it FA can reduce the amount of time required to acquire full spectral images with sufficient contrast between the different chemical regions when compared to spectral fitting.

### 3.4.5 Analysis of ODT—Fluoro-ODT sample.

The ODT and FODT molecules exhibit almost identical spectra except that the  $-\text{CH}_3$  symmetric and asymmetric stretches differ (relative shifted blue for FODT) by  $5\text{ cm}^{-1}$  (Figure 3-8b). The structural difference between the ODT and FODT molecules is that FODT contains two fluorines at the 15<sup>th</sup> carbon position (Figure 3-8a). SFG imaging was taken of ODT—FODT

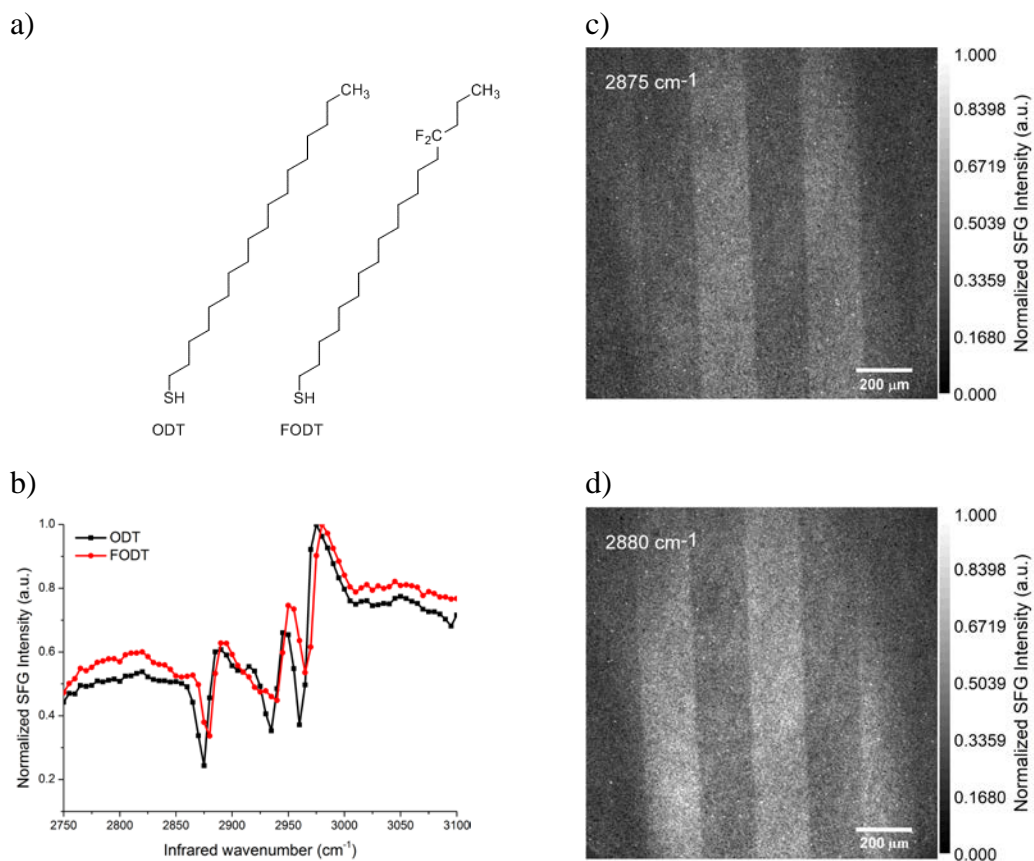


**Figure 3-8.** (a) ODT and FODT molecular structure. ODT—FODT sample SFG (b) spectra and (c) image at  $2875\text{ cm}^{-1}$  and (d)  $2880\text{ cm}^{-1}$  with 5000 shots.

sample with 5000 laser shots per image. The SFG images taken at 2875 and 2880  $\text{cm}^{-1}$ , Figure 3-8c and 3-8d, respectively, show good contrast between the ODT stamped region and fluorinated thiol backfilled region represented by darker shaded regions in the respective images. The stack of ODT—FODT SFG images were treated the same as the ODT—MeOHT SFG images.

Principal factor analysis results indicated that there are three significant abstract factors that account for 96.5% of data variance. The 3.5% account for the 68 non-significant abstract factors that are assumed to contain only noise. Target testing of ODT and FODT by TFA revealed that both ODT and FODT are real factors of the data analyzed. The three significant abstract factors produced by PFA are shown in Figure 3-9. The first abstract factor accounts for 95.7% of input data matrix. The *R* matrix component of the factor, Figure 3-9a, represents the average spectrum of the data matrix and is almost identical to the SFG spectra of ODT (Figure 3-10a) which might be due to ODT and FODT spectra being almost identical except for the methyl symmetric and asymmetric stretches are shifted by 5  $\text{cm}^{-1}$ . The SFG spectral resolution is 5  $\text{cm}^{-1}$ , where only a shift by one data point will result in the first abstract factor to resemble either ODT or FODT. The corresponding first abstract factor of *C* matrix, Figure 3-9d, represents the SFG beam intensity signal over the image area. The second abstract factor, Figures 3-9b and 3-9e, accounts for 0.51% of the input data matrix and represent some change to the first abstract factor that has not been determined yet, but has been observed in the 0.5k MeOHT—ODT results (Figures 3-7b and 3-7e). The third factor accounts for 0.28% of the input data matrix. The *R* matrix component, Figure 3-9c, represents the spectral difference between the observed ODT and FODT peak positions in derivative-like shapes.<sup>93</sup> It contains both the ODT and FODT spectral information where the ODT peaks are pointing down and FODT peaks are pointing up. When compared to the SFG ODT and

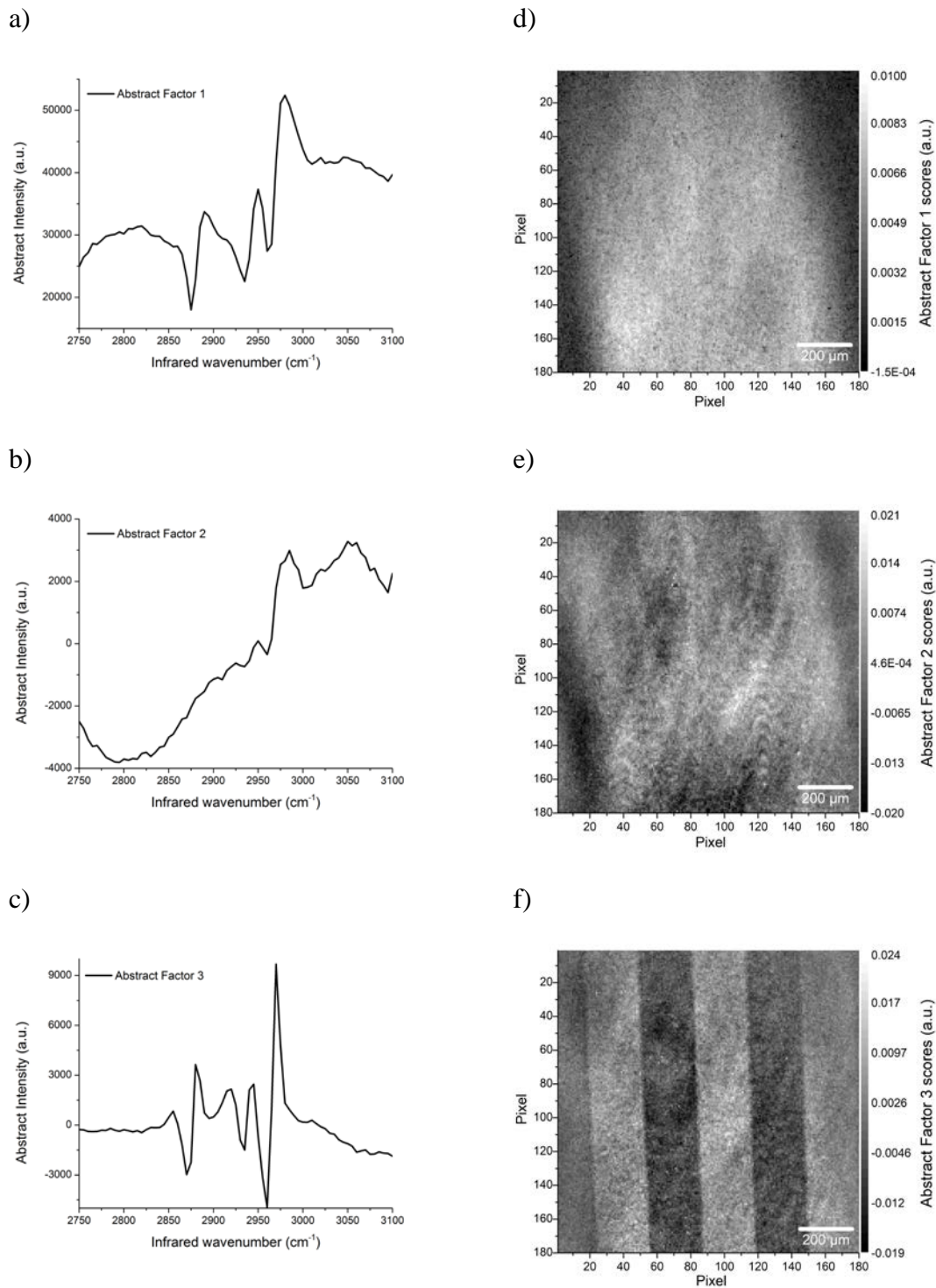


**Figure 3-9.** First three abstract factors from row matrix (a-c) and column matrix (d-f) obtained by PFA of ODT-FODT sample data matrix.

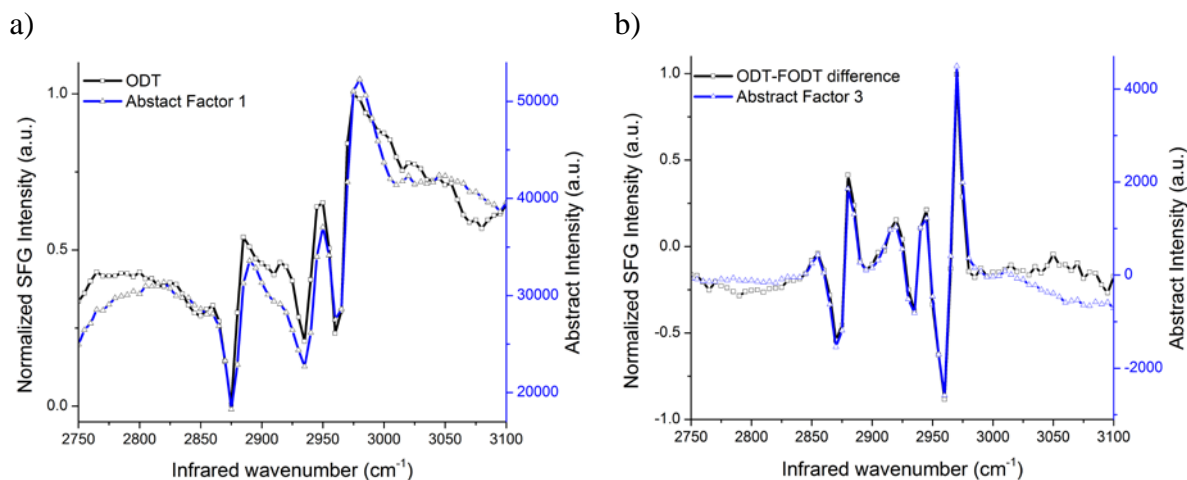


**Figure 3-10.** (a) First abstract factor compared with SFG spectrum of ODT, (b) resulting SFG spectrum of ODT and FODT after normalized FODT SFG spectrum was subtracted from the normalized ODT SFG spectrum compared with the third abstract factor obtained from PFA.

FODT spectra, it represents the difference spectrum of ODT and FODT (Figure 3-10b), where SFG spectrum of FODT was subtracted from ODT spectrum which is similar to what was previously observed for the second abstract factor of ODT—MeOHT sample. The corresponding *C* matrix component, Figure 3-9f, contains the image contrast between the ODT and FODT regions, where the darker and lighter regions of the image represent ODT and FODT regions respectively, which is in good agreement with SFG image of ODT and FODT shown in Figure 3-8c.

### 3.5. Conclusion

This work has shown that PFA and TFA can be used successfully on low signal data to extract individual species spectral information, and also the spatial distribution of chemically different alkanethiols on gold surface. In this study, the chemical systems studied have consisted of two components, where the chemical species used here have distinctly different vibrational

spectra, in the case of ODT and MeOHT, and very similar vibrational spectra, in the case of ODT and FODT. The resulting chemical maps have demonstrated that TFA can be successfully applied to SFG images to acquire real significant factors. It also shows that PFA can be applied just as successfully to data obtained with lower signal or with shorter acquisition times. The reconstructed chemical maps indicate that TFA can be utilized as an alternative to spectral fitting to generate chemical maps. This work has demonstrated that caution should be exercised when determining the number of chemical components present and which factors represent the corresponding components. The decomposition step produces abstract factors that do not necessarily represent the chemical components individually but may represent some other inherent underlying principles responsible for producing the data results analyzed. It has been observed that the number of significant factors do not always correspond to the number of components present. The components are not necessarily represented by the first or even the second abstract factor and may be represented by one factor or multiple factors or a combination of factors. It is considered that factors or components obtained by PFA are just mathematical results that contain no physical or chemical meaning but as this work has shown that they might contain meaningful information. It is important to remember that it is difficult to determine what factors contain the chemical species spectral information without targets. More studies need to be conducted to determine the effectiveness of FA on real samples that contain mixed unknown chemical species and random patterns.

## **ASSOCIATED CONTENT**

Supporting information available: Sum frequency generation imaging microscope, factor analysis, illustration of imaging stacking and spectral extraction, 100 shots per image SFG image and FA results, and an outline of target transformation of abstract factor into real factors.

## **ACKNOWLEDGMENTS**

We would like to thank Daniela Rodriguez for providing MeOHT. We gratefully acknowledge the NSF (CHE-1361885) for providing funds for this project. TRL wishes to thank the NSF (CHE-1710561), the Robert A. Welch Foundation (E-1320), and the Texas Center for Superconductivity at the University of Houston for providing generous support for this research.

# Chapter 4: Multicolor Chemical Imaging by Sum Frequency Generation Imaging Microscopy of Monolayers on Metal Surfaces

## 4.1. Introduction

The ability to directly visualize distinct molecular species on the surface is essential for gaining fundamental understanding of complex chemical systems. While there are many different optical imaging systems, majority are not surface sensitive, and many rely on tags or other secondary methods to generate image contrast. Sum frequency generation imaging microscopy (SFG-IM) is a unique surface specific technique for obtaining spatial distribution of molecules with label-free chemical contrast on the surfaces.<sup>23-25</sup> The capability of sub-monolayer sensitivity allows investigation of spatially inhomogeneous systems, to map chemical surface distribution, molecular arrangement, orientation, and domain formation.<sup>10, 20, 27, 94</sup> The technique is very useful in providing information about the interfacial structure of a surface, such as molecular coverage, molecular orientation and arrangement, chemical reactions, and chemical adsorption.<sup>24, 28, 95-99</sup> Sum frequency generation microscopy has been used to study a range of systems such as monolayers on metals, nonlinear materials, and biological systems.<sup>25, 27, 36, 91, 100-101</sup>

Vibrational spectroscopic imaging techniques including Fourier transform infrared, Raman, coherent anti-Stokes Raman, and stimulated Raman scattering are able to provide spatial structures and chemical information of the molecules present on the surface.<sup>11-19</sup> The limitation of these techniques as surface microscopy techniques is that they lack interface specificity and cannot distinguish surface from bulk signal. The advantage of SFG is its intrinsic sensitivity to molecules in a non-centrosymmetric environment, where inversion symmetry is broken.<sup>10, 21, 102</sup> This makes the SFG process highly surface-specific.

The surface molecular spatial distribution, molecular arrangement, orientation, and domain formation results obtained by SFG-IM have been acquired through spectral fitting.<sup>25, 27, 34, 36, 91, 103-105</sup> However, SFG has been mainly limited to binary chemical systems.<sup>28, 34, 103, 106-111</sup> At any single wavelength only two chemical species can be distinguish apart and spectral fitting is limited to spectral resolution of chemical species and signal-to-noise. A few SFG studies have utilized spectral decomposition to generate chemical maps.<sup>108, 110</sup>

Previous results of factor analysis (FA) application to SFG images demonstrated that it can be utilized as an alternative method to spectral fitting in generating chemical maps of binary systems.<sup>112</sup> The imaged chemical systems consisting of two different SAMs that had either distinctly different vibrational spectra or very similar vibrational spectra. In addition it was determined that FA can be successfully applied to data obtained with lower signals or with shorter acquisition times to reduce the time required for full spectral SFG imaging.

In this study, SFG images of a sample patterned by microcontact printing with multiple distinct alkanethiols on gold were acquired by SFG-IM, and then analyzed by FA. Utilizing a library consisting of SFG alkanethiol spectra, the chemical components were determined and their spatial distribution was mapped. Furthermore, FA, utilizing the alkanethiol library was used to determine the chemical identities and produce chemical maps of a random pattern multi-component alkanethiol sample. The results demonstrated the capability of FA combined with the alkanethiol library to determine the chemical composition and spatial distribution of alkanethiol monolayers on the surface of multi-component complex chemical system acquired by SFG-IM. In addition, FA revealed an unknown surface species, spectra of which was not present in the library.

## **4.2. Theoretical background**

### **4.2.1. Sum frequency generation**

The theoretical background of SFG and its application has been described previously in detail.<sup>10, 21, 113</sup> The SFG process is achieved when two coherent laser beams, a fixed wavelength of 1064 nm ( $\omega_{1064\text{ nm}}$ ) and a tunable wavelength infrared ( $\omega_{IR}$ ), are spatially and temporally overlapped on a surface to induce a second order nonlinear polarization. The induced polarization generates the coherent sum frequency beam at the sum of the two input beam frequencies ( $\omega_{SF} = \omega_{1064\text{ nm}} + \omega_{IR}$ ). When the IR frequency is at a resonance frequency of one of the vibrational modes, an enhanced SFG signal is observed.

### **4.2.2. Factor analysis**

The theoretical background and application of factor analysis (FA) are discussed in detail by Malinowski.<sup>37</sup> A short description of the main steps are presented in Chapter 2.7. Factor analysis is a mathematical technique for studying matrices of data. It is a useful method for furnishing the number of components, concentrations, and spectral information via a purely mathematical route.<sup>37</sup> Factor analysis includes principle factor analysis (PFA), which is also known as principal component analysis (PCA), and target factor analysis (TFA). It is performed by taking a data set of interest and obtaining a mathematical solution by decomposition. Each data point of the data set, after decomposition, is expressed as a linear sum of product terms. Since the factor analytical solution is purely mathematical having no physical or chemical meaning, the resulting matrices are termed “abstract” factors. To acquire chemically recognizable factors, a transformation of the abstract factors is required. Target factor analysis uses target testing as a unique transformation method to test potential factors, and to transform the abstract factors into real factors. Target testing serves as a mathematical bridge between abstract and real factors.

### 4.3. Experimental

#### 4.3.1. Materials and sample preparation

All reagents used for self-assembled monolayers were either purchased or synthesized by T. R. Lee group (University of Houston) and used as received without any further purification. The chemicals used were octadecanethiol (ODT), 16-methoxy-hexadecane-1-thiol (MeOHT), 16,16-difluoro-octadecane-1-thiol (H2FODT), 16-phenyl-hexadecane-1-thiol (PhHDT), and carborane-1-thiol (M1CT).

SAMs on gold substrate patterning was achieved by utilizing microcontact printing ( $\mu$ CP). The stamp used for  $\mu$ CP was manufactured by mixing PDMS prepolymer (SYLGARD 184) and curing agent in a 10:1 volume ratio. The PDMS mixture was poured onto the ridged pattern which was previously treated with octadecyltrichlorosilane, an anti-adhesion layer for easy peeling of PDMS from the master pattern. The master pattern with PDMS was first placed under house vacuum for about an hour to remove bubbles produced during mixing and then cured inside the oven for 2 hours at 80 °C to ensure complete polymerization. After curing, the PDMS was cooled to room temperature, then carefully peeled off from the master pattern and cleaned by sonicating in ethanol.

The preparation procedure of the five component and the random pattern sample is schematically shown in Figure 4-1a and b, respectively, and is only briefly outlined here. Pure solutions of 20 mM ODT, MeOHT, H2FODT, PhHDT, and M1CT in ethanol were prepared. Pure alkanethiol SAMs samples for target testing library by TFA were prepared by solution deposition for 15 minutes of the respective alkanethiol solution on evaporated gold silicon wafers. For the preparation of the five component monolayer sample, a pattern from the PDMS stamp was selected and cut into four pieces. Each individual piece of the PDMS stamp was inked with a different

alkanethiol solution by placing a drop of the respective alkanethiol solution on top of the PDMS stamp and then dried by nitrogen gas. The four PDMS pieces were brought together and carefully placed on the surface of evaporated gold on silicon wafer. Light pressure was applied to the PDMS stamp and left on the surface for 15 minutes. After the stamp was removed, the sample was placed into the alkanethiol solution that was not used for stamping, to backfill bare gold regions. After 15 minute solution deposition, the sample was taken out and rinsed with ethanol and dried with nitrogen.

The random pattern sample was prepared from the same alkanethiol solutions as the five component and target test library samples. First, ODT was solution deposited onto a piece of evaporated gold substrate for 15 minutes, after which it was taken out of solution, rinsed with

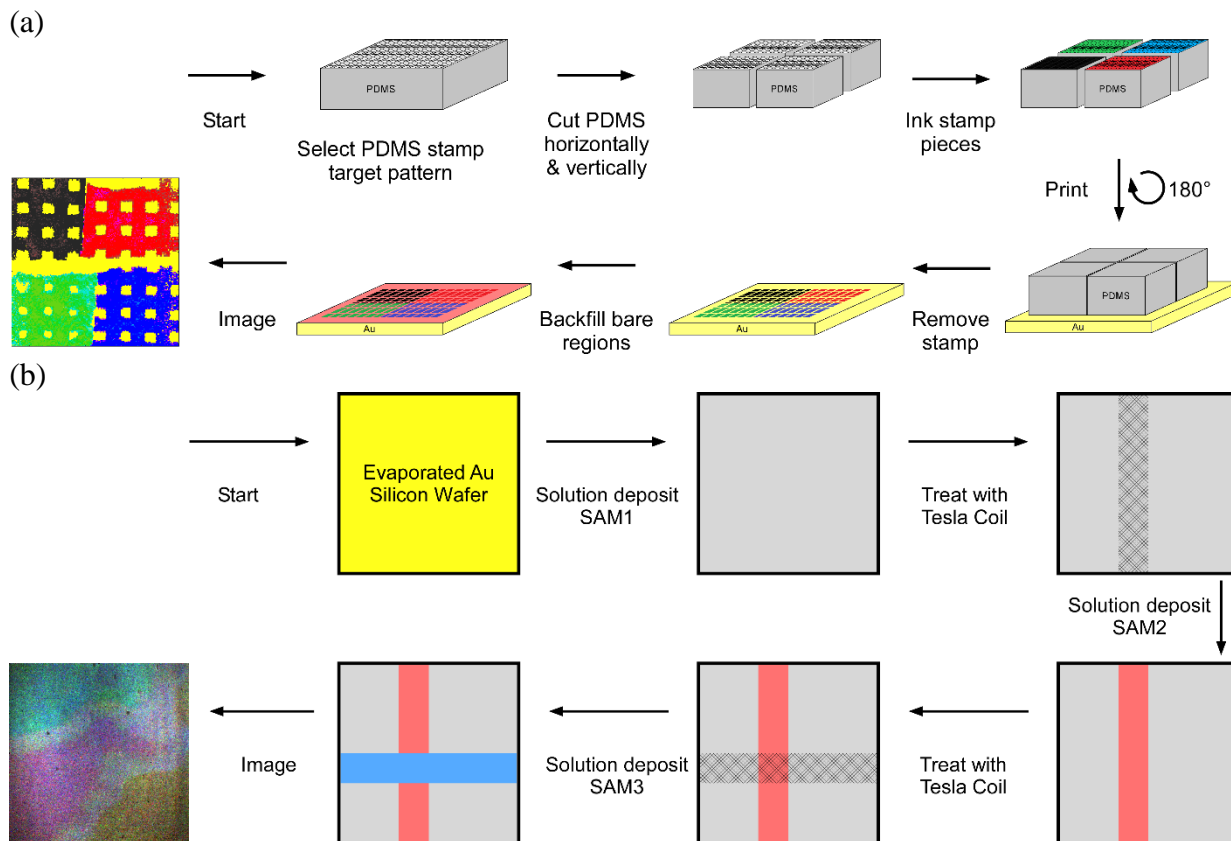


**Figure 4-1.** Schematic diagram of the preparation procedure of the (a) five component patterned sample and (b) random pattern sample.

ethanol and dried with nitrogen. Using a handheld Tesla coil to generate local plasma, a straight line was drawn across the sample while the Tesla coil tip was held at about one centimeter above the sample. After the plasma treatment, the sample was placed into the MeOHT solution for 15 minutes, after which it was taken out of solution, rinsed with ethanol and dried with nitrogen. The sample was again treated with plasma in the same manner, but with the straight line drawn perpendicular to the previous plasma treatment. The sample was then placed into the H2FODT solution. After 15 minutes, it was taken out of solution, rinsed with ethanol and dried with nitrogen. All samples were rinsed with ethanol solvent and dried with nitrogen gas before taking images.

#### **4.3.2. Sum frequency generation imaging microscope**

The SFG-IM microscope has been described previously in detail elsewhere.<sup>36, 112</sup> Briefly, a picosecond pulsed Nd:YAG laser, with a 20 Hz repetition rate, was used to generate a 1064 nm beam, part of which was used to pump the optical parametric generator/amplifier (OPG/OPA) to produce the tunable mid-IR beam. The incident angles of the 1064 nm and tunable mid-IR beams were set at 60° and 70° from the surface normal, respectively, and generated the SFG beam around 800 nm with an approximate angle of 62.1° from the surface normal. The SFG signal was collected using an intensified charge-coupled device (iCCD) detector (Roper Scientific) with a 1024 × 1024 pixel chip.

#### **4.3.3. SFG image data processing with target factor analysis**

During the SFG imaging, the iCCD detector acquired 71 SFG images sequentially, while the mid-IR frequencies were continuously scanned from 2747 to 3102 cm<sup>-1</sup> at 1000 laser shots per image. Each SFG image is an integration of 5 cm<sup>-1</sup> interval. No processing of the presented SFG images were performed except for background correction. Once the set of images was acquired, using ImageJ software, the images were stacked according to decreasing IR wavenumber. The

image stack was divide into square region of interests (ROIs) of 5-by-5 pixels, which correspond to 6.5-by-6.5  $\mu\text{m}$ , and the vibrational spectra was extracted from each ROI. Using MATLAB, the extracted spectra were normalized and compiled into a data matrix in a specified sequence, where each ROI spectrum is a column of the data matrix, on which FA was performed. The SFG image stacks of pure solution deposited alkanethiol samples were not divide into ROIs but the SFG spectra from the whole image was exacted and compiled into a library matrix in MATLAB, containing pure component spectra for TFA.

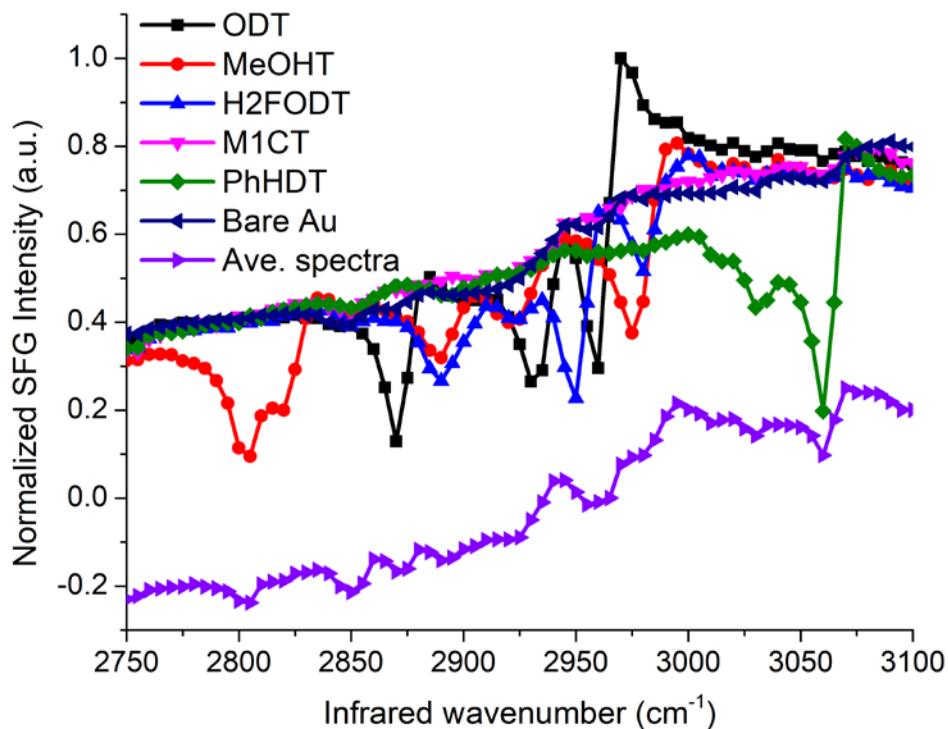
To determine the number of significant abstract factors necessary to reconstruct the data, the data matrix was decomposed via PFA, and analyzed by the factor (empirical) indicator function (IND) (See Chapter 2.7 for details on IND). To produce transformed real factors and their corresponding chemical maps, the data matrix was then analyzed by TFA. The test (target) spectra from the spectra matrix library were used to produce the transformation matrix, by converting significant abstract factors into physically significant factors. To confirm that the test spectra is a real factor in the chemical system, a SPOIL function was used to evaluate all the target spectra in the library used (See Chapter 2.7 for details on SPOIL).<sup>37</sup> The row matrix obtained from the target transformation contained the transformed (predicted) real factors, and the column matrix contained the component weights of the corresponding transformed real factors. The component weights of each real factor was reconstructed to produce the chemical maps. The chemical maps were normalized and constrained to positive values only, with no other constraints or processing. The MATLAB codes used were modified PFA and TFA codes provided by Malinowski.<sup>37</sup>

#### **4.4. Results and Discussion**

The SFG spectra of pure solution deposited alkanethiols monolayers on gold substrate that formed the SFG spectra “thiol library” were MeOHT, ODT, PhHDT, H2FODT, M1CT, and bare

gold, shown in Figure 4-2a, with the respective alkanethiol structures in Figure 4-2b. These alkanethiol spectra exhibit some distinct vibrational resonances in the C–H stretching region, 2750–3100  $\text{cm}^{-1}$ , that can be used to distinguish the alkanethiols, except for M1CT which has no distinct vibrational bands in the 2750–3100  $\text{cm}^{-1}$  region. MeOHT contains a distinct vibrational

(a)



(b)

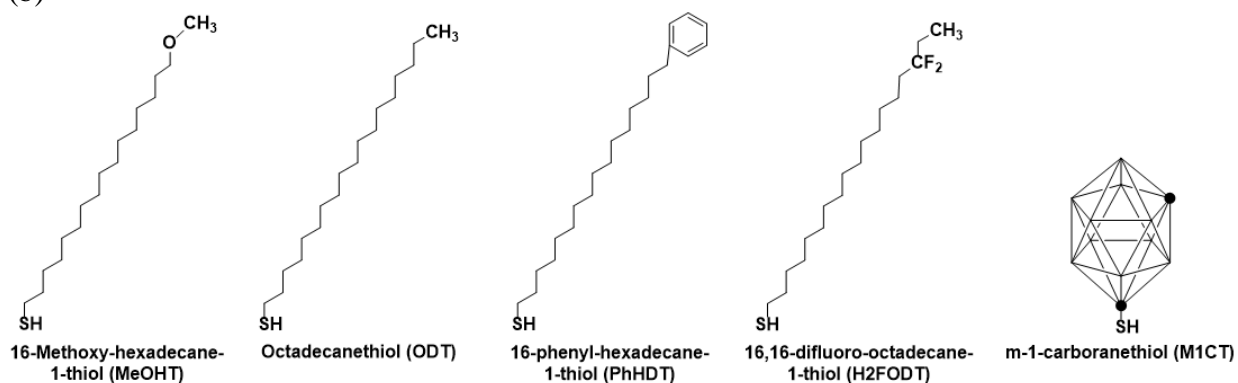


**Figure 4-2.** (a) SFG spectra of octadecanethiol (ODT), 16-methoxy-hexadecane-1-thiol (MeOHT), 16,16-difluoro-octadecane-1-thiol (H2FODT), 16-phenyl-hexadecane-1-thiol (PhHDT), m-1-carboranethiol (M1CT), and bare Au compared to averaged SFG signal, and (b) respective MeOHT, ODT, PhHDT, H2FODT, and M1CT alkanethiol structures.

symmetric stretch of the terminal methoxy (-OCH<sub>3</sub>) group as doublet at 2805/2825 cm<sup>-1</sup>, ODT has a CH<sub>3</sub> symmetric at 2870 cm<sup>-1</sup>, and PhHDT has aromatic ring stretching resonances between 3030–3060 cm<sup>-1</sup> that do not overlap with any other presented vibrational bands. The vibrational resonant stretches of the alkanethiols in the 2880–3000 cm<sup>-1</sup> range contain a significant amount of peak overlap. In the SFG images contrast is observed when there is an observable SFG signal intensity difference between the different monolayers. At frequencies where little or no relative signal difference exists, little to no image contrast is observed. In the average SFG signal of the five alkanethiols, shown below the individual alkanethiol spectra in Figure 4-2a, majority of the resonant peaks overlap and cannot be identified. In order to spectrally fit the average alkanethiol spectra to the general SFG equation, the fitting would require at least 12 terms in the equation, which makes it almost impossible to obtain a good fit. Even if the monolayers are spatially separated, the areas where the different alkanethiols meet or overlap, spectral fitting is complicated.

#### **4.4.1. Five component patterned Sample**

Analyzing the SFG image data matrix of the five component patterned sample with PFA resulted in 71 abstract factors, due to 71 frequency data points per spectrum. The IND function indicated only seven significant abstract factors that account for 97.7% of the data variance. The rest of the abstract factors that account for 2.3% were checked to contain only noise and discarded. Target testing of the thiol library to the seven significant abstract factors confirmed that all five of the tested alkanethiols were real factors of the analyzed data with their corresponding SPOIL values smaller than 20. This confirmed that independently prepared library can be used to test unknown samples. Target transformed real factors by TFA, shown in Figure 4-3a–e, overlapped well with the corresponding SFG spectra. The images in Figure 4-3f–j are the TFA resulting chem-

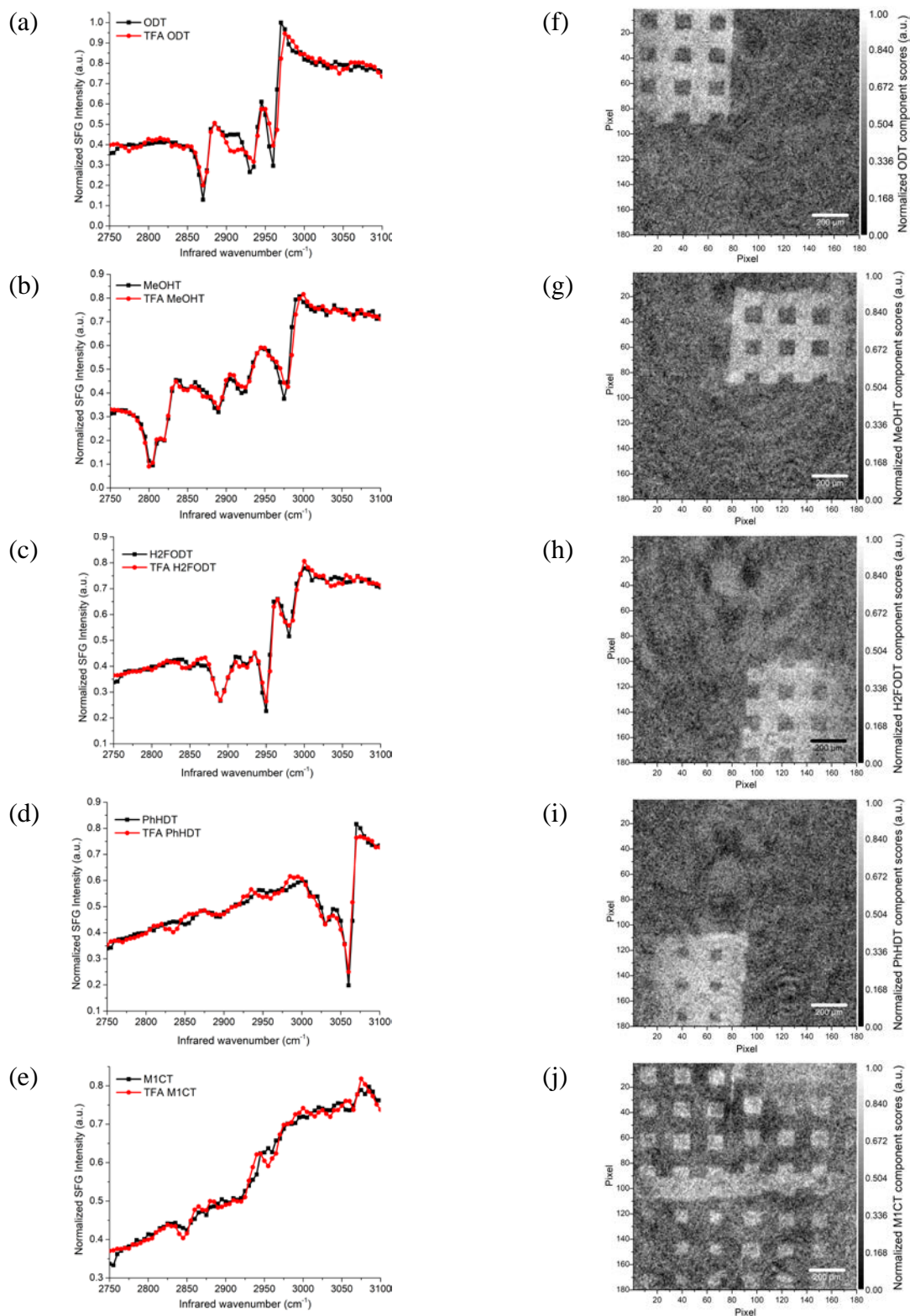


**Figure 4-3.** SFG spectra overlaid with the corresponding target transformed spectra predicted by TFA (a) ODT, (b) MeOHT, (c) H2FODT, (d) PhHDT, (e) M1CT, and corresponding reconstructed TFA chemical images of (f) ODT, (g) MeOHT, (h) H2FODT, (i) PhHDT, and (j) M1CT.

ical maps showing the spatial distribution of the real factors. The chemical maps were constructed by mapping back the component weights of each target transformed real factor in each of the 6.5-by-6.5  $\mu\text{m}$  ROIs. The lighter shaded region of each image in Figure 4-3f–j corresponds to ODT, MeOHT, H2FODT, PhHDT and M1CT region, respectively.

The normalized SFG spectrum averaged from the five component image stack is shown in Figure 4-4a. From the averaged SFG spectrum it is difficult to determine the number of different SAMs on the surface nor their identities. To visualize the distribution of the alkane thiols, selected raw SFG images of the five component sample are shown in Figure 4-4b–f. The observed contrast in the SFG images (Figure 4-4c–f) is due to the vibrational contrast in the SFG spectra, where the darker region of the images correlate to the resonant peaks of the SAMs on the surface at the

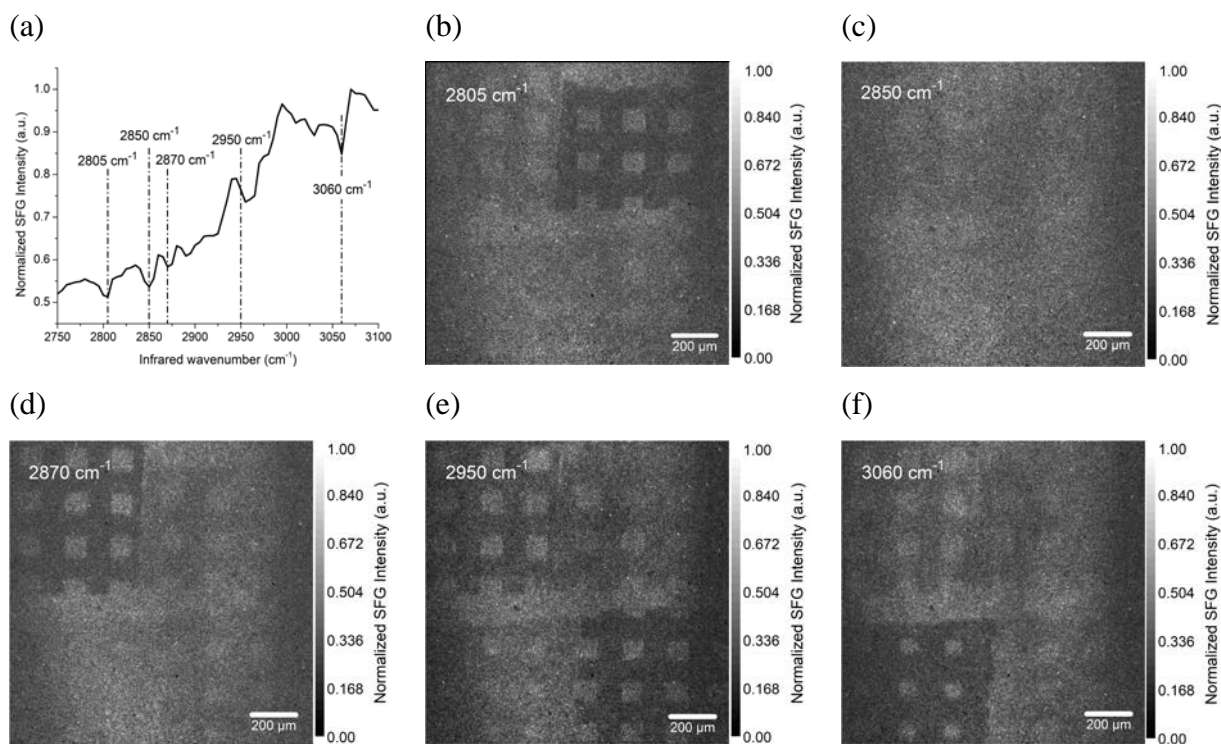


**Figure 4-4.** Normalized SFG spectrum (a), averaged over the full image, and images of the five component sample at (b) 2805  $\text{cm}^{-1}$ , (c) 2850  $\text{cm}^{-1}$ , (d) 2870  $\text{cm}^{-1}$ , (e) 2950  $\text{cm}^{-1}$ , and (f) 3060  $\text{cm}^{-1}$ .

specified frequency. Lack of unique image contrast is observed when the imaged alkanethiols show little to no vibrational resonance or very similar vibrational intensity at the specified frequency, such an example is shown in Figure 4-4b. The observed darker region in the upper right quarter of the SFG image taken at  $2805\text{ cm}^{-1}$ , Figure 4-4c, corresponds to the MeOHT covered surface, which has a symmetric methoxy stretch at that frequency. The darker region in the upper left quarter of the  $2870\text{ cm}^{-1}$  SFG image, Figure 4-4d, corresponds to the ODT region of the surface, which has a methyl symmetric stretch at that frequency. The H2FODT SAM region is the darker area in the bottom right quarter of the  $2950\text{ cm}^{-1}$  image, Figure 4-4e. The observed image contrast in the upper half of the image is due to the nonresonant SFG signal difference between the stamped ODT and MeOHT regions and the backfilled M1CT region, where M1CT has a higher nonresonant signal than ODT and MeOHT. The darker region in the bottom left quarter of the  $3060\text{ cm}^{-1}$  image, Figure 4-4f, represents the PhHDT monolayer region. Since M1CT does not contain any strong resonant vibrational bands in the selected frequency range, but mainly nonresonant signal, it is observed as the lightest region in Figure 4-4e. The spatial positions of the alkanethiols was verified by selecting the corresponding regions and analyzing the extracted vibrational spectra. The TFA chemical maps in Figure 4-3f–j, are in very good agreement with the SFG images shown in Figure 4-3c–f, indicating the capability of FA to deconvolute the spectra via SVD, predict the chemical composition, and generate chemical maps via target testing. Spectral decomposition with target testing allows the possibility to use SFG imaging to analyze more complex samples, containing multiple chemical species.

#### **4.4.2. Random pattern three component sample**

To assess the performs of TFA on a more natural system, where the spatial distribution of the molecules is unknown, a sample of randomly formed ODT, MeOHT, and H2FODT SAMs was

prepared. The SFG image stack was acquired and processed in the same manner as the patterned five component data. Principal factor analysis indicated that there were six significant abstract factors that account for 98.4% of data variance. Target testing of the alkanethiol library indicated that ODT, MeOHT, and H2FODT were real factors of the data analyzed, with corresponding SPOIL values below 20, while M1CT, PhHDT and bare Au had SPOIL values above 30, indicating that they were not real factors in the analyzed data. Target transformed real factors by TFA are shown in Figure 4-5a–e, overlapped with the corresponding SFG spectra. TFA predicted spectra were in good agreement with the corresponding SFG spectra of ODT, MeOHT, and H2FODT shown in Figure 4-5a–c, respectively. Corresponding TFA chemical maps of ODT, MeOHT, and H2FODT are shown in Figure 4-5f–h, respectively, where the lighter region of each map represents the respective SAMs coverage. TFA correctly identified that PhHDT was not a real factor since PhHDT was not used in the preparation of the sample. Aromatic ring stretching between 3030–3060  $\text{cm}^{-1}$  was not present in any of the abstract factors, and no combination of significant factors will reproduce spectra resembling PhHDT. Figure 4-5d shows PhHDT SFG spectra overlapped with the attempted TFA target transformation using PhHDT as a target, with the corresponding chemical map (Figure 4-5i), showing very weak image contrast as expected. Similarly, the SFG spectrum of M1CT did not overlap well with TFA predicted spectrum shown in Figure 4-5e.

The averaged SFG spectrum and select images representing the main vibrational frequency of ODT, MeOHT, and H2FODT of the random sample are presented in Figure 4-6. The images in Figure 4-6b–d were taken at the IR frequencies of 2805, 2870, and 2950  $\text{cm}^{-1}$ , where the darker regions of each image represent the MeOHT, ODT, and H2FODT region, respectively. The SAMs pattern observed in the presented SFG images was an unexpected pattern. Utilizing a handheld Tesla coil generates a unique, non-reproducible pattern, since there is little control on the intensity

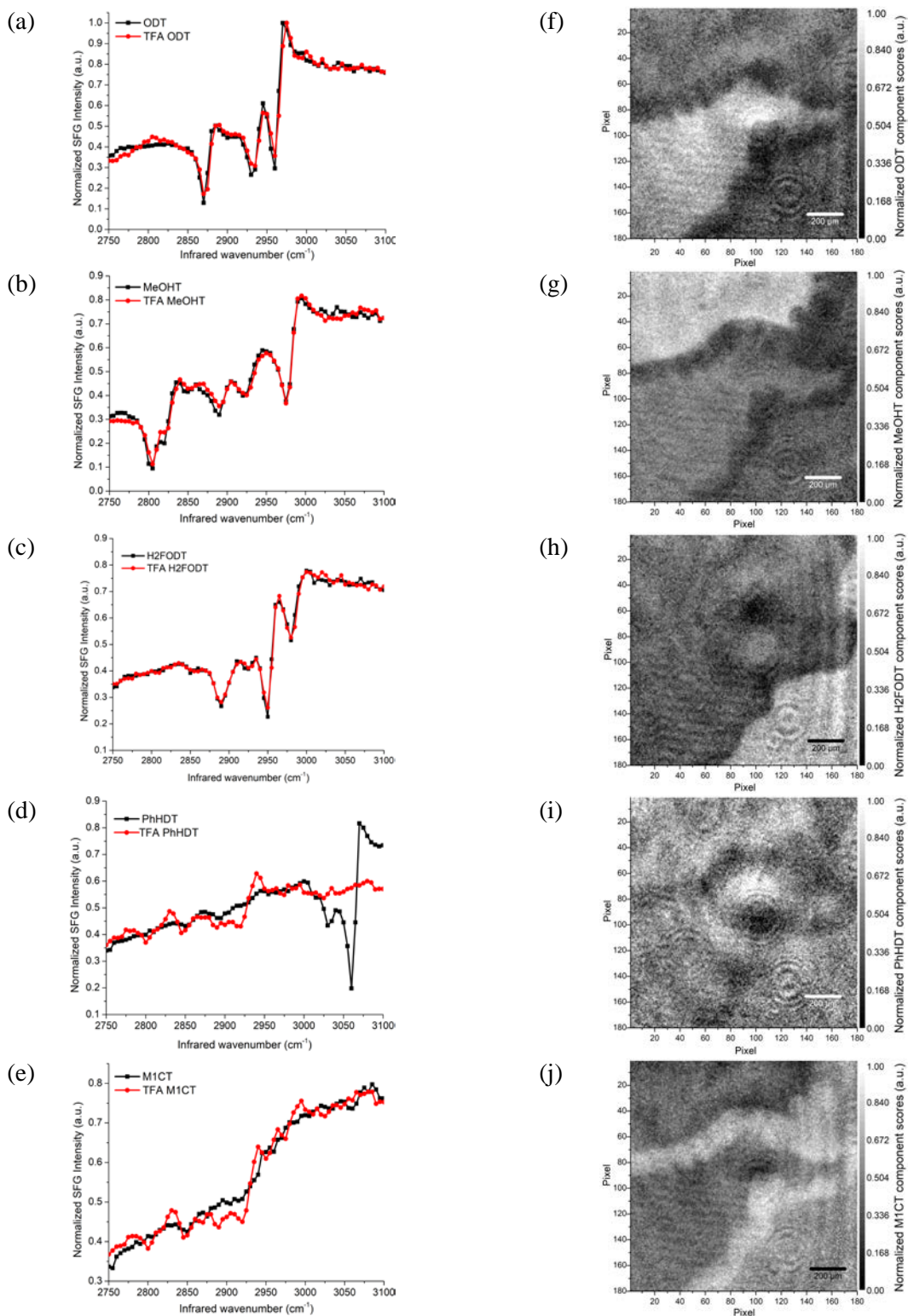


**Figure 4-5.** SFG spectra overlaid with the corresponding target transformed spectra predicted by TFA (a) ODT, (b) MeOHT, (c) H2FODT, (d) PhHDT, (e), M1CT and corresponding reconstructed TFA chemical images of (f) ODT, (g) MeOHT, (h) H2FODT, (i) PhHDT, and (j) M1CT.

and distribution of the local plasma generated. Comparison of the TFA generated ODT, MeOHT, and H2FODT chemical maps (Figure 4-5f-h) with the SFG images in Figure 4-6b-d showed good agreement. These results indicate that TFA has the sensitivity to distinguish spectral band changes and correctly (positively) determine true factors. The possibility of correctly identifying the real factors and producing chemical images that correspond to the respective SFG image chemical contrast make TFA an important tool for SFG image analysis.

In the ODT, MeOHT, and H2FODT TFA images (Figure 4-5f-h) there is an observable chemical contrast between the ODT, MeOHT, and H2FODT regions as a darkest region of the images. Surprisingly, but the contrast is also apparent in Figure 4-5i as the darker region and in Figure 4-5j as the lightest region. This observed border region contained spectral features that were not identified as one of the five alkanethiols used for target testing. SFG spectrum extracted from the border region is shown in Figure 4-7a. The faint peak at  $2810\text{ cm}^{-1}$  and a relatively large peak

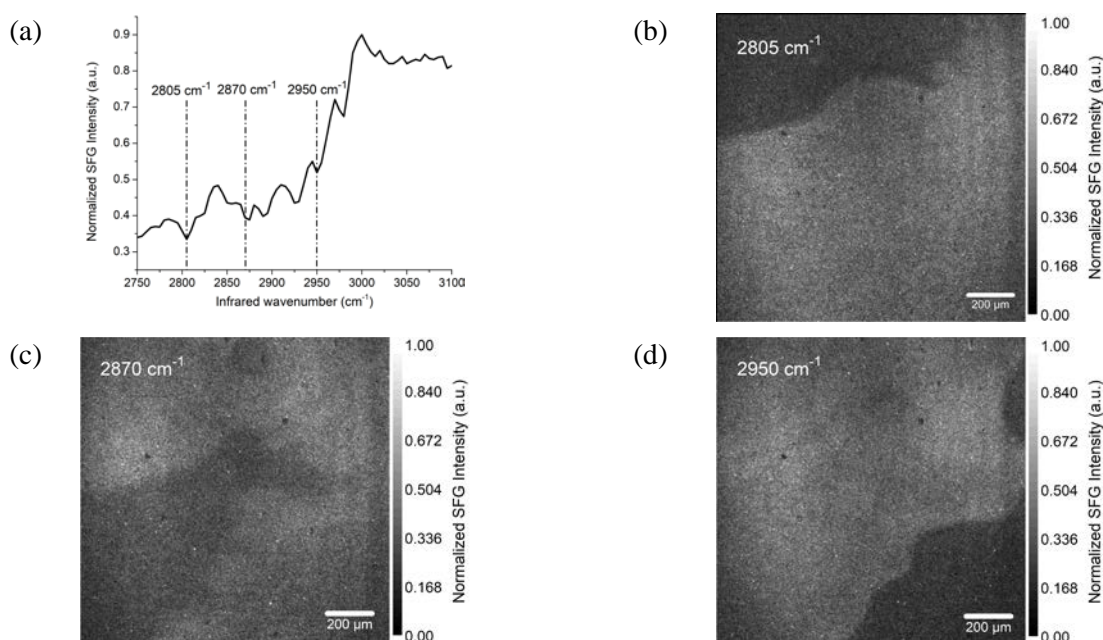


**Figure 4-6.** Normalized SFG spectrum (a) averaged over the full image, and images of the random pattern sample at (b)  $2805\text{ cm}^{-1}$ , (c)  $2870\text{ cm}^{-1}$ , and (d)  $2950\text{ cm}^{-1}$ .

at  $2850\text{ cm}^{-1}$  are observed in the MeOHT spectrum as the methoxy symmetric and  $\text{CH}_2$  symmetric stretches, respectively. The spectrum also contains a peaks at  $2895$ ,  $2950$ , and  $2980\text{ cm}^{-1}$  which are observed in H2FODT spectrum as the  $\text{CH}_2$  symmetry,  $\text{CH}_3$  symmetric, and  $\text{CH}_3$  asymmetric stretches, respectively.<sup>114-118</sup> The spectrum shows a strong  $\text{CH}_2$  symmetric stretch at  $2850\text{ cm}^{-1}$ , which is present as a minor dip in most of the alkanethiol spectra (Figure 4-2a), and indicates gauche defects in the SAMs.<sup>119-120</sup> This indicates that the border region contains highly disorder MeOHT and H2FODT molecules. This border region is faintly visible as the darker region in the SFG image at  $2850\text{ cm}^{-1}$ , shown in Figure 4-7b. The slight larger  $\text{CH}_2$  symmetric stretch in the border region compared to the other regions is responsible for the observed contrast in Figure 4-7b. This behavior of the SAMs is believed to be the result of the random pattern generation method used to prepare the sample. Target testing the extracted SFG spectrum from the border region

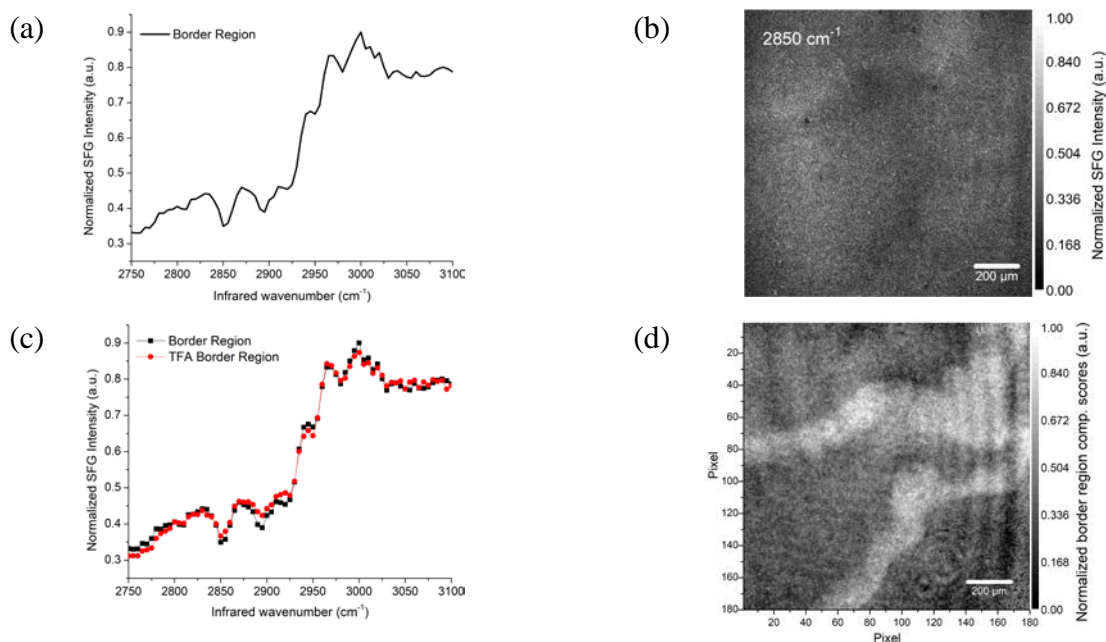


**Figure 4-7.** (a) SFG spectrum extracted from the border region of the random pattern sample and (b) SFG image at  $2850\text{ cm}^{-1}$ . (c) Border region SFG spectra overlaid with the corresponding target transformed spectra predicted by TFA and (d) corresponding chemical map.

returned a SPOIL value below 20, indicating that it was a real factor. The target transformed spectra and corresponding chemical map is shown in Figure 4-7c and d, respectively, where the lighter region of Figure 4-7d corresponds to the border region.

#### **4.5. Conclusion**

The presented work has demonstrated that FA can be successfully utilized with a spectral library to determine monolayer identities and spatial distribution. In this study, the chemical systems analyzed were a patterned five components and a random pattern. By utilizing a spectral library as a target test for TFA, the correct identification and spatial distribution of the monolayers was made possible. Also, FA was able to identify an unknown monolayer region vibrational spectra of which was not present in the target library.

Although the above observations demonstrate the potential of this technique for chemical identification and chemical map generation, it can be further improved in several ways. First, the target test library can be expanded to include more variety of vibrational spectra by using isotropic labels ( $^{13}\text{C}$ , D, and  $^{18}\text{O}$ ). This can potentially double or triple the number of molecules studied. Second, the infrared wavelength resolution can be increased to obtain narrower vibrational bands. Third, imaging resolution can be improved to resolve finer features.

## **Chapter 5: Quantification of Self-Assembled Monolayers by Sum Frequency Generation Imaging Microscopy: Factor Analysis**

### **5.1. Introduction**

Microcontact printing ( $\mu$ CP) has been widely used in the last couple of decades as a simple and efficient method to generate patterned surfaces on many different metal surfaces including gold, copper, silver, and mild steel.<sup>80-82, 121</sup> It has been utilized in numerous studies as a tool to study the surface chemistry properties via patterned alkanethiol monolayers. The procedure involves using a patterned rubber stamped and ink, where the stamp is polydimethylsiloxane (PDMS) and the ink is an alkanethiol solution. The  $\mu$ CP process involves the manufacturing of the PDMS stamp, alkanethiol inking of the stamp, and application of the stamp to the surface. During the stamping, the alkanethiols are transferred from the stamp to the surface in a mirror image of the pattern on PDMS stamp. Due to the simple and efficient method,  $\mu$ CP has been widely utilized in many studies of patterned systems.

Chemical identification, monolayer coverage, molecular orientation, and kinetics are some of the properties of alkanethiol patterned Au surfaces that have been studied by many spectroscopic, microscopic, spectrometric, and electrochemical techniques.<sup>122-123</sup> X-ray photoelectron spectroscopy (XPS) studies have provided the chemical composition, oxidation states, monolayer coverage, and thickness.<sup>122, 124-128</sup> Secondary ion mass spectrometry (SIMS) provides surface chemical composition and bonding information about surface monolayer while low energy electron diffraction (LEED) gives surface structure information.<sup>128-135</sup> Through scanning probe microscopy techniques (STM, AFM) the 2D structure of the monolayers have been determined.<sup>136-140</sup> Linear spectroscopic techniques such as Raman scattering and infrared absorption have been used to study molecular functional groups, molecular orientation, and

crystallinity.<sup>141-145</sup> Utilizing non-linear spectroscopic techniques such as second harmonic generation (SHG) and sum frequency generation (SFG), the surface coverage, surface symmetry, molecular orientation, and the monolayers' conformational order have been determined.<sup>60, 146-154</sup>

From studies of alkanethiol comparing structure of the surfaces formed by  $\mu$ CP and solution deposition, it was determined that utilizing alkanethiol solution concentrations greater than 10 mM produced monolayer coverage with the same organization and distribution of defects as those prepared by equilibration in solution.<sup>77, 155-158</sup> Low concentrations (below 10 mM) resulted in significant deviation in the order and type of order observed in the monolayers. Studies using SFG, a method directly sensitive to molecular conformation, revealed a significant degree of disorder in stamped monolayers prepared from low concentrations, indicating gauche defects.<sup>78</sup> Cimatu and Baldelli using SFG imaging microscopy (SFG-IM) observed some degree of mixing occurring between the backfilled and  $\mu$ CP monolayers.<sup>25, 34</sup>

Kinetic studies of alkanethiol adsorption from solution onto gold surfaces have shown two distinct adsorption kinetics: a very fast step, which takes a few minutes, and a slow step, which lasts several hours.<sup>146, 159-160</sup> During the first step, contact angles were observed to be close to their limiting values and the thickness was about 80—90 percent of its maximum, while by the end of the slow step, the thickness and contact angles reached their final values.<sup>161</sup> For low alkanethiol concentrations (<10 mM) the first step is achieved within 10–15 minutes.<sup>159, 162-165</sup> In contrast,  $\mu$ CP monolayers are formed on the order of seconds to minutes, with the alkanethiols transferring to the gold to form monolayers.<sup>35, 77, 81</sup>

The goal of this study was to utilize target factor analysis (TFA) to determine the percent mixing of the backfill alkanethiol into the  $\mu$ CP alkanethiol monolayer and also to observe if the mixing occurred at the same rate as solution deposition observed in previous studies. Here, SFG-

IM was used to acquire SFG images of octadecanethiol (ODT) and methoxyhexadecanethiol (MeOHT) patterned gold by  $\mu$ CP. The images were then analyzed by target factor analysis (TFA), a variant of principle component analysis, which allows the preliminary analysis of data without requiring insight into the nature of the data.<sup>37</sup> TFA has been utilized to identify components with succeeding quantitative analysis, kinetics, and reaction mechanics.<sup>38, 41, 49-50, 166-168</sup> It has been applied in chromatography and spectroscopic analysis.<sup>38-40, 112, 169</sup>

## **5.2. Experimental**

### **5.2.1. Materials and sample preparation by microcontact printing**

The PDMS stamp used for  $\mu$ CP was produced by a 10:1 volume mixture of the prepolymer and curing agent. The mixture was thoroughly mixed and placed under house vacuum for about an hour to remove air trapped during mixing. It was then poured onto a clean master pattern, which was pretreated with octadecyltrichlorosilane anti-adhesion layer. Then the master with the PDMS was placed into an oven to cure for 2 hours at 80 °C. After curing, the PDMS was carefully peeled off the surface and cleaned in ethanol.

Pure solution of 5 mM ODT and MeOHT were prepared in ethanol. The patterned sample for quantification of backfill mixing into the stamped region was prepared by placing a drop of ODT solution onto the PDMS surface containing the desired pattern and then the stamp surface was dried with nitrogen gas. Then the stamp was placed on the surface of evaporated gold on silicon for 15 minutes after which the stamp was removed and the sample was placed into the MeOHT backfill solution for 15 minutes. Target samples used for producing SFG spectra for target testing were prepared from the same solutions as the patterned sample. The ODT target sample was prepared by the same procedure detail above, using the same stamp, but without backfilling

with MeOHT. MeOHT target sample was by solution deposition for 15 minutes on evaporated gold wafer.

The patterned samples used for time dependent study were all prepared from the same solutions and with the same procedure outlined for the backfill mixing study sample. The stamping was performed using the same stamp for all samples with a fixed stamping time of 15 minutes. The backfill time was varied, where the first sample was backfilled for two minutes and the last sample was backfilled for 18 hours and 20 minutes. All samples were rinsed with ethanol and dried with nitrogen gas before taking images.

### **5.2.2. SFG image data processing with target factor analysis**

The SFG-IM was used to acquire 71 images in the 2750–3100  $\text{cm}^{-1}$  range, where each image is an integration of 5  $\text{cm}^{-1}$  interval, at a set rate of 5000 laser shots per image. No image processing was performed on the presented SFG images except for background subtraction. The images were stacked according to decreasing IR wavenumber using Image J. The vibrational spectrum was extracted by selecting a region-of-interest (ROI) on the image stack. For the determination of the percent of MeOHT mixing into the stamped ODT region, ten vibrational spectra were extracted from the mixed patterned images. The first spectrum was extracted from the stamped ROI, the last was from the MeOHT backfilled ROI, and the intermediate spectrums were extracted by shifting the ROI from the stamped ROI to the backfilled ROI in equal increments (see Figure 5-1). To determine the solution deposition rate, from each time dependent image stack, an ROI was selected from the stamped region and vibrational spectra were extracted. Using MATLAB, the extracted spectra were compiled into data matrices, where each ROI spectrum is a column of the data matrix, on which the PFA and TFA were performed. The SFG spectra extracted from the target sample image stacks were used to construct target matrix for TFA target testing.

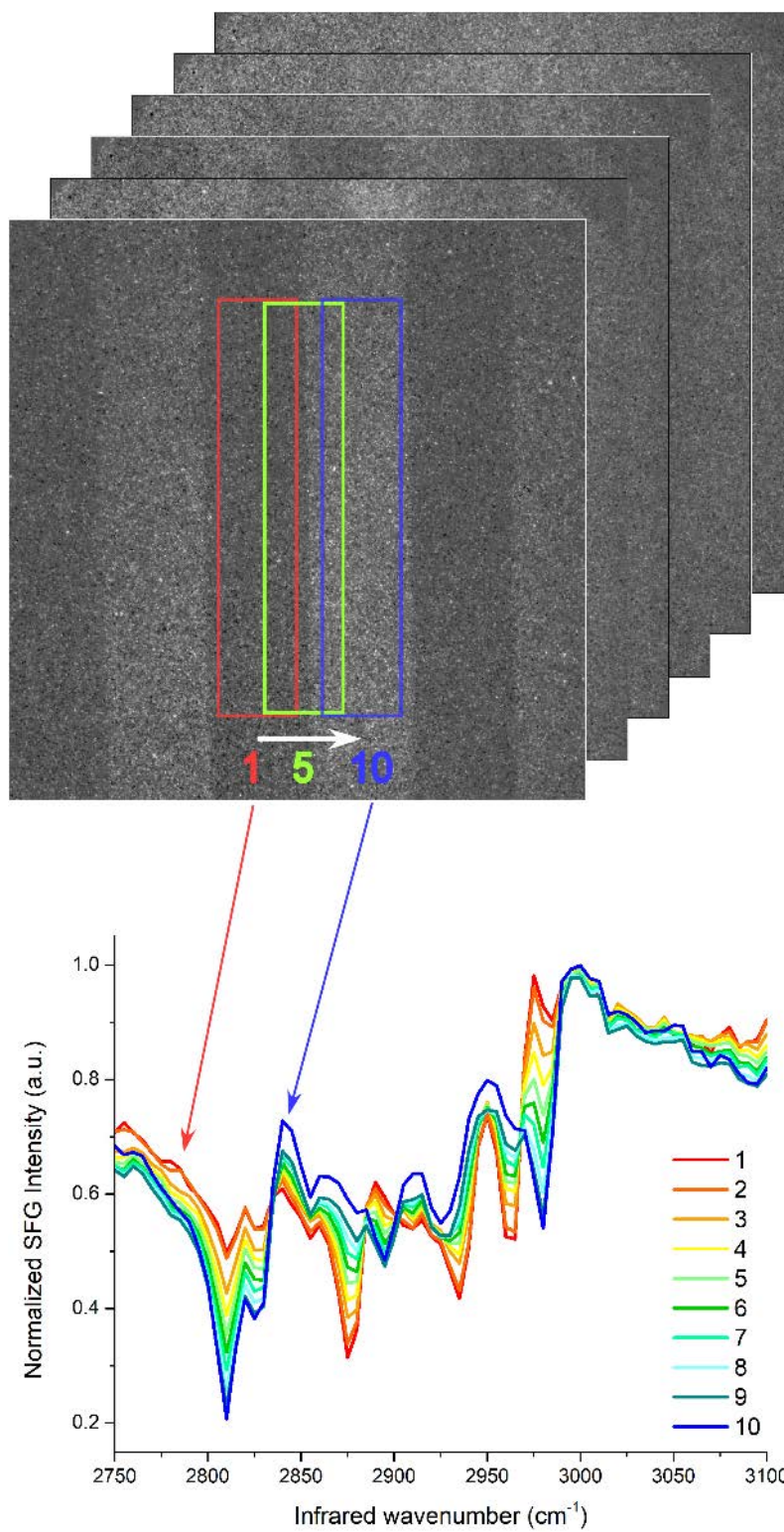


**Figure 5-1.** Illustration of image stacking and spectra extraction from ROIs.

### 5.3. Results and discussion

ODT and MeOHT were chosen as the stamping and backfilling molecules, respectively, based on previous studies that have shown that alkanethiols with higher molecular weight, low vapor pressure under ambient condition, and longer alkane chains produce robust, reliable, and well-ordered monolayer patterns.<sup>170-171</sup> SFG images and spectra from the  $\mu$ CP ODT-MeOHT mixed sample are presented in Figure 5-2. Figures 5-2a,b, and c show SFG images representative of 2810, 2875 and 2945  $\text{cm}^{-1}$  respectively and spectra shown in Figures 5-2d and 5-2e were extracted from the ROI highlighted in Figures 5-2a and 5-2b respectively. The observed image contrast is due to the vibrational contrast in the SFG spectra, where the dark areas in the images are related to the resonance peaks in the SAMs.<sup>34</sup> ODT and MeOHT exhibit distinct vibrational spectra in the 2800 to 3000  $\text{cm}^{-1}$  region that can be used to distinguish the two molecules apart. In the C-H stretching region, MeOHT contains six vibrational modes, which are the symmetric stretch of the  $\text{CH}_3$  in the terminal methoxy group,  $\text{CH}_2$  symmetric and asymmetric stretches, Fermi

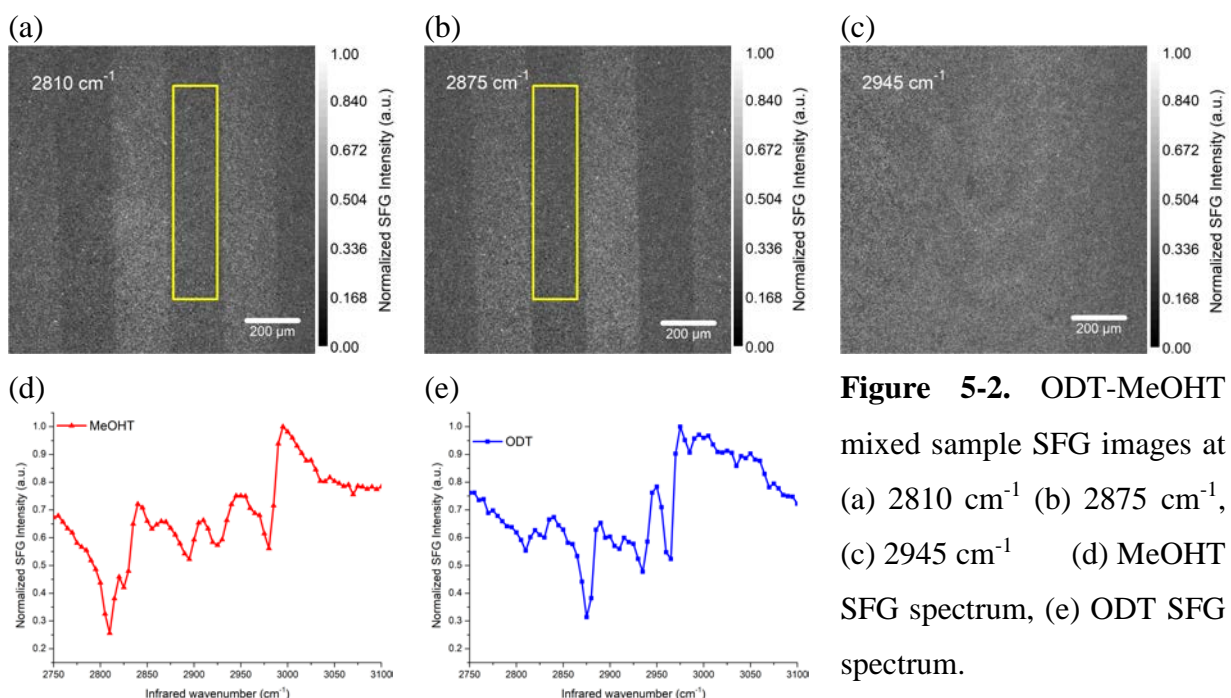


**Figure 5-2.** ODT-MeOHT mixed sample SFG images at (a) 2810  $\text{cm}^{-1}$  (b) 2875  $\text{cm}^{-1}$ , (c) 2945  $\text{cm}^{-1}$  (d) MeOHT SFG spectrum, (e) ODT SFG spectrum.

resonance, and the CH<sub>3</sub> antisymmetric stretch observed at 2810, 2830, 2855, 2900, 2930, and 2980 cm<sup>-1</sup>, respectively. The vibrational modes of ODT observed at 2875, 2935, 2965, and 2975 cm<sup>-1</sup> are the CH<sub>3</sub> symmetric stretch, Fermi resonance, and the antisymmetric in-plane and out of plane stretching of the terminal methyl group, respectively. The observed dark areas of the SFG images at 2810 and 2875 cm<sup>-1</sup> correspond to the MeOHT and ODT surface coverage, respectively. When both the MeOHT and ODT are off vibrational resonant frequencies, no image contrast is observed. An example of an off vibrational resonant image is shown in Figure 5-2c.

### 5.3.1. Mixing in stamped region

Figure 5-3 shows overlapped SFG vibrational spectra of MeOHT and ODT from Figure 5-2d and 5-2e, with stamped ODT only obtained from the ODT target sample. Spectra from the stamped ODT target and ODT from mixed sample differ slightly, where the mixed ODT contains MeOHT peaks at 2810 and 2825 cm<sup>-1</sup> which are not observed in the ODT target spectrum but is

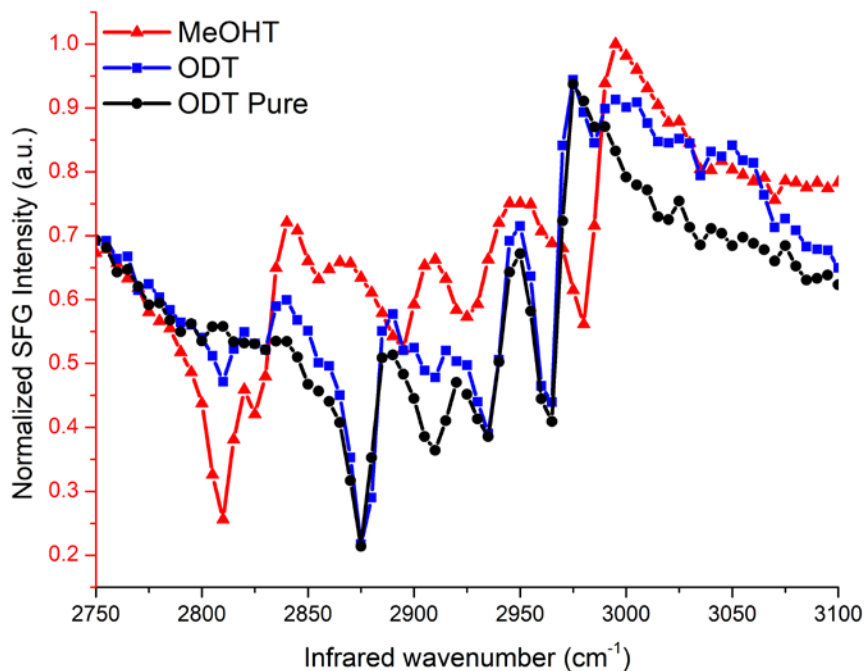


**Figure 5-3.** SFG spectra of stamped ODT and solution deposited MeOHT, and stamped ODT pure, without backfill.

observed in the MeOHT spectrum. These peaks suggest that mixing occurs during the backfill step. It has been reported previously that overall monolayers formed by microcontact printing are less densely packed than those from solution-deposited films, indicating gauche defects or defect in stamp.<sup>25, 34, 78</sup> Cimatu and Baldelli reported mixing of backfill in the microcontract stamped region of a hexadecanethiol–phenylhexadecanethiol sample. On the basis of the amplitude ratio of the phenyl peak in the two phases, they reported that the phenyl coverage in the CH<sub>3</sub> phase was about 1/12<sup>th</sup> of that in the pure phenyl phase.<sup>25</sup>

Target factor analysis was used to determine the percent of MeOHT coverage in the ODT stamped region. The ten spectra extracted from the mixed patterned sample are shown in Figure 5-4a. The first spectra, extracted from the stamped ODT region, contains weak MeOHT resonant peaks. Moving the ROI incrementally from the stamped ODT region to the MeOHT region, the MeOHT resonant peaks increase while the ODT peaks decrease. In the final spectra, extracted from the MeOHT backfill region, no ODT resonant peaks are observed. Applying TFA with target ODT and MeOHT spectra allowed to determine the amount of MeOHT mixing into the ODT

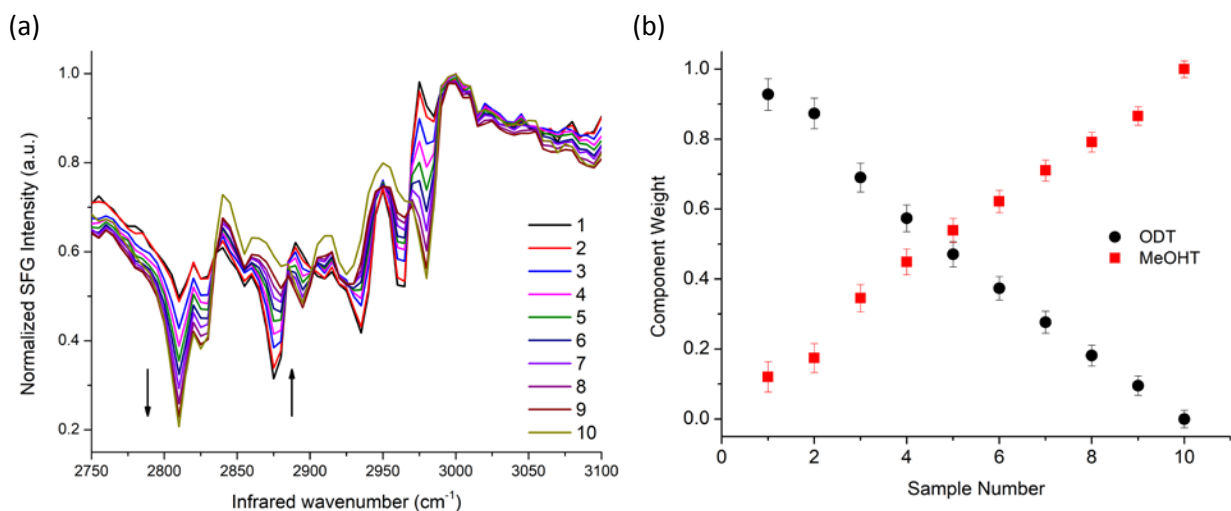


**Figure 5-4.** (a) SFG spectra of patterned sample extracted from ROI (b) Component weight of MeOHT in ODT stamped region.

stamped region. The result from TFA are shown in Figure 5-4b as the componential weight of the ODT and MeOHT contribution to each extracted ROI spectrum in Figure 5-4a. Based on the TFA results, the MeOHT coverage in the stamped ODT region is about 12 percent of that in the pure MeOHT region, which is in close agreement to the results published by Cimatu and Baldelli.<sup>25</sup> These results reflect the percent mixing in sample prepared from low concentration alkanethiol solutions.

### 5.3.2. Effect of backfill time on mixing

To determine if the mixing of the backfill methoxy-terminated alkanethiol followed the two-step mechanism observed for pure solution deposition, SFG spectrum was taken of ODT-MeOHT patterned samples, where the time duration the sample was backfilled was varied from no backfill to over 18 hours. The time dependent SFG spectra extracted from the ODT stamped region is shown in Figure 5-5a. The intensity of the methoxy stretch of MeOHT observed at 2810  $\text{cm}^{-1}$  increases with longer deposition times in MeOHT. The increased intensity of the peak indicates an increase in amount of MeOHT mixing into the ODT stamped region. Using pure

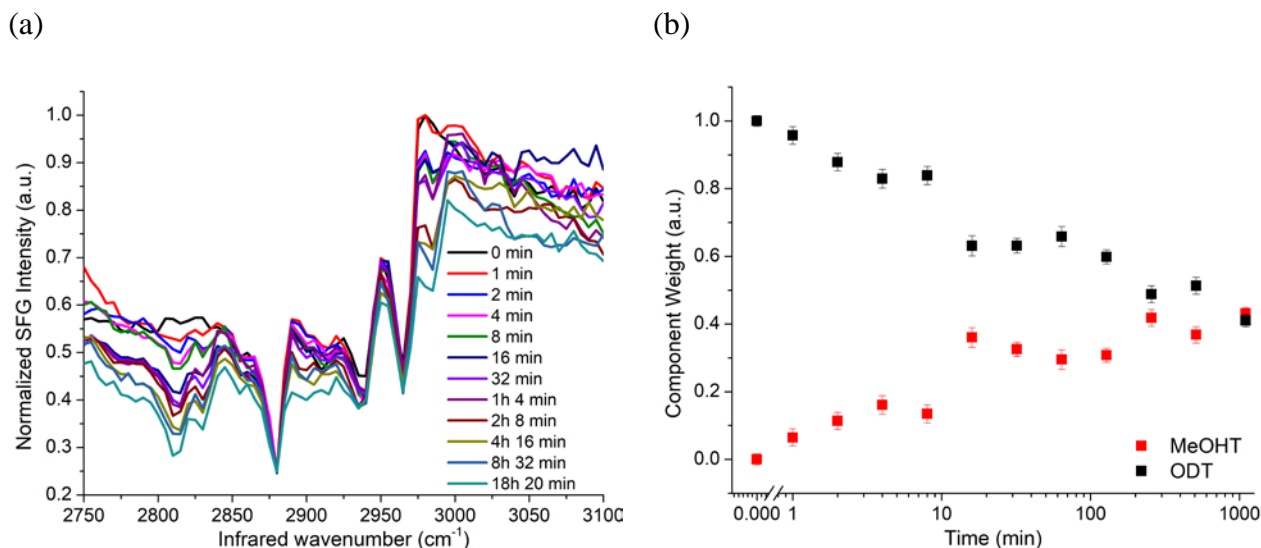


**Figure 5-5.** (a) SFG spectra of time varied backfill and (b) the TFA results.

solution deposited ODT and MeOHT spectra as targets for TFA analysis, the component weight of ODT and MeOHT was determined in each time spectra. Based on the results of TFA, shown in Figure 5-5b, the component weight of MeOHT in the ODT stamped region shows a two-step adsorption process similar to solution deposition kinetics. The first step reaches a stable point after about 16 minutes, and the second step requires at least 8 hours.

#### **5.4. Conclusion**

The amount of solution deposited backfill mixing into the stamped region and the absorption kinetics obtained by TFA correlate with previous studies. The 12 percent backfill mixing into the  $\mu$ CP stamped region, quantified by TFA, results are representative of low concentration solutions. Since stamped monolayers formed from low concentration were shown to exhibit lower density/coverage, using higher solution concentrations (>10 mM) for stamping would most likely result in a denser stamped monolayer and reduce the amount of backfill mixing into the stamped region.

## Bibliography

- (1) Somorjai, G. A.; Li, Y., *Introduction to surface chemistry and catalysis*. 2nd ed.; Wiley: Hoboken, N.J., 2010; p xii, 771 p.
- (2) Somorjai, G. A.; Li, Y. M., Impact of surface chemistry. *P Natl Acad Sci USA* **2011**, *108* (3), 917-924.
- (3) Zharnikov, M.; Shaporenko, A.; Paul, A.; Golzhauser, A.; Schow, A., X-ray absorption spectromicroscopy studies for the development of lithography with a monomolecular resist. *J Phys Chem B* **2005**, *109* (11), 5168-5174.
- (4) Klauser, R.; Hong, I. H.; Wang, S. C.; Zharnikov, M.; Paul, A.; Golzhauser, A.; Terfort, A.; Chuang, T. J., Imaging and patterning of monomolecular resists by zone-plate-focused x-ray microprobe. *J Phys Chem B* **2003**, *107* (47), 13133-13142.
- (5) Vericat, C.; Vela, M. E.; Benitez, G. A.; Gago, J. A. M.; Torrelles, X.; Salvarezza, R. C., Surface characterization of sulfur and alkanethiol self-assembled monolayers on au(111). *J Phys-Condens Mat* **2006**, *18* (48), R867-R900.
- (6) Grunthaner, F. J.; Grunthaner, P. J.; Vasquez, R. P.; Lewis, B. F.; Maserjian, J.; Madhukar, A., High-resolution x-ray photoelectron-spectroscopy as a probe of local atomic-structure - application to amorphous sio<sub>2</sub> and the si-sio<sub>2</sub> interface. *Phys Rev Lett* **1979**, *43* (22), 1683-1686.
- (7) Toselli, M.; Gardella, J. A.; Messori, M.; Hawkrige, A. M.; Pilati, F.; Tonelli, C., Surface chemical analysis of poly(epsilon-caprolactone)-perfluoropolyether-poly(epsilon-caprolactone) triblock copolymers by x-ray photoelectron spectroscopy. *Polym Int* **2003**, *52* (8), 1262-1274.
- (8) Vickerman, J. C.; Gilmore, I. S., *Surface analysis : The principal techniques*. 2nd ed.; Wiley: Chichester, U.K., 2009; p xix, 666 p.
- (9) Woodruff, D. P.; Delchar, T. A., *Modern techniques of surface science*. 2nd ed.; Cambridge University Press: Cambridge ; New York, 1994; p xviii, 586 p.
- (10) Bain, C. D., Sum-frequency vibrational spectroscopy of the solid-liquid interface. *J Chem Soc Faraday T* **1995**, *91* (9), 1281-1296.
- (11) Sahlin, J. J.; Peppas, N. A., Near-field ftir imaging: A technique for enhancing spatial resolution in ftir microscopy. *J Appl Polym Sci* **1997**, *63* (1), 103-110.
- (12) Kazarian, S. G.; Chan, K. L. A., Applications of atr-ftir spectroscopic imaging to biomedical samples. *Bba-Biomembranes* **2006**, *1758* (7), 858-867.

- (13) Ray, K.; McCreery, R. L., Spatially resolved raman spectroscopy of carbon electrode surfaces: Observations of structural and chemical heterogeneity. *Anal Chem* **1997**, *69* (22), 4680-4687.
- (14) Treado, P. J.; Govil, A.; Morris, M. D.; Sternitzke, K. D.; McCreery, R. L., Hadamard-transform raman microscopy of laser-modified graphite-electrodes. *Appl Spectrosc* **1990**, *44* (8), 1270-1275.
- (15) Zumbusch, A.; Holtom, G. R.; Xie, X. S., Three-dimensional vibrational imaging by coherent anti-stokes raman scattering. *Phys Rev Lett* **1999**, *82* (20), 4142-4145.
- (16) Cheng, J. X.; Volkmer, A.; Book, L. D.; Xie, X. S., An epi-detected coherent anti-stokes raman scattering (e-cars) microscope with high spectral resolution and high sensitivity. *J Phys Chem B* **2001**, *105* (7), 1277-1280.
- (17) Cheng, J. X.; Volkmer, A.; Book, L. D.; Xie, X. S., Multiplex coherent anti-stokes raman scattering microspectroscopy and study of lipid vesicles. *J Phys Chem B* **2002**, *106* (34), 8493-8498.
- (18) Cheng, J. X.; Xie, X. S., Coherent anti-stokes raman scattering microscopy: Instrumentation, theory, and applications. *J Phys Chem B* **2004**, *108* (3), 827-840.
- (19) Potma, E. O.; Xie, X. S.; Muntean, L.; Preusser, J.; Jones, D.; Ye, J.; Leone, S. R.; Hinsberg, W. D.; Schade, W., Chemical imaging of photoresists with coherent anti-stokes raman scattering (cars) microscopy. *J Phys Chem B* **2004**, *108* (4), 1296-1301.
- (20) Zhu, X. D.; Suhr, H.; Shen, Y. R., Surface vibrational spectroscopy by infrared-visible sum frequency generation. *Phys Rev B* **1987**, *35* (6), 3047-3050.
- (21) Wang, H. F.; Gan, W.; Lu, R.; Rao, Y.; Wu, B. H., Quantitative spectral and orientational analysis in surface sum frequency generation vibrational spectroscopy (sfg-vs). *Int Rev Phys Chem* **2005**, *24* (2), 191-256.
- (22) Wang, H. F., Sum frequency generation vibrational spectroscopy (sfg-vs) for complex molecular surfaces and interfaces: Spectral lineshape measurement and analysis plus some controversial issues. *Prog Surf Sci* **2016**, *91* (4), 155-182.
- (23) Florsheimer, M.; Brillert, C.; Fuchs, H., Chemical imaging of interfaces by sum-frequency generation. *Mat Sci Eng C-Bio S* **1999**, *8-9*, 335-341.
- (24) Hoffmann, D. M. P.; Kuhnke, K.; Kern, K., Chemical imaging of structured sams with a novel sfg microscope. *Proc Spie* **2002**, *4812*, 82-90.
- (25) Cimatu, K.; Baldelli, S., Sum frequency generation microscopy of microcontact-printed mixed self-assembled monolayers. *J Phys Chem B* **2006**, *110* (4), 1807-1813.

- (26) Cimatu, K.; Baldelli, S., Sum frequency generation imaging microscopy of co on platinum. *J Am Chem Soc* **2006**, *128* (50), 16016-16017.
- (27) Fang, M.; Baldelli, S., Surface-induced heterogeneity analysis of an alkanethiol monolayer on microcrystalline copper surface using sum frequency generation imaging microscopy. *J Phys Chem C* **2017**, *121* (3), 1591-1601.
- (28) Kuhnke, K.; Hoffmann, D. M. P.; Wu, X. C.; Bittner, A. M.; Kern, K., Chemical imaging of interfaces by sum-frequency generation microscopy: Application to patterned self-assembled monolayers. *Appl Phys Lett* **2003**, *83* (18), 3830-3832.
- (29) Bain, C. D.; Whitesides, G. M., Modeling organic-surfaces with self-assembled monolayers. *Angew Chem Int Edit* **1989**, *28* (4), 506-512.
- (30) Schreiber, F., Self-assembled monolayers: From 'simple' model systems to biofunctionalized interfaces. *J Phys-Condens Mat* **2004**, *16* (28), R881-R900.
- (31) Smith, R. K.; Lewis, P. A.; Weiss, P. S., Patterning self-assembled monolayers. *Prog Surf Sci* **2004**, *75* (1-2), 1-68.
- (32) Whitesides, G. M.; Grzybowski, B., Self-assembly at all scales. *Science* **2002**, *295* (5564), 2418-2421.
- (33) Nuzzo, R. G.; Dubois, L. H.; Allara, D. L., Fundamental-studies of microscopic wetting on organic-surfaces .1. Formation and structural characterization of a self-consistent series of polyfunctional organic monolayers. *J Am Chem Soc* **1990**, *112* (2), 558-569.
- (34) Cimatu, K.; Moore, H. J.; Barriet, D.; Chinwangso, P.; Lee, T. R.; Baldelli, S., Sum frequency generation imaging microscopy of patterned self-assembled monolayers with terminal -ch<sub>3</sub>, -och<sub>3</sub>, -cf<sub>2</sub>cf<sub>3</sub>, -c = c, -phenyl, and -cyclopropyl groups. *J Phys Chem C* **2008**, *112* (37), 14529-14537.
- (35) Love, J. C.; Estroff, L. A.; Kriebel, J. K.; Nuzzo, R. G.; Whitesides, G. M., Self-assembled monolayers of thiolates on metals as a form of nanotechnology. *Chem Rev* **2005**, *105* (4), 1103-1169.
- (36) Cimatu, K. A.; Baldelli, S., Chemical microscopy of surfaces by sum frequency generation imaging. *J Phys Chem C* **2009**, *113* (38), 16575-16588.
- (37) Malinowski, E. R., *Factor analysis in chemistry*. 3rd ed.; Wiley: New York, 2002; p xviii, 414 p.
- (38) Mccue, M.; Malinowski, E. R., Target factor-analysis of infrared-spectra of multicomponent mixtures. *Anal Chim Acta-Comp* **1981**, *5* (2), 125-136.

- (39) Ngo, D.; Baldelli, S., Adsorption of dimethyldodecylamine oxide and its mixtures with triton x-100 at the hydrophilic silica/water interface studied using total internal reflection raman spectroscopy. *J Phys Chem B* **2016**, *120* (48), 12346-12357.
- (40) Woods, D. A.; Petkov, J.; Bain, C. D., Surfactant adsorption by total internal reflection raman spectroscopy. Part iii: Adsorption onto cellulose. *Colloid Surface A* **2011**, *391* (1-3), 10-18.
- (41) Day, J. P. R.; Campbell, R. A.; Russell, O. P.; Bain, C. D., Adsorption kinetics in binary surfactant mixtures studied with external reflection ftir spectroscopy. *J Phys Chem C* **2007**, *111* (25), 8757-8774.
- (42) Lewis, I. R.; Edwards, H. G. M., *Handbook of raman spectroscopy: From the research laboratory to the process line*. Marcel Dekker: New York, 2001; p xiii, 1054 p.
- (43) Geladi, P.; Sethson, B.; Nystrom, J.; Lillhonga, T.; Lestander, T.; Burger, J., Chemometrics in spectroscopy - part 2. Examples. *Spectrochim Acta B* **2004**, *59* (9), 1347-1357.
- (44) Larrechi, M. S.; Callao, M. P., Strategy for introducing nir spectroscopy and multivariate calibration techniques in industry. *Trac-Trend Anal Chem* **2003**, *22* (9), 634-640.
- (45) vandenBroek, W. H. A. M.; Derks, E. P. P. A.; vandeVen, E. W.; Wienke, D.; Geladi, P.; Buydens, L. M. C., Plastic identification by remote sensing spectroscopic nir imaging using kernel partial least squares (kpls). *Chemometr Intell Lab* **1996**, *35* (2), 187-197.
- (46) Koons, J. M.; Ellis, P. D., Applicability of factor-analysis in solid-state nmr. *Anal Chem* **1995**, *67* (23), 4309-4315.
- (47) Weiner, P. H.; Howery, D. G., Factor-analysis of some chemical and physical influences in gas-liquid chromatography. *Anal Chem* **1972**, *44* (7), 1189-&.
- (48) Mccue, M.; Malinowski, E. R., Target factor-analysis of the ultraviolet-spectra of unresolved liquid-chromatographic fractions. *Appl Spectrosc* **1983**, *37* (5), 463-469.
- (49) Malinowski, E. R.; Mccue, M., Qualitative and quantitative-determination of suspected components in mixtures by target transformation factor-analysis of their mass-spectra. *Anal Chem* **1977**, *49* (2), 284-287.
- (50) Shao, L. M.; Griffiths, P. R., Information extraction from a complex multicomponent system by target factor analysis. *Anal Chem* **2010**, *82* (1), 106-114.
- (51) Carvalho, A. R.; Wattoo, J.; Zhu, L. F.; Brereton, R. G., Combined kinetics and iterative target transformation factor analysis for spectroscopic monitoring of reactions. *Analyst* **2006**, *131* (1), 90-97.

- (52) Zhu, L. F.; Brereton, R. G.; Thompson, D. R.; Hopkins, P. L.; Escott, R. E. A., On-line hplc combined with multivariate statistical process control for the monitoring of reactions. *Anal Chim Acta* **2007**, *584* (2), 370-378.
- (53) Pachuta, S. J., Enhancing and automating tof-sims data interpretation using principal component analysis. *Appl Surf Sci* **2004**, *231*, 217-223.
- (54) Boyd, R. W., *Nonlinear optics*. 3rd ed.; Academic Press: Amsterdam ; Boston, 2008; p xix, 613 p.
- (55) Hirose, C.; Akamatsu, N.; Domen, K., Formulas for the analysis of the surface sfg spectrum and transformation coefficients of cartesian sfg tensor components. *Appl Spectrosc* **1992**, *46* (6), 1051-1072.
- (56) Lambert, A. G.; Davies, P. B.; Neivandt, D. J., Implementing the theory of sum frequency generation vibrational spectroscopy: A tutorial review. *Appl Spectrosc Rev* **2005**, *40* (2), 103-145.
- (57) Zhang, H. P.; Romero, C.; Baldelli, S., Preparation of alkanethiol monolayers on mild steel surfaces studied with sum frequency generation and electrochemistry. *J Phys Chem B* **2005**, *109* (32), 15520-15530.
- (58) Hunt, J. H.; Guyotsionnest, P.; Shen, Y. R., Observation of c-h stretch vibrations of monolayers of molecules optical sum-frequency generation. *Chem Phys Lett* **1987**, *133* (3), 189-192.
- (59) Shen, Y. R., *The principles of nonlinear optics*. Wiley classics library ed.; Wiley-Interscience: Hoboken, N.J., 2003; p xii, 563 p.
- (60) Bain, C. D.; Davies, P. B.; Ong, T. H.; Ward, R. N.; Brown, M. A., Quantitative-analysis of monolayer composition by sum-frequency vibrational spectroscopy. *Langmuir* **1991**, *7* (8), 1563-1566.
- (61) Nishida, T.; Johnson, C. M.; Holman, J.; Osawa, M.; Davies, P. B.; Ye, S., Optical sum-frequency emission from langmuir-blodgett films of variable thickness: Effects of the substrate and polar orientation of fatty acids in the films. *Phys Rev Lett* **2006**, *96* (7).
- (62) Duffy, D. C.; Davies, P. B.; Bain, C. D., Surface vibrational spectroscopy of organic counterions bound to a surfactant monolayer. *J Phys Chem-Us* **1995**, *99* (41), 15241-15246.
- (63) Ward, R. N.; Duffy, D. C.; Davies, P. B.; Bain, C. D., Sum-frequency spectroscopy of surfactants adsorbed at a flat hydrophobic surface. *J Phys Chem-Us* **1994**, *98* (34), 8536-8542.

- (64) Ward, R. N.; Davies, P. B.; Bain, C. D., Orientation of surfactants adsorbed on a hydrophobic surface. *J Phys Chem-Us* **1993**, *97* (28), 7141-7143.
- (65) *Laser pl2143a/20 technical description & user's manual*. EKSPLA: 2001.
- (66) Koechner, W., *Solid-state laser engineering*. 5th rev. and updated ed.; Springer: Berlin ; New York, 1999; p xi, 746 p.
- (67) Zhang, J.-y.; Huang, J. Y.; Shen, Y. R., *Optical parametric generation and amplification*. Harwood Academic Publishers: Australia ; United States, 1995; p vii, 70 p.
- (68) Cimatu, K. L. A. Sum frequency generation imaging microscopy. Ph D, University of Houston, 2008.
- (69) Fang, M. Surface chemistry on the heterogeneous metal surface investigated by the sum frequency generation microscope. Ph D, University of Houston, 2016.
- (70) Sun, Z.; Zheng, D. S.; Baldelli, S., Distortion correction for a Brewster angle microscope using an optical grating. *Anal Chem* **2017**, *89* (4), 2186-2190.
- (71) *Princeton instruments pi-max4 camera system: User manual*. Roper Scientific: 2016.
- (72) *Princeton instruments pi-max4: 1024i*. N3 ed.; Roper Scientific: 2014.
- (73) Rostami, A.; Abdollahi, H.; Maeder, M., Enhanced target factor analysis. *Anal Chim Acta* **2016**, *911*, 35-41.
- (74) Press, W. H., *Numerical recipes : The art of scientific computing*. 3rd ed.; Cambridge University Press: Cambridge, UK ; New York, 2007; p xxi, 1235 p.
- (75) Xia, Y. N.; Whitesides, G. M., Soft lithography. *Angewandte Chemie-International Edition* **1998**, *37* (5), 550-575.
- (76) Libioulle, L.; Bietsch, A.; Schmid, H.; Michel, B.; Delamarche, E., Contact-inking stamps for microcontact printing of alkanethiols on gold. *Langmuir* **1999**, *15* (2), 300-304.
- (77) Larsen, N. B.; Biebuyck, H.; Delamarche, E.; Michel, B., Order in microcontact printed self-assembled monolayers. *J Am Chem Soc* **1997**, *119* (13), 3017-3026.
- (78) Bohm, I.; Lampert, A.; Buck, M.; Eisert, F.; Grunze, M., A spectroscopic study of thiol layers prepared by contact printing. *Appl Surf Sci* **1999**, *141* (3-4), 237-243.
- (79) Cimatu, K.; Baldelli, S., Spatially resolved surface analysis of an octadecanethiol self-assembled monolayer on mild steel using sum frequency generation imaging microscopy. *J Phys Chem C* **2007**, *111* (19), 7137-7143.

- (80) Kumar, A.; Biebuyck, H. A.; Whitesides, G. M., Patterning self-assembled monolayers - applications in materials science. *Langmuir* **1994**, *10* (5), 1498-1511.
- (81) Ruiz, S. A.; Chen, C. S., Microcontact printing: A tool to pattern. *Soft Matter* **2007**, *3* (2), 168-177.
- (82) Thakar, R.; Baker, L. A., Lithography-free production of stamps for microcontact printing of arrays. *Anal Methods-Uk* **2010**, *2* (8), 1180-1183.
- (83) Shadnam, M. R.; Kirkwood, S. E.; Fedosejevs, R.; Amirfazli, A., Direct patterning of self-assembled monolayers on gold using a laser beam. *Langmuir* **2004**, *20* (7), 2667-2676.
- (84) Liao, W. S.; Cheunkar, S.; Cao, H. H.; Bednar, H. R.; Weiss, P. S.; Andrews, A. M., Subtractive patterning via chemical lift-off lithography. *Science* **2012**, *337* (6101), 1517-1521.
- (85) Pardo, L.; Wilson, W. C.; Boland, T. J., Characterization of patterned self-assembled monolayers and protein arrays generated by the ink-jet method. *Langmuir* **2003**, *19* (5), 1462-1466.
- (86) Vickerman, J. C.; Gilmore, I., *Surface analysis : The principal techniques*. Second edition. ed.; John Wiley & Sons: Chichester, U.K., 2009; p xix, 666 pages.
- (87) Woodruff, D. P.; Delchar, T. A., *Modern techniques of surface science*. Second edition. ed.; Cambridge University Press: New York, **1994**; p xviii, 586 pages.
- (88) Woods, D. A.; Petkov, J.; Bain, C. D., Surfactant adsorption kinetics by total internal reflection raman spectroscopy. 2. Ctab and triton x-100 mixtures on silica. *J Phys Chem B* **2011**, *115* (22), 7353-7363.
- (89) Woods, D. A.; Petkov, J.; Bain, C. D., Surfactant adsorption kinetics by total internal reflection raman spectroscopy. 1. Pure surfactants on silica. *J Phys Chem B* **2011**, *115* (22), 7341-7352.
- (90) Malinowski, E. R., *Factor analysis in chemistry*. Third edition. ed.; John Wiley & Sons: New York, 2002; p xviii, 414 pages.
- (91) Fang, M.; Baldelli, S., Grain structures and boundaries on microcrystalline copper covered with an octadecanethiol monolayer revealed by sum frequency generation microscopy. *J Phys Chem Lett* **2015**, *6* (8), 1454-1460.
- (92) Han, Y.; Raghunathan, V.; Feng, R. R.; Maekawa, H.; Chung, C. Y.; Feng, Y.; Potma, E. O.; Ge, N. H., Mapping molecular orientation with phase sensitive vibrationally resonant sum-frequency generation microscopy. *J Phys Chem B* **2013**, *117* (20), 6149-6156.

- (93) Lewis, I. R.; Edwards, H. G. M., *Handbook of raman spectroscopy: From the research laboratory to the process line*. Marcel Dekker: New York, 2001; p xiii, 1054 pages.
- (94) Shen, Y. R., Surface-properties probed by 2nd-harmonic and sum-frequency generation. *Nature* **1989**, 337 (6207), 519-525.
- (95) Hoffmann, D. M. P.; Kuhnke, K.; Kern, K., Sum-frequency generation microscope for opaque and reflecting samples. *Rev Sci Instrum* **2002**, 73 (9), 3221-3226.
- (96) Shen, Y. R., Surfaces probed by nonlinear optics. *Surf Sci* **1994**, 299 (1-3), 551-562.
- (97) Su, X. C.; Cremer, P. S.; Shen, Y. R.; Somorjai, G. A., High-pressure co oxidation on pt(111) monitored with infrared-visible sum frequency generation (sfg). *J Am Chem Soc* **1997**, 119 (17), 3994-4000.
- (98) Cremer, P. S.; Su, X. C.; Shen, Y. R.; Somorjai, G. A., Ethylene hydrogenation on pt(111) monitored in situ at high pressures using sum frequency generation. *J Am Chem Soc* **1996**, 118 (12), 2942-2949.
- (99) Chen, Z.; Gracias, D. H.; Somorjai, G. A., Sum frequency generation (sfg)-surface vibrational spectroscopy studies of buried interfaces: Catalytic reaction intermediates on transition metal crystal surfaces at high reactant pressures; polymer surface structures at the solid-gas and solid-liquid interfaces. *Appl Phys B-Lasers O* **1999**, 68 (3), 549-557.
- (100) Raghunathan, V.; Han, Y.; Korth, O.; Ge, N. H.; Potma, E. O., Rapid vibrational imaging with sum frequency generation microscopy. *Opt Lett* **2011**, 36 (19), 3891-3893.
- (101) Smith, K. A.; Conboy, J. C., A simplified sum-frequency vibrational imaging setup used for imaging lipid bilayer arrays. *Anal Chem* **2012**, 84 (19), 8122-8126.
- (102) Shen, Y. R., Basic theory of surface sum-frequency generation. *J Phys Chem C* **2012**, 116 (29), 15505-15509.
- (103) Jang, J. H.; Jacob, J.; Santos, G.; Lee, T. R.; Baldelli, S., Image contrast in sum frequency generation microscopy based on monolayer order and coverage. *J Phys Chem C* **2013**, 117 (29), 15192-15202.
- (104) Santos, G.; Baldelli, S., Scale dependence of the orientation and conformation distribution analysis of a molecular mono layer using sum frequency generation imaging microscopy. *J Phys Chem C* **2012**, 116 (49), 25874-25887.
- (105) Cimatu, K.; Moore, H. J.; Lee, T. R.; Baldelli, S., Sum frequency generation imaging of microcontact-printed monolayers derived from aliphatic dithiocarboxylic acids: Contrast based on terminal-group orientation. *J Phys Chem C* **2007**, 111 (32), 11751-11755.

- (106) Rey, N. G.; Weissenborn, E.; Schulze-Zachau, F.; Gochev, G.; Braunschweig, B., Quantifying double-layer potentials at liquid gas interfaces from vibrational sum-frequency generation. *J Phys Chem C* **2019**, *123* (2), 1279-1286.
- (107) Novakovic, D.; Saarinen, J.; Rojalin, T.; Antikainen, O.; Fraser-Miller, S. J.; Laaksonen, T.; Peltonen, L.; Isomaki, A.; Strachan, C. J., Multimodal nonlinear optical imaging for sensitive detection of multiple pharmaceutical solid-state forms and surface transformations. *Anal Chem* **2017**, *89* (21), 11460-11467.
- (108) Zheng, D. S.; Lu, L. Y.; Kelly, K. F.; Baldelli, S., Chemical imaging of self-assembled monolayers on copper using compressive hyperspectral sum frequency generation microscopy. *J Phys Chem B* **2018**, *122* (2), 464-471.
- (109) Huang, S. X.; Makarem, M.; Kiemle, S. N.; Hamedi, H.; Sau, M.; Cosgrove, D. J.; Kim, S. H., Inhomogeneity of cellulose microfibril assembly in plant cell walls revealed with sum frequency generation microscopy. *J Phys Chem B* **2018**, *122* (19), 5006-5019.
- (110) Lee, C. M.; Kafle, K.; Huang, S. X.; Kim, S. H., Multimodal broadband vibrational sum frequency generation (mm-bb-v-sfg) spectrometer and microscope. *J Phys Chem B* **2016**, *120* (1), 102-116.
- (111) Nickolov, Z. S.; Britt, D. W.; Miller, J. D., Sum-frequency spectroscopy analysis of two-component langmuir monolayers and the associated interfacial water structure. *J Phys Chem B* **2006**, *110* (31), 15506-15513.
- (112) Pikalov, A. A.; Ngo, D.; Lee, H. J.; Lee, T. R.; Baldelli, S., Sum frequency generation imaging microscopy of self-assembled monolayers on metal surfaces: Factor analysis of mixed monolayers. *Anal Chem* **2019**, *91* (2), 1269-1276.
- (113) Shen, Y. R., A few selected applications of surface nonlinear optical spectroscopy. *P Natl Acad Sci USA* **1996**, *93* (22), 12104-12111.
- (114) Durig, J. R.; Yu, Z.; Guirgis, G. A., Conformational stability, barriers to internal rotation, vibrational assignment, and ab initio calculations of 2,2-difluorobutane. *J Mol Struct* **1999**, *509* (1-3), 115-135.
- (115) Durig, J. R.; Guirgis, G. A.; Li, Y. S., Microwave, raman, and far infrared-spectra, barrier to internal-rotation, and dipole-moment of 2,2-difluoropropane. *J Chem Phys* **1981**, *74* (11), 5946-5953.
- (116) McNaughton, D.; Evans, C., High-resolution ftir spectrum of jet-cooled ch<sub>3</sub>chf<sub>2</sub>. *J Phys Chem-Us* **1996**, *100* (21), 8660-8664.
- (117) Nanaie, H.; Guirgis, G. A.; Durig, J. R., Torsional spectra of molecules with 2 c-3v rotors .25. Rotational and vibrational-spectra, r(0) structure, barriers to internal-rotation and ab-

- initio calculations for 2,2-difluoropropane. *Spectrochim Acta A* **1993**, *49* (13-14), 2039-2056.
- (118) Li, Y. S.; Cox, F. O.; Durig, J. R., Low-resolution microwave, infrared, and raman-spectra, conformational stability, and vibrational assignment of 2,2,2-trifluoroethyl methyl-ether. *J Phys Chem-Us* **1987**, *91* (6), 1334-1344.
- (119) Guyot-Sionnest, P.; Hunt, J. H.; Shen, Y. R., Sum-frequency vibrational spectroscopy of a langmuir film: Study of molecular orientation of a two-dimensional system. *Phys Rev Lett* **1987**, *59* (14), 1597-1600.
- (120) Bain, C. D.; Davies, P. B.; Ward, R. N., In-situ sum-frequency spectroscopy of sodium dodecyl-sulfate and dodecanol coadsorbed at a hydrophobic surface. *Langmuir* **1994**, *10* (7), 2060-2063.
- (121) Hedberg, J.; Leygraft, C.; Cimatu, K.; Baldelli, S., Adsorption and structure of octadecanethiol on zinc surfaces as probed by sum frequency generation spectroscopy, imaging, and electrochemical techniques. *J Phys Chem C* **2007**, *111* (47), 17587-17596.
- (122) Weisshaar, D. E.; Walczak, M. M.; Porter, M. D., Electrochemically induced transformations of monolayers formed by self-assembly of mercaptoethanol at gold. *Langmuir* **1993**, *9* (1), 323-329.
- (123) Tencer, M.; Berini, P., Toposelective electrochemical desorption of thiol sams from neighboring polycrystalline gold surfaces. *Langmuir* **2008**, *24* (21), 12097-12101.
- (124) Bain, C. D.; Biebuyck, H. A.; Whitesides, G. M., Comparison of self-assembled monolayers on gold - coadsorption of thiols and disulfides. *Langmuir* **1989**, *5* (3), 723-727.
- (125) Walczak, M. M.; Alves, C. A.; Lamp, B. D.; Porter, M. D., Electrochemical and x-ray photoelectron spectroscopic evidence for differences in the binding-sites of alkanethiolate monolayers chemisorbed at gold. *J Electroanal Chem* **1995**, *396* (1-2), 103-114.
- (126) Zubragel, C.; Deuper, C.; Schneider, F.; Neumann, M.; Grunze, M.; Schertel, A.; Woll, C., The presence of 2 different sulfur species in self-assembled films of n-alkanethiols on au and ag surfaces. *Chem Phys Lett* **1995**, *238* (4-6), 308-312.
- (127) Castner, D. G.; Hinds, K.; Grainger, D. W., X-ray photoelectron spectroscopy sulfur 2p study of organic thiol and disulfide binding interactions with gold surfaces. *Langmuir* **1996**, *12* (21), 5083-5086.
- (128) Rieley, H.; Price, N. J.; Smith, T. L.; Yang, S. H., Photo-oxidation and photo-reduction in alkylthiol monolayers self-assembled on gold. *J Chem Soc Faraday T* **1996**, *92* (19), 3629-3634.

- (129) Brewer, N. J.; Janusz, S.; Critchley, K.; Evans, S. D.; Leggett, G. J., Photooxidation of self-assembled monolayers by exposure to light of wavelength 254 nm: A static sims study. *J Phys Chem B* **2005**, *109* (22), 11247-11256.
- (130) Zhou, C. Z.; Trionfi, A.; Jones, J. C.; Hsu, J. W. P.; Walker, A. V., Comparison of chemical lithography using alkanethiolate self-assembled monolayers on gaas (001) and au. *Langmuir* **2010**, *26* (6), 4523-4528.
- (131) Wolf, K. V.; Cole, D. A.; Bernasek, S. L., High-resolution tof-sims study of varying chain length self-assembled monolayer surfaces. *Anal Chem* **2002**, *74* (19), 5009-5016.
- (132) Tencer, M.; Nie, H. Y.; Berini, P., A contact angle and tof-sims study of sam-thiol interactions on polycrystalline gold. *Appl Surf Sci* **2011**, *257* (9), 4038-4043.
- (133) Tencer, M.; Nie, H. Y.; Berini, P., Formation and electrochemical desorption of self-assembled monolayers as studied by tof-sims. *Surf Interface Anal* **2011**, *43* (6), 993-997.
- (134) Dubois, L. H.; Zegarski, B. R.; Nuzzo, R. G., Molecular ordering of organosulfur compounds on au(111) and au(100) - adsorption from solution and in ultrahigh-vacuum. *J Chem Phys* **1993**, *98* (1), 678-688.
- (135) Gerlach, R.; Polanski, G.; Rubahn, H. G., Structural manipulation of ultrathin organic films on metal surfaces: The case of decane thiol/au(111). *Appl Phys a-Mater* **1997**, *65* (4-5), 375-377.
- (136) Poirier, G. E., Coverage-dependent phases and phase stability of decanethiol on au(111). *Langmuir* **1999**, *15* (4), 1167-1175.
- (137) Xu, S.; Cruchon-Dupeyrat, S. J. N.; Garno, J. C.; Liu, G. Y.; Jennings, G. K.; Yong, T. H.; Laibinis, P. E., In situ studies of thiol self-assembly on gold from solution using atomic force microscopy. *J Chem Phys* **1998**, *108* (12), 5002-5012.
- (138) Poirier, G. E.; Pylant, E. D., The self-assembly mechanism of alkanethiols on au(111). *Science* **1996**, *272* (5265), 1145-1148.
- (139) Yamada, R.; Uosaki, K., In situ scanning tunneling microscopy observation of the self-assembly process of alkanethiols on gold(111) in solution. *Langmuir* **1998**, *14* (4), 855-861.
- (140) Noh, J.; Hara, M., Final phase of alkanethiol self-assembled monolayers on au(111). *Langmuir* **2002**, *18* (6), 1953-1956.
- (141) Bryant, M. A.; Pemberton, J. E., Surface raman-scattering of self-assembled monolayers formed from 1-alkanethiols - behavior of films at au and comparison to films at ag. *J Am Chem Soc* **1991**, *113* (22), 8284-8293.

- (142) Schoenfish, M. H.; Pemberton, J. E., Air stability of alkanethiol self-assembled monolayers on silver and gold surfaces. *J Am Chem Soc* **1998**, *120* (18), 4502-4513.
- (143) Truong, K. D.; Rowntree, P. A., Formation of self-assembled butanethiol monolayers on au substrates: Spectroscopic evidence for highly ordered island formation in sub-monolayer films. *J Phys Chem-Us* **1996**, *100* (51), 19917-19926.
- (144) Porter, M. D.; Bright, T. B.; Allara, D. L.; Chidsey, C. E. D., Spontaneously organized molecular assemblies .4. Structural characterization of normal-alkyl thiol monolayers on gold by optical ellipsometry, infrared-spectroscopy, and electrochemistry. *J Am Chem Soc* **1987**, *109* (12), 3559-3568.
- (145) Hirata, N.; Suga, S.; Noguchi, Y.; Shibuta, M.; Tsunoyama, H.; Eguchi, T.; Nakajima, A., Highly ordered self-assembled monolayers of carboxy- and ester-terminated alkanethiols on au(111): Infrared absorption and hyperthermal-deposition experiments with cr(benzene)(2) ions. *J Phys Chem C* **2017**, *121* (12), 6736-6747.
- (146) Buck, M.; Grunze, M.; Eisert, F.; Fischer, J.; Trager, F., Adsorption-kinetics of n-alkyl thiols on gold studied by 2nd-harmonic generation and x-ray photoelectron-spectroscopy. *J Vac Sci Technol A* **1992**, *10* (4), 926-929.
- (147) Thom, I.; Buck, M., Electrochemical stability of self-assembled monolayers of biphenyl based thiols studied by cyclic voltammetry and second harmonic generation. *Surf Sci* **2005**, *581* (1), 33-46.
- (148) Mishina, E.; Tamura, T.; Sakaguchi, H.; Nakabayashi, S., Kinetics of adsorption and self-assembling of thiophene and dodecanethiol studied by optical second harmonic generation. *Chem Lett* **2003**, *32* (7), 652-653.
- (149) Buck, M.; Eisert, F., Thiol adsorption on gold studied by resonant 2nd-harmonic generation and phase-sensitive detection. *J Electron Spectrosc* **1993**, *64-5*, 159-166.
- (150) Eisert, F.; Dannenberger, O.; Buck, M., Molecular orientation determined by second-harmonic generation: Self-assembled monolayers. *Phys Rev B* **1998**, *58* (16), 10860-10870.
- (151) Himmelhaus, M.; Eisert, F.; Buck, M.; Grunze, M., Self-assembly of n-alkanethiol monolayers. A study by ir-visible sum frequency spectroscopy (sfg). *J Phys Chem B* **2000**, *104* (3), 576-584.
- (152) Yeganeh, M. S.; Dougal, S. M.; Polizzotti, R. S.; Rabinowitz, P., Interfacial atomic-structure of a self-assembled alkyl thiol monolayer au(111) - a sum-frequency generation study. *Phys Rev Lett* **1995**, *74* (10), 1811-1814.
- (153) Nishi, N.; Hobara, D.; Yamamoto, M.; Kakiuchi, T., Chain-length-dependent change in the structure of self-assembled monolayers of n-alkanethiols on au(111) probed by broad-

- bandwidth sum frequency generation spectroscopy. *J Chem Phys* **2003**, *118* (4), 1904-1911.
- (154) Covert, P. A.; Hore, D. K., Assessing the gold standard: The complex vibrational nonlinear susceptibility of metals. *J Phys Chem C* **2015**, *119* (1), 271-276.
- (155) Graham, D. J.; Price, D. D.; Ratner, B. D., Solution assembled and microcontact printed monolayers of dodecanethiol on gold: A multivariate exploration of chemistry and contamination. *Langmuir* **2002**, *18* (5), 1518-1527.
- (156) Losic, D.; Shapter, J. G.; Gooding, J. J., Concentration dependence in microcontact printing of self-assembled monolayers (sams) of alkanethiols. *Electrochem Commun* **2001**, *3* (12), 722-726.
- (157) Losic, D.; Shapter, J. G.; Gooding, J. J., Influence of surface topography on alkanethiol sams assembled from solution and by microcontact printing. *Langmuir* **2001**, *17* (11), 3307-3316.
- (158) Eberhardt, A. S.; Nyquist, R. M.; Parikh, A. N.; Zawodzinski, T.; Swanson, B. I., Defects in microcontact-printed and solution-grown self-assembled monolayers. *Langmuir* **1999**, *15* (5), 1595-1598.
- (159) Bain, C. D.; Troughton, E. B.; Tao, Y. T.; Evall, J.; Whitesides, G. M.; Nuzzo, R. G., Formation of monolayer films by the spontaneous assembly of organic thiols from solution onto gold. *J Am Chem Soc* **1989**, *111* (1), 321-335.
- (160) Hahner, G.; Woll, C.; Buck, M.; Grunze, M., Investigation of intermediate steps in the self-assembly of n-alkanethiols on gold surfaces by soft-x-ray spectroscopy. *Langmuir* **1993**, *9* (8), 1955-1958.
- (161) Ulman, A., Formation and structure of self-assembled monolayers. *Chem Rev* **1996**, *96* (4), 1533-1554.
- (162) Buck, M.; Eisert, F.; Fischer, J.; Grunze, M.; Trager, F., Investigation of self-organizing thiol films by optical 2nd-harmonic generation and x-ray photoelectron-spectroscopy. *Appl Phys a-Mater* **1991**, *53* (6), 552-556.
- (163) Kim, Y. T.; Mccarley, R. L.; Bard, A. J., Observation of n-octadecanethiol multilayer formation from solution onto gold. *Langmuir* **1993**, *9* (8), 1941-1944.
- (164) Peterlinz, K. A.; Georgiadis, R., In situ kinetics of self-assembly by surface plasmon resonance spectroscopy. *Langmuir* **1996**, *12* (20), 4731-4740.
- (165) DeBono, R. F.; Loucks, G. D.; DellaManna, D.; Krull, U. J., Self-assembly of short and long-chain n-alkyl thiols onto gold surfaces: A real-time study using surface plasmon resonance techniques. *Can J Chem* **1996**, *74* (5), 677-688.

- (166) Sasic, S., Quantitative analysis of overlapped raman spectra by target factor analysis and evolving factor analysis. *Analyst* **1998**, *123* (6), 1193-1197.
- (167) Shao, L. M.; Griffiths, P. R., Obtaining qualitative information on trace species in continuous open-path fourier transform spectroscopic measurements using target factor analysis and related techniques. *Anal Chem* **2007**, *79* (5), 2118-2124.
- (168) Tam, K. Y.; Chau, F. T., Multivariate study of kinetic data for a 2-step consecutive reaction using target factor-analysis. *Chemometr Intell Lab* **1994**, *25* (1), 25-42.
- (169) Gemperline, P. J., Target transformation factor-analysis with linear inequality constraints applied to spectroscopic chromatographic data. *Anal Chem* **1986**, *58* (13), 2656-2663.
- (170) Bass, R. B.; Lichtenberger, A. W., Microcontact printing with octadecanethiol. *Appl Surf Sci* **2004**, *226* (4), 335-340.
- (171) Balmer, T. E.; Schmid, H.; Stutz, R.; Delamarche, E.; Michel, B.; Spencer, N. D.; Wolf, H., Diffusion of alkanethiols in pdms and its implications on microcontact printing (mu cp). *Langmuir* **2005**, *21* (2), 622-632.

## **APPENDIX A**

## A.1. Principle factor analysis (pfa) code

The significant factor analysis code presented here is a modified version of the code presented by Malinowski, E. R. in Factor Analysis in Chemistry, 3rd ed.; John Wiley & Sons: New York, 2002.

```
function [] = pfa(d,n)
% pfa.m Principle Factor Analysis - a program designed to help determine
% the number of significant factors in a data matrix.
% pfa(d) or pfa(d,n)
% d = data matrix
% n = number of principal factors to be saved in file temp.mat
format short e
[r,c] = size(d);
if r < c,
    d = d';
    [r,c]= size(d);
end
[u,s,v] = svd(d,0);
for j = 1:c
    ev(j) = s(j,j) * s(j,j);
    df(j) = (r-j+1)*(c-j+1);
    rev(j) = ev(j) / df(j);
end
for k = 1:c-1
    sev(k) = sum(ev(k+1:c));
    sdf(k) = sum(df(k+1:c));
end
for i = 1:c-1
    re(i) =sqrt(sev(i) / (r * (c-i)));
    ind(i) = re(i) / (c-i)^2;
end
[vind,m] = min(ind);
disp(['IND function indicates ',int2str(m),' significant factors (see eq. 4.63).'])
disp(['The real error (RE) is +/-',num2str(re(m)),' (see eq. 4.44).'])
re(c) = NaN; ind(c) = NaN;
for j = 1:c
    t(j,1) = j;
    t(j,2) = ev(j);
    t(j,3) = re(j);
    t(j,4) = ind(j);
    t(j,5) = rev(j);
end
for j = 1:c-1
    f = (sdf(j) * ev(j)) / ((r-j+1) * (c-j+1) * sev(j));
% convert f (see eq. 4.83) into percent significant level
```

```

    if j < c
        tt = sqrt(f);
        df = c - j;
        a = tt / sqrt(df);
        b = df / (df + tt * tt);
        im = df - 2;
        jm = df - 2 * fix(df / 2);
        ss = 1;
        cc = 1;
        ks = 2 + jm;
        fk = ks;
        if (im - 2) >= 0
            for k = ks:2:im
                cc = cc * b * (fk - 1) / fk;
                ss = ss + cc;
                fk = fk + 2;
            end
        end
        if (df - 1) > 0
            cl = .5 + (a * b * ss + atan(a)) * .31831;
        else
            cl = .5 + atan(a) * .31831;
        end
        if jm <= 0
            cl = .5 + .5 * a * sqrt(b) * ss;
        end
    end
    sl = 100 * (1 - cl);
    sl = 2 * sl;
    t(j,6) = sl;
end
t(c,6) = NaN;
disp(['PFA RESULTS (note %SL based on eq. 4.83)'])
disp(' ')
disp('  n      EV      RE      IND      REV      %SL')
disp(t)
if n > 0
    u = u(:,1:n);
    s = s(1:n,1:n);
    v = v(:,1:n);
    save temp u s v
    disp(' ')
    disp('The SVD results are stored in a file labelled "temp.mat":')
    disp(' ')
    disp('To access the file, type "load temp".')
end

```

## A.2. Target factor analysis (tfa) code

The target factor analysis code presented here is a modified version of the code presented by Malinowski, E. R. in Factor Analysis in Chemistry, 3rd ed.; John Wiley & Sons: New York, 2002.

```
function [] = tfa(d,x,n)
% tfa.m Target factor analysis - a program designed to
% target test suspected vectors.
% tfa(d,x,n)
% d = an (r x c) data matrix.
% x = an (r x m) matrix composed of m test vectors, each with r elements.
% n = number of factors to be used in the target tests.
% No provision is made for handling missing points (blanks) in the targets.

format short e
[rx,nx] = size(x);
[r,c] = size(d);
if rx ~= r
disp('Target vectors must emulate columns of the data matrix! Program Aborted')
end

lg = r;
sm = c;
if r < c
lg = c;
sm = r;
[v,s,u] = svd(d',0);
else
[u,s,v] = svd(d,0);
end
for j=1:sm
ev(j) = s(j,j) * s(j,j);
df(j) = (r-j+1)*(c-j+1);
rev(j) = ev(j) / df(j);
u(:,j) = u(:,j) * s(j,j);
end
ubar = u(:,1:n);
sev = sum(ev(n+1:sm));
sdf = sum(df(n+1:sm));
re = sqrt(sev / (lg * (sm-n)));
for j = 1:nx
t(:,j) = pinv(ubar) * x(:,j);
xp(:,j) = ubar * t(:,j);
dx = xp(:,j) - x(:,j);
aet(j) = sqrt((dx' * dx) / (rx - n));
rep(j) = re * norm(t(:,j));
```

```

                if rep(j) > aet(j)
                    ret(j) = 0;
                else
                    ret(j) = sqrt(aet(j)^2 - rep(j)^2);
                end
            spoil(j) = ret(j) / rep(j);
            f(j) = (sdf * r * aet(j)^2) / ((r-n+1) * (c-n+1) * sev * t(:,j)' * t(:,j));
        end

df1 = rx - n;
df2 = sm - n;
disp(' ')
disp('RESULTS OF TARGET TESTING (see Section 4.6)')
disp(' ')
        for j = 1:nx
            tx(j,1) = j;
            tx(j,2) = aet(j);
            tx(j,3) = rep(j);
            tx(j,4) = ret(j);
            tx(j,5) = spoil(j);
            tx(j,6) = f(j);
        end
disp(' target #    AET    REP    RET    SPOIL    F')
disp(tx)
predv = xp(:,1:nx);
save temp predv
disp(' ')
disp('The predicted vectors have been stored in a file labelled "temp.mat"')
disp(' ')
disp('To access this file, type "load temp".')
disp(' ')

```

### A.3. Loading factor analysis (lfa) code

The loading factor analysis code presented here is a modified version of the code presented by Malinowski, E. R. in Factor Analysis in Chemistry, 3rd ed.; John Wiley & Sons: New York, 2002.

```
function [] = lfa(d,x,n)
% lfa.m - Loading Factor Analysis - a program designed to calculate
%         factor loadings and errors in the loadings.
% lfa(d,x,n)
% d = an (r x c) data matrix.
% x = an (r x m) matrix composed of m test vectors.
% n = number of factors to be used in the target tests.
% The factor space is assumed to be n dimensional.
% No provision is made for handling missing points (blanks) in the targets.
format short e
[rx,nx] = size(x);
[r,c] = size(d);
if rx ~= r
disp('Target vectors must emulate columns of the data matrix! PROGRAM ABORTED')
end

    sm = c;
    if r < c
        sm = r;
        [v,s,u] = svd(d',0);
    else
        [u,s,v] = svd(d,0);
    end
    for j = 1:sm
        u(:,j) = u(:,j) * s(j,j);
    end
ubar = u(:,1:n);
vbar = v(:,1:n);
    for j = 1:nx
        t(:,j) = pinv(ubar) * x(:,j);
        xp(:,j) = ubar * t(:,j);
        dx = xp(:,j) - x(:,j);
    end
loadings = pinv(t) * vbar';

% Estimate the error in the loadings (Clifford method)
e = d - x * loadings;
xx = inv(x' * x);
    for j = 1:c
        v = xx * (e(:,j)' * e(:,j)) / (rx - n);
        for k = 1:nx
```

```
                                loaderr(k,j) = sqrt(v(k,k));
                                end
                                end
loadings = loadings';
loaderr = loaderr';
save temp loadings loaderr
disp(' ')
disp('The results have been stored in file labelled "temp.mat" as follows:')
disp(' ')
disp('To access the file, type "load temp".')
disp(' ')
```

## A.4. Other MATLAB codes

### A.4.1. Remove first line of .txt

```
Folder = 'C:/Users/user_name/Desktop/folder_name/';
fileName = 'file_name';
format = '.txt';

a1 = 0;
for k = 1:102;
    b1 = num2str(a1);
    fileName1 = [fileName b1];
    dash = '-';
    fileName2 = [fileName1 dash];
    g = 0;
    for k = 1:102;
        b2 = num2str(g);
        fileName3 = [fileName2 b2];
        openName = [Folder fileName3 format];
        fid = fopen(openName,'r');
        fgetl(fid);
        buffer = fread(fid, Inf);
        fclose(fid);
        saveName = [Folder fileName3 format];
        fid2 = fopen(saveName,'w');
        fwrite(fid, buffer);
        fclose(fid2);
        g = g + 10;
    end
    a1 = a1 + 10;
end
```

#### A.4.2. Data matrix

```
openFolder = 'C:/Users/user_name/Desktop/folder_name/';
fileName = 'file_name';
format = '.txt';
C = [];

a1 = 0;
for k = 1:102;
    b1 = num2str(a1);
    fileName1 = [fileName b1];
    dash = '-';
    fileName2 = [fileName1 dash];
    g = 0;
    for k = 1:102;
        b2 = num2str(g);
        fileName3 = [fileName2 b2];
        openName = [openFolder fileName3 format];
        fid = fopen(openName,'r');
        sizeA = [2 Inf];
        formatSpec = '%g %g';
        A = fscanf(fid, formatSpec, sizeA);
        fclose(fid);
        B = A';
        C = [C B(:,end)];
        g = g + 10;
    end
    a1 = a1 + 10;
end
C;
fid2 = 'file_name.mat';
save(fid2);
```

### A.4.3. Target test matrix

`% target test 1`

```
fileID = fopen('C:/Users/user_name/Desktop/folder_name/file_name.txt','r');
sizeA = [2 Inf];
formatSpec = '%g %g';
A = fscanf(fileID, formatSpec, sizeA);
fclose(fileID);
B = A';
```

```
C = B(:,end);
```

`% target test 2`

```
fileID = fopen('C:/Users/ user_name/Desktop/folder_name/file_name.txt','r');
sizeA = [2 Inf];
formatSpec = '%g %g';
A = fscanf(fileID, formatSpec, sizeA);
fclose(fileID);
B = A';
```

```
C = [C B(:,end)];
```

`% target test 3`

```
fileID = fopen('C:/Users/ user_name/Desktop/folder_name/file_name.txt','r');
sizeA = [2 Inf];
formatSpec = '%g %g';
A = fscanf(fileID, formatSpec, sizeA);
fclose(fileID);
B = A';
```

```
C = [C B(:,end)];
```

```
fid = "file_name.mat";
save(fid);
```

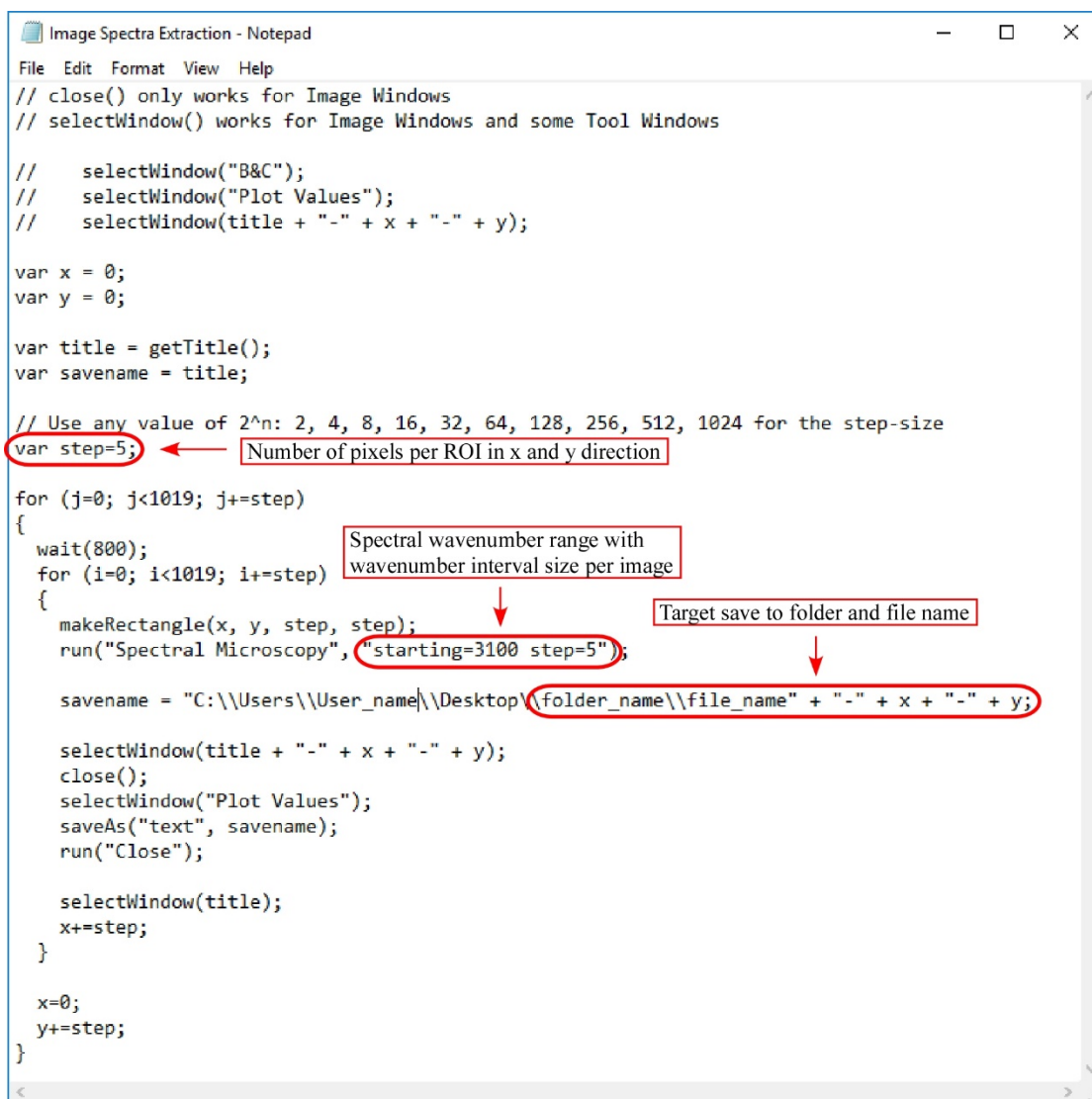
## A.5. Data analysis

Step-by-step outline for producing target transformed chemical maps on MATLAB.

### A.5.1. Spectra extraction from SFG images for data matrix and test target matrix

#### a) Spectra extraction using ImageJ mapping for data matrix

- 1) In the notepad, containing the image spectra extraction code, shown in Figure A-1, specify the required region of interest (ROI) size, spectral range, and target save to folder with file name. Save the changes made to the .txt file.



```
Image Spectra Extraction - Notepad
File Edit Format View Help
// close() only works for Image Windows
// selectWindow() works for Image Windows and some Tool Windows

//  selectWindow("B&C");
//  selectWindow("Plot Values");
//  selectWindow(title + "-" + x + "-" + y);

var x = 0;
var y = 0;

var title = getTitle();
var savename = title;

// Use any value of 2^n: 2, 4, 8, 16, 32, 64, 128, 256, 512, 1024 for the step-size
var step=5; ← Number of pixels per ROI in x and y direction

for (j=0; j<1019; j+=step)
{
    wait(800);
    for (i=0; i<1019; i+=step)
    {
        makeRectangle(x, y, step, step);
        run("Spectral Microscopy", "starting=3100 step=5");
        savename = "C:\\Users\\User_name\\Desktop\\folder_name\\file_name" + "-" + x + "-" + y;

        selectWindow(title + "-" + x + "-" + y);
        close();
        selectWindow("Plot Values");
        saveAs("text", savename);
        run("Close");

        selectWindow(title);
        x+=step;
    }

    x=0;
    y+=step;
}
}
```

Figure A-1. Image Spectra Extraction code used for spectral extraction from ROIs.

- 2) Open the acquired SFG image stack in ImageJ mapping program.
- 3) Reverse the image stack using the Stack Reverser under Plugins Menu, Figure A-2.
- 4) From the Plugins Menu, select the Macros tab, then select Run. In the file explorer, select and open the file containing the image spectra extraction code. (see Figure A-3)

Note: The program requires some time to complete the spectral extraction operation. The spectra extracted from each ROI is automatically saved as a .txt file in the folder specified in the image spectral extraction code.

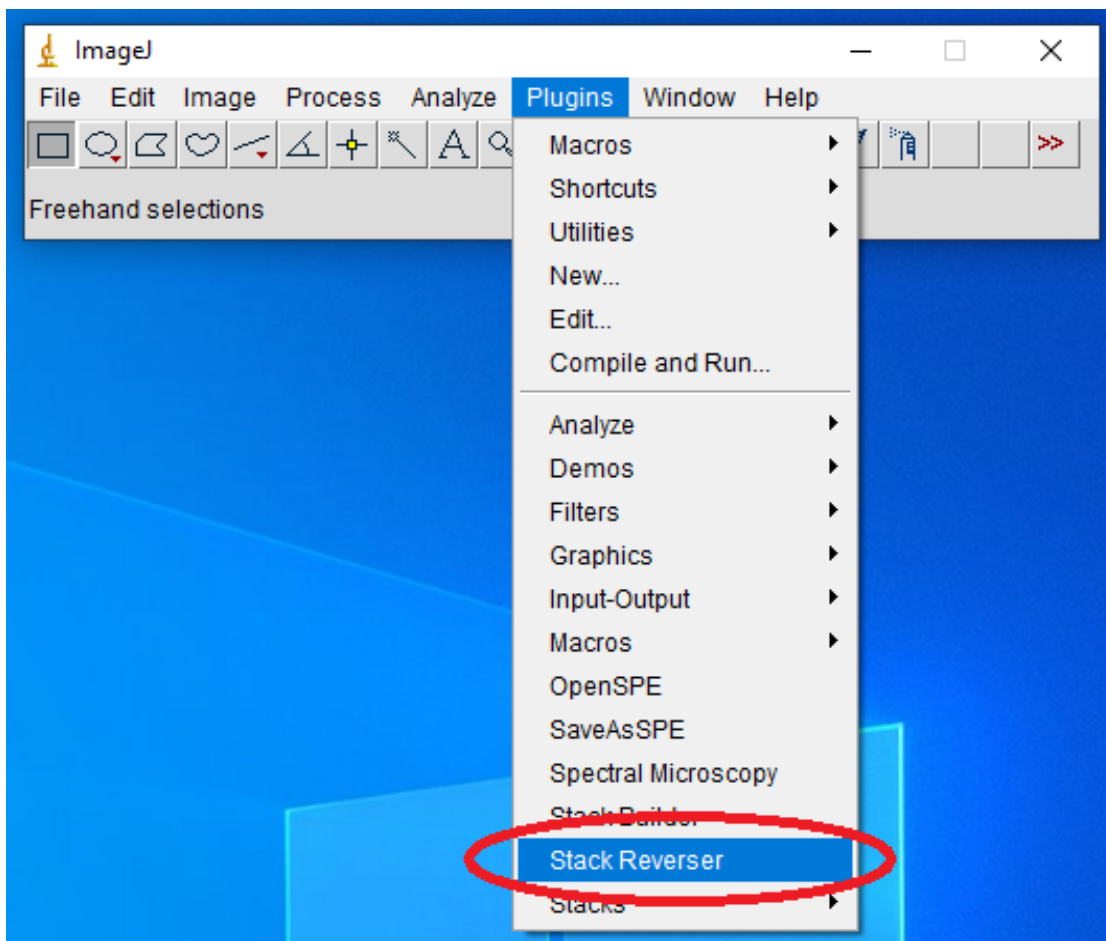


**Figure A-2.** ImageJ Stack Reverser Plugin used for image stack reversing.

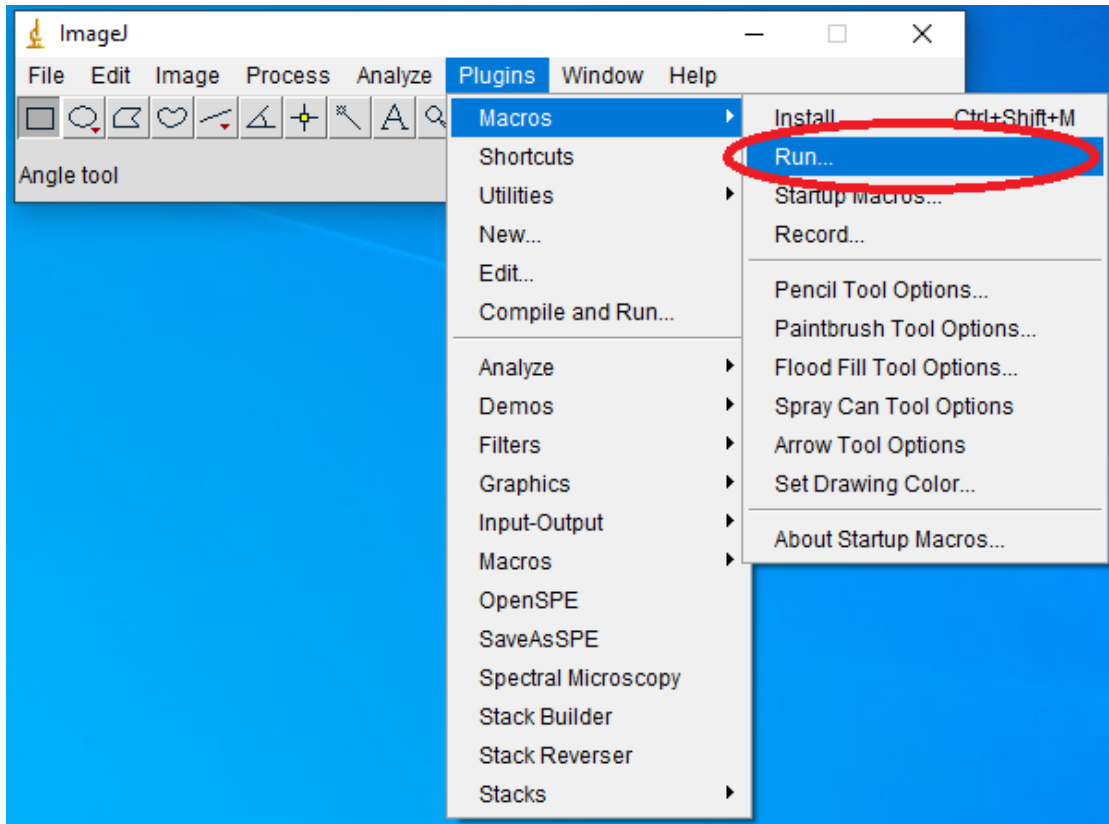


**Figure A-3.** ImageJ image spectra extraction code was ran using Macros Run Plugin.

**b) Spectra extraction using ImageJ for target test matrix**

- 1) Open the SFG images for target testing in ImageJ program.
- 2) Reverse the image stack using the Stack Reverser plugin found under the Plugins Menu.
- 3) Select the Spectral Microscopy function under the Plugins Menu, as shown in Figure A-4a. In the first dialog box, specify the ending wavenumber of the image stack as Starting Energy (Figure A-4b), and in the second box, specify the image wavenumber Step Size (Figure A-4c).
- 4) From the B&C box, shown in Figure A-4d, adjust the brightness/contrast of the image.

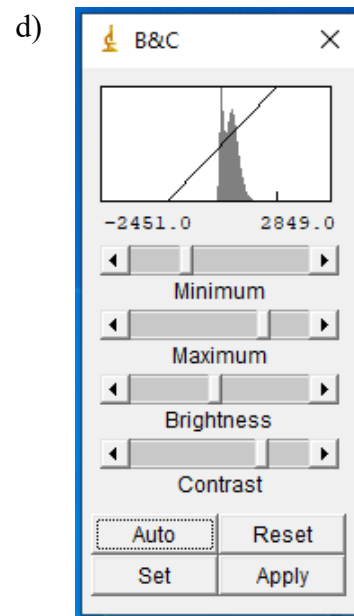
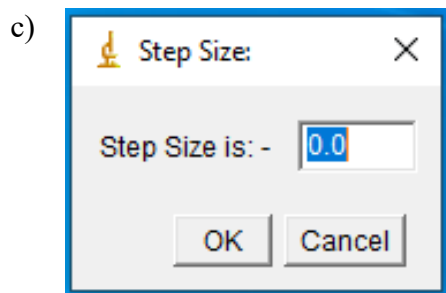
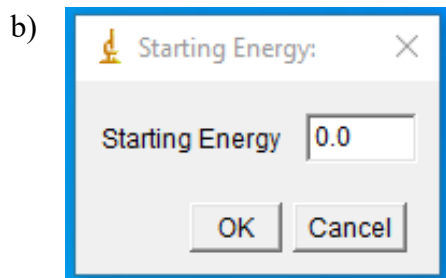
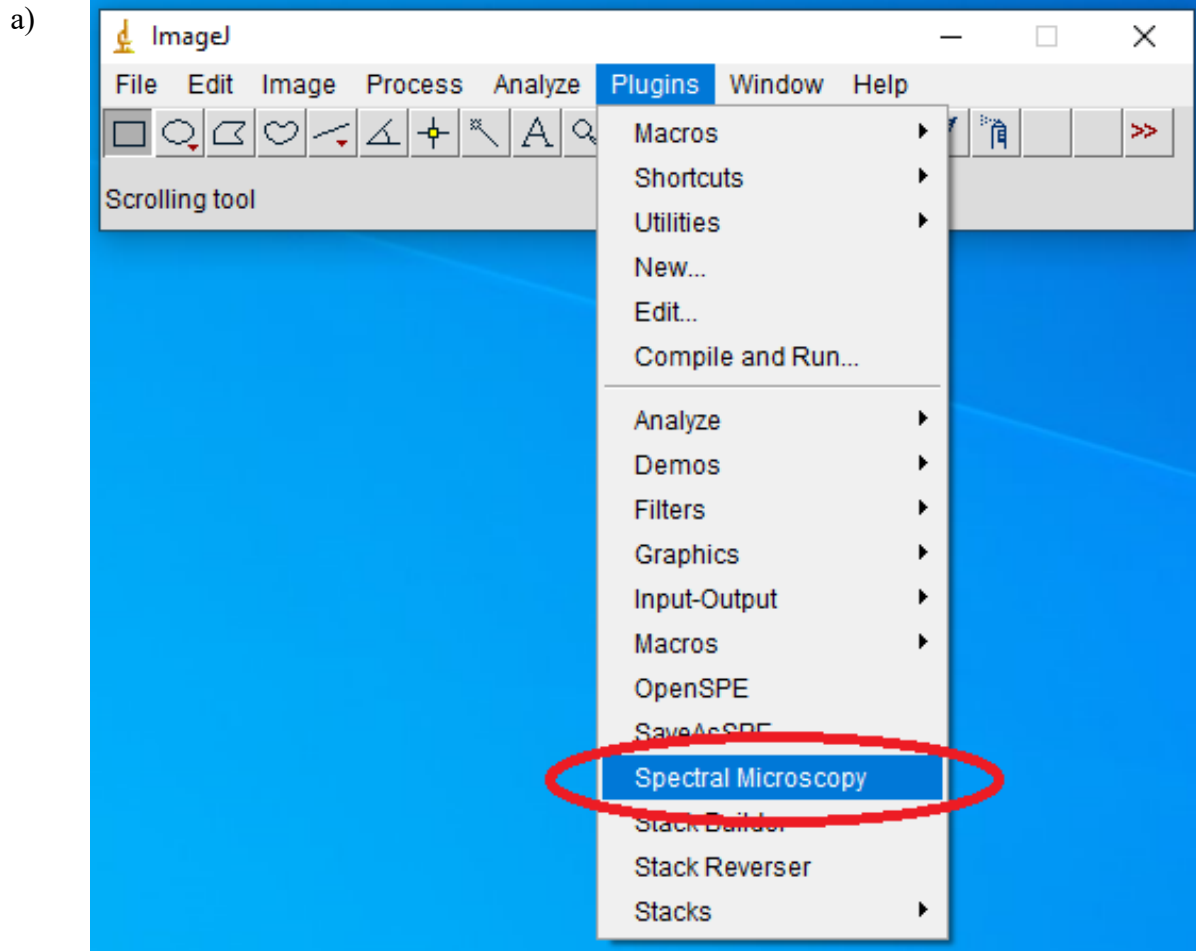


**Figure A-4.** ImageJ (a) Spectral Microscopy Plugin, (b) starting energy, (c) step size selection, and (d) brightness and contrast (B&C) adjustment.

- 5) Select an ROI of interest from the image by drawing a box with the Selection Tool as shown in Figure A-5.
- 6) Extract the spectra from the selected ROI by selecting Gen Spectrum from the Spectrum\_Extractor box, shown in Figure A-6a.

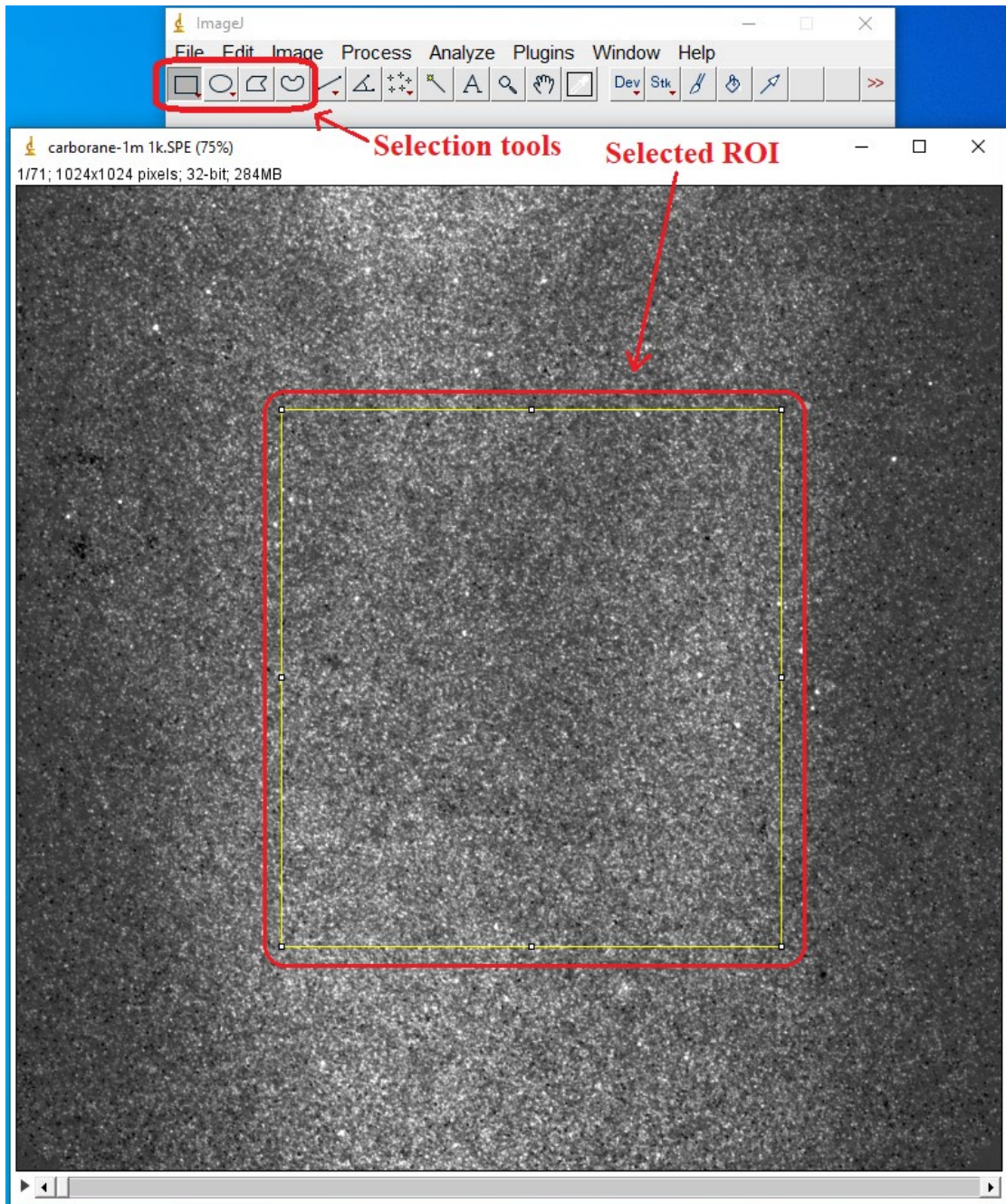


**Figure A-5.** Region of interest (ROI) was selected using selection tools.

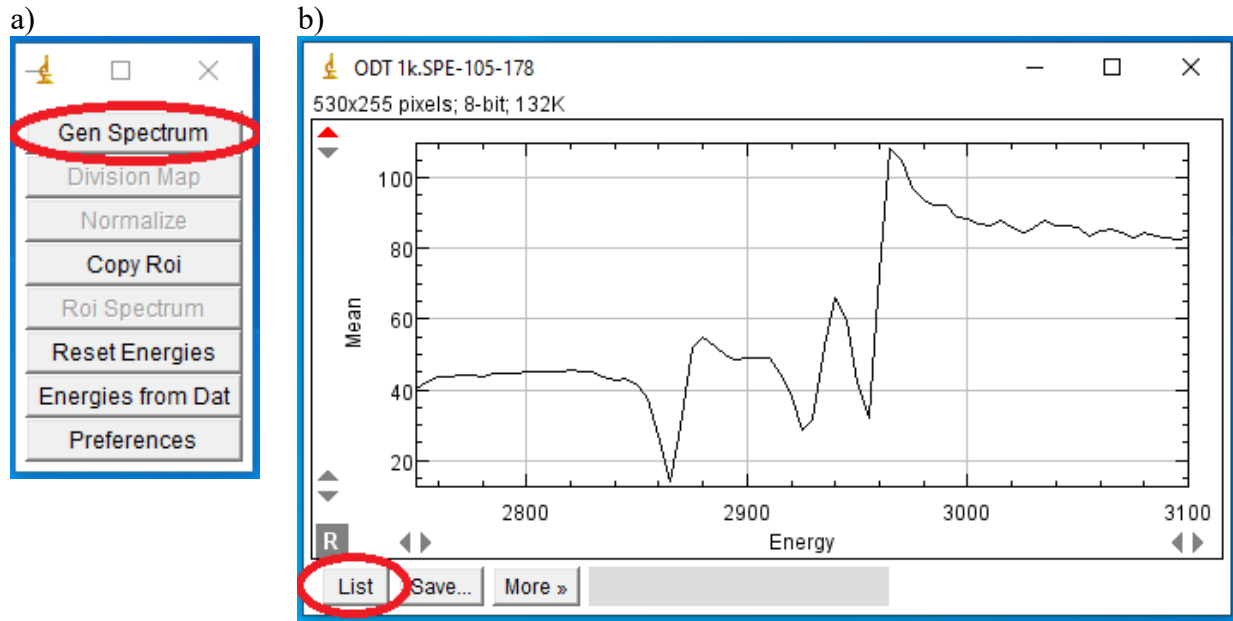


**Figure A-6.** ImageJ (a) spectra extraction using Gen Spectrum function and (b) obtaining a list of wavenumber–intensity values.

- 7) From the extracted spectrum plot box, select the List icon, shown in Figure A6b. Save the listed vales in the Plot Values box as a text file.

#### A.5.2. Data matrix and target test matrix construction in MATLAB

##### a) Data matrix construction

- 1) Once the image spectral extraction is complete, construct the data matrix by running the `data_matrix.m` code (Figure A-7).

Note: `data_matrix.m` will not import data if the `.txt` file contains any letter, except numerical values.

- 2) (Optional, if needed) The first row of the `.txt` file containing letters can be removed using the `remove_row_txt.m` code.
- 3) Open the code in MATLAB Editor. Specify the folder and file name containing the extracted spectra text files as the 'openFolder' and 'fileName', respectively.
- 3) Once the data matrix construction is completed, save the file containing the data matrix.

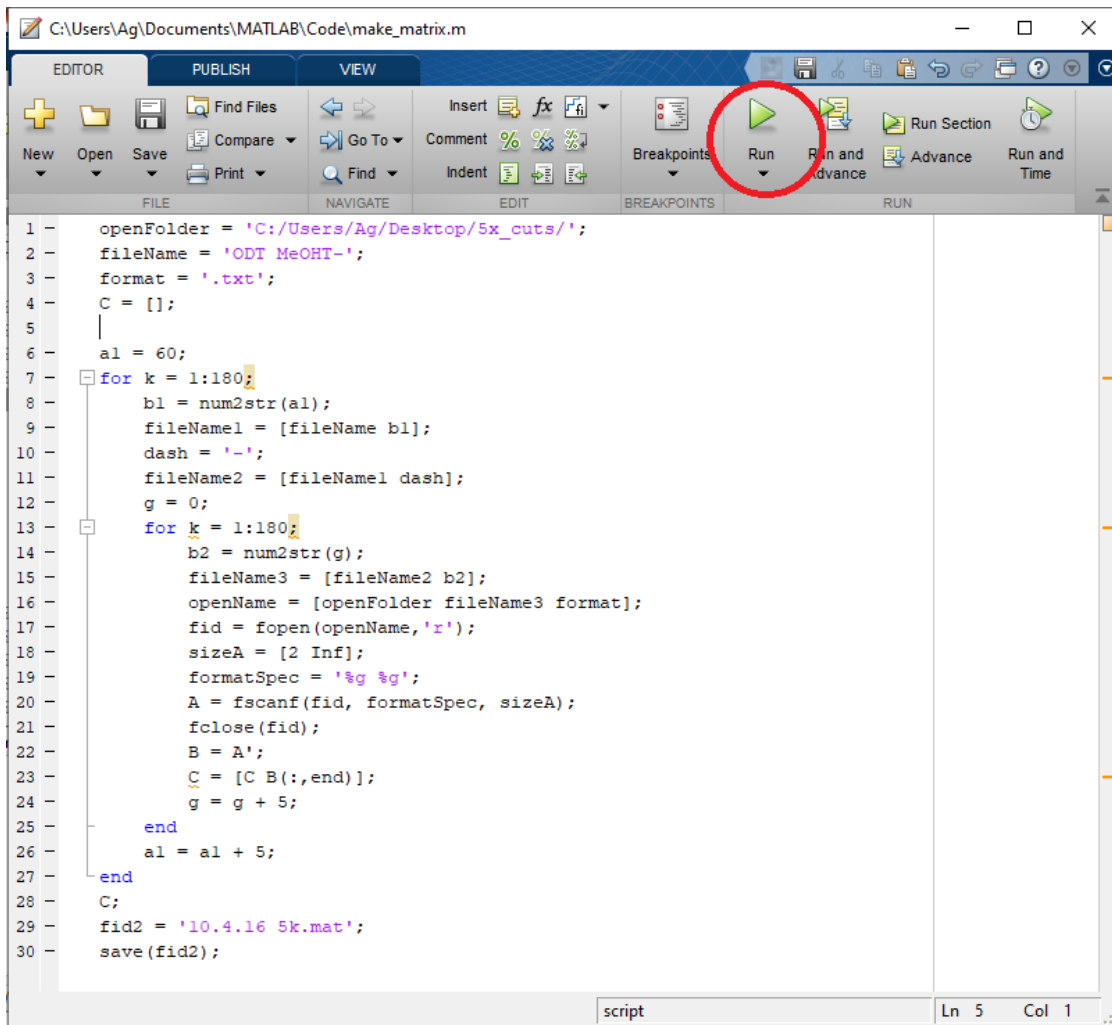


**Figure A-7.** Matrix construction using MATLAB EDITOR.

**b) Target test matrix construction**

- 1) Construct the target test matrix using target\_test\_matrix.m code.

Note: target\_test\_matrix.m will not import data if the .txt file contains any letter, except numerical values.

- 2) Once the target test matrix construction is completed, save the file containing the matrix.

### A.5.3. Data matrix analysis by significant factor analysis (sfa)

- 1) Make sure the folder containing the factor analysis (FA) code is in the directory path.  
(Figure A-8)
- 2) Add the data matrix to the Workspace of MATLAB.
- 3) Run the sfa.m code on data matrix to determine the number of significant factors. (Figure A-9)

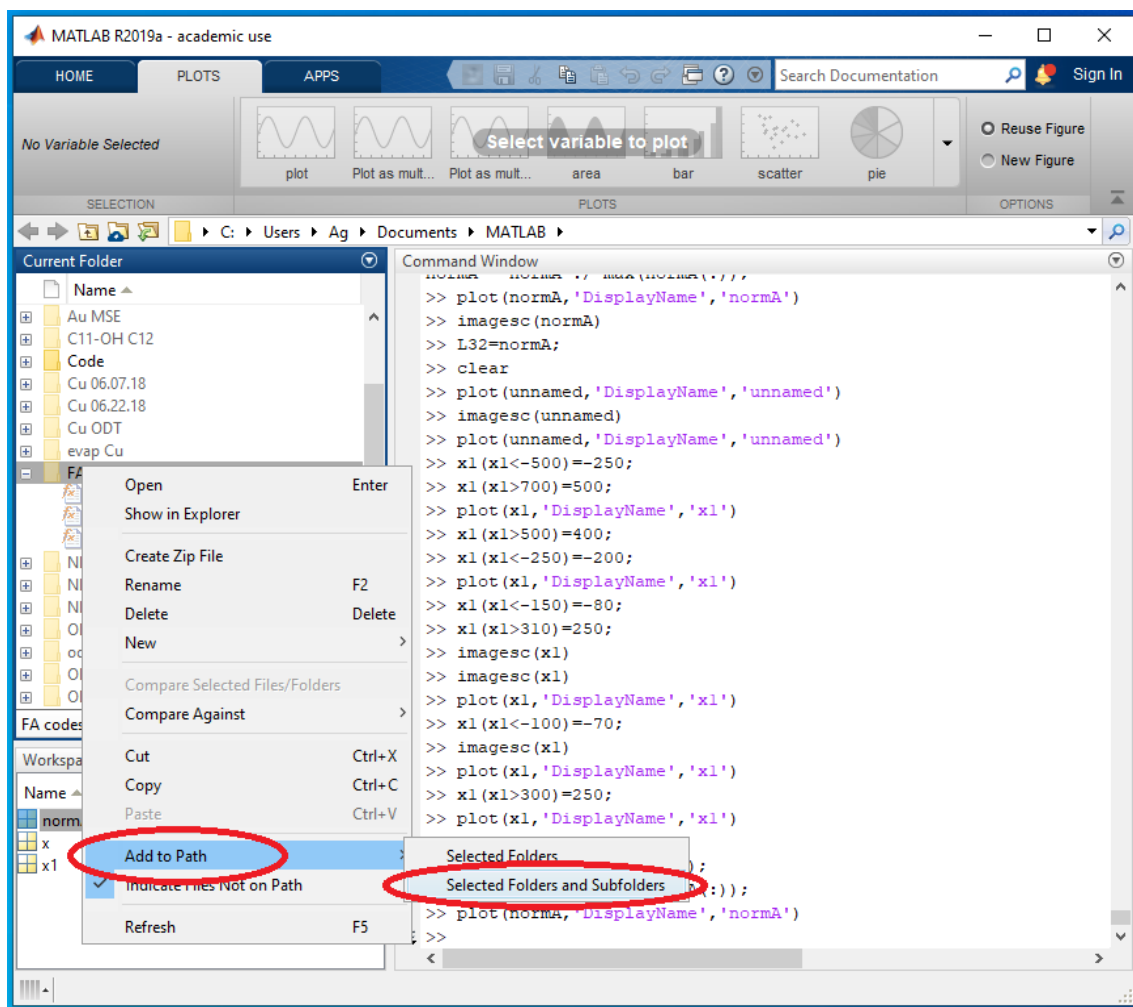


Figure A-8. Adding the factor analysis code to Path in MATLAB.

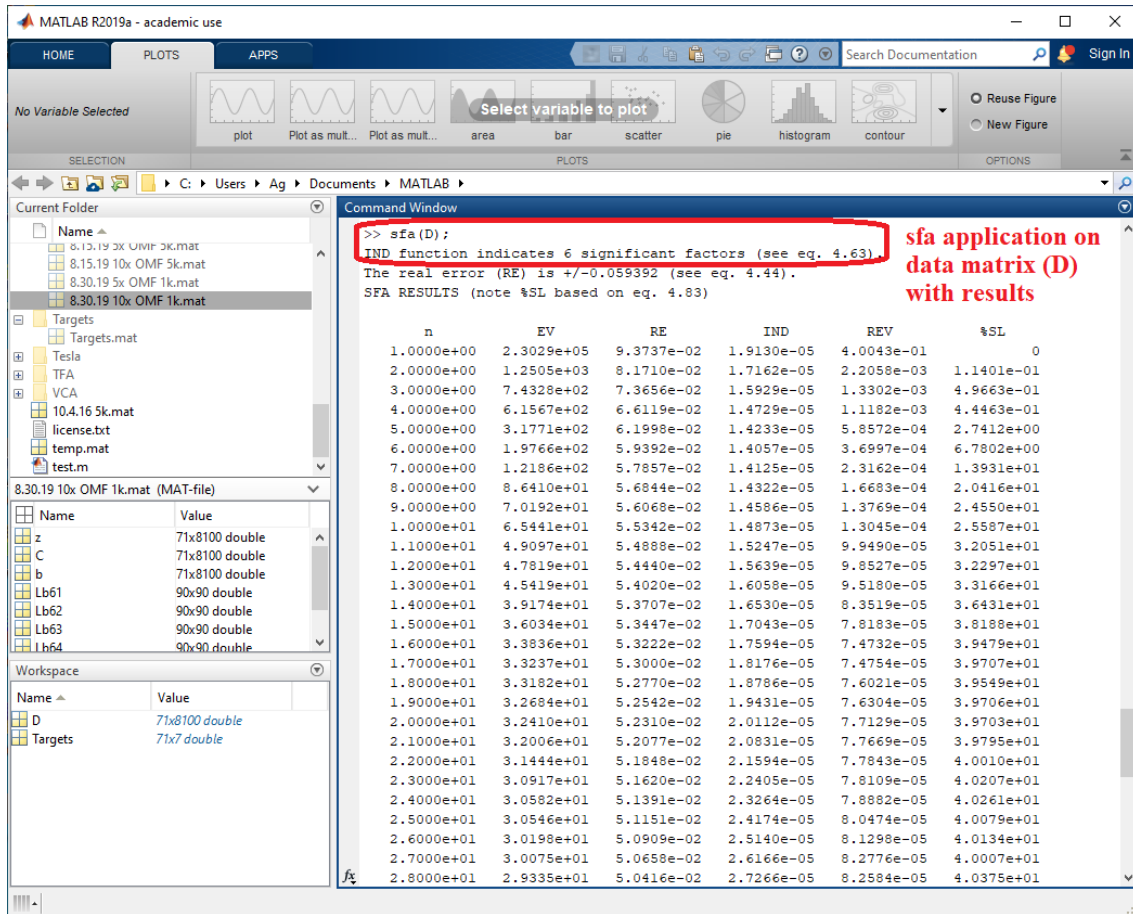


Figure A-9. Application of sfa on data matrix.

#### A.5.4. Generation of abstract factors from data matrix

- 1) To generate the abstract cofactors, run singular value decomposition as `'[u,s,v]=svd(d);'`, as shown in Figure A-10.
- 2) To visualize the abstract factors' spectra, open the 'u' worksheet, select the desired abstract factor, then plot the factor by selecting one of the built-in plot functions. (Figure A-11)
- 3) To visualize the abstract factors' spatial distribution, first, open the 'v' worksheet, select the desired abstract factor, and then, select 'create new variable from selection', as shown in Figure A-12.

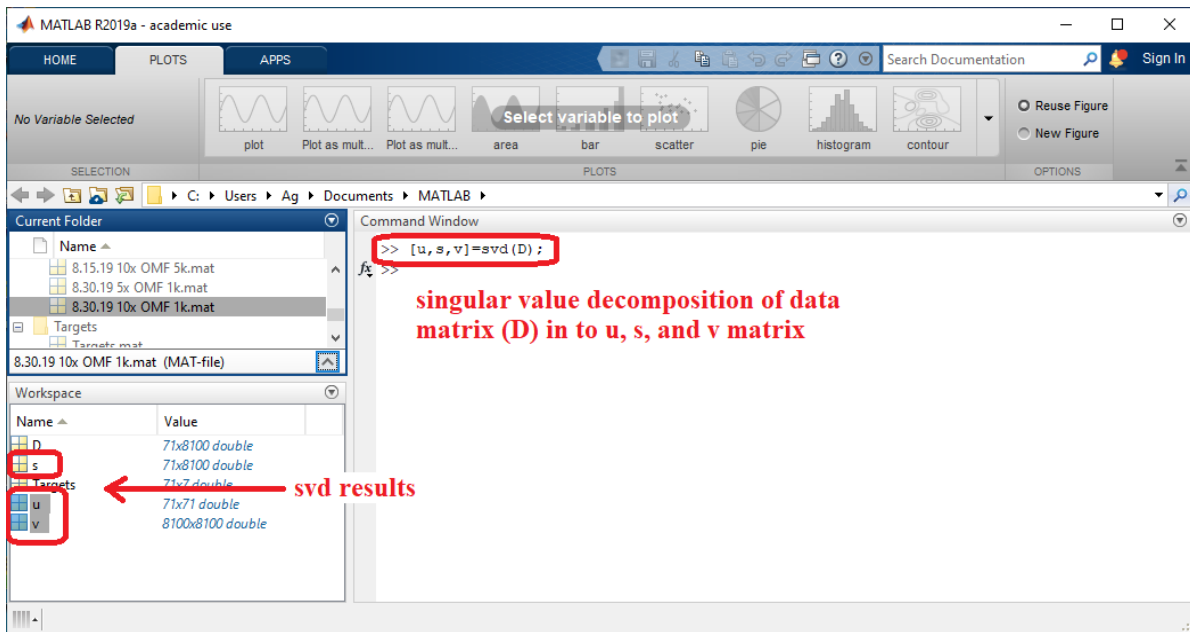


Figure A-10. Application of singular value decomposition to obtain abstract factors of data matrix.

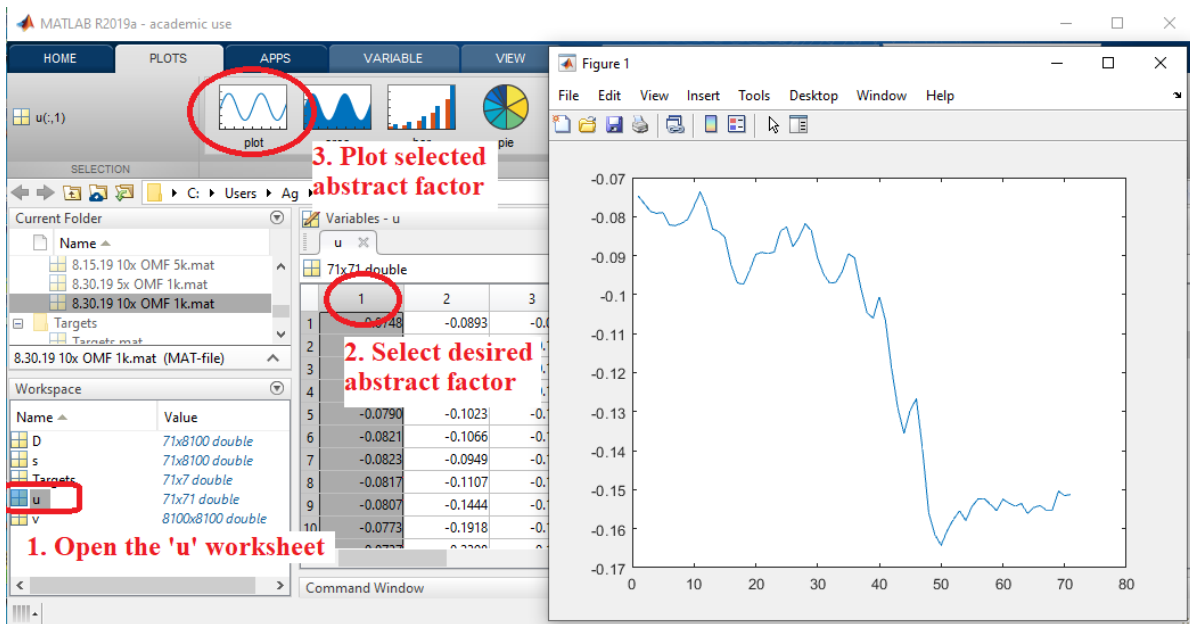


Figure A-11. Steps to visualize the decomposed abstract factors of 'u' matrix.

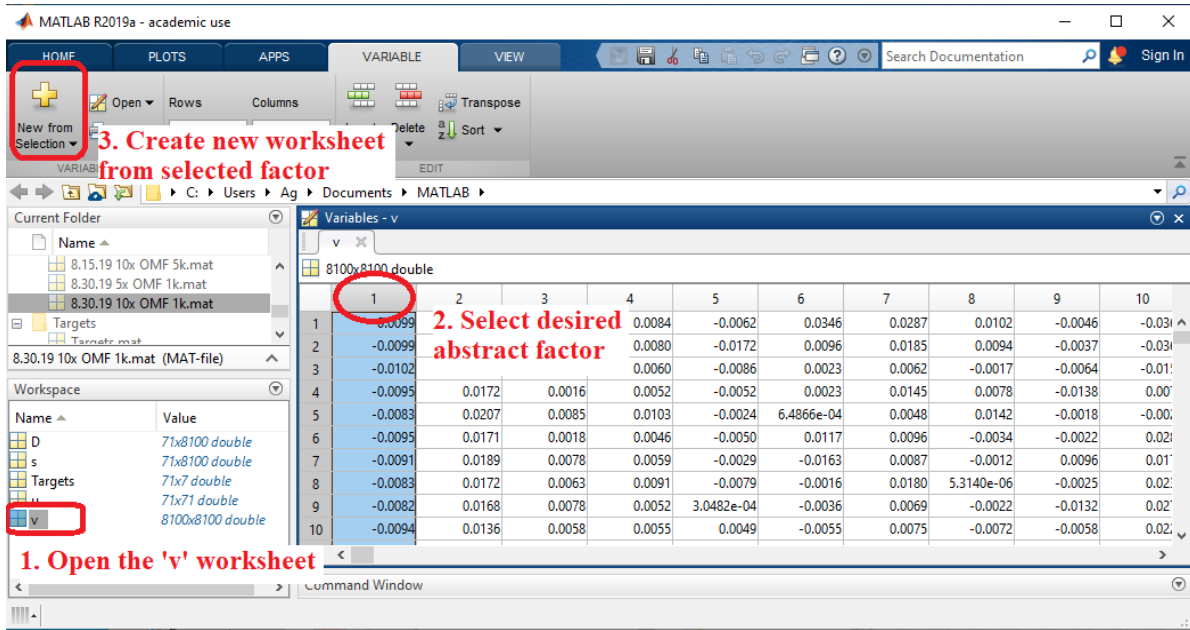


Figure A-12. Steps to select abstract factors from 'v' matrix.

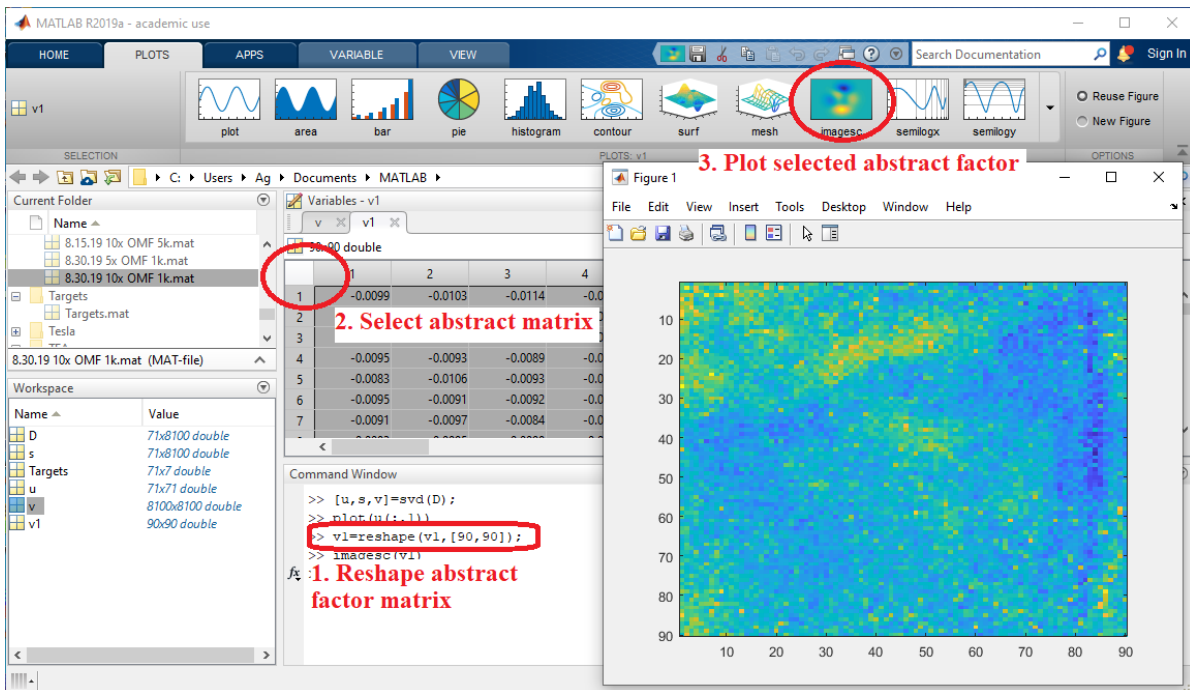


Figure A-13. Reconstruction of abstract factor to generate distribution map.

- 4) Reshape the new abstract factor matrix using 'reshape' function, select the reshaped matrix, and then, plot the abstract factor's distribution, as shown in Figure A-13.

#### A.5.5. Data matrix analysis by target factor analysis (tfa)

- 1) Run the tfa.m code. The inputs of the tfa(d,x,n) are the data matrix (d), target matrix (x), and the number of significant factors (n), as shown in Figure A-14.
- 2) Type 'load temp' to add the tfa predicted spectra to the Workspace. The predicted tfa spectra is contained in the 'predv' file.
- 3) To visualize the tfa predicted spectra, open the 'predv' worksheet, select the desired component, and then plot it. (Figure A-15)

#### A.5.6. Chemical image construction by loadings factor analysis (lfa)

- 1) To obtain chemical maps of the predicted components, run the lfa.m code. The inputs are the data matrix, target matrix, and the number of significant factors. (Figure A-16)

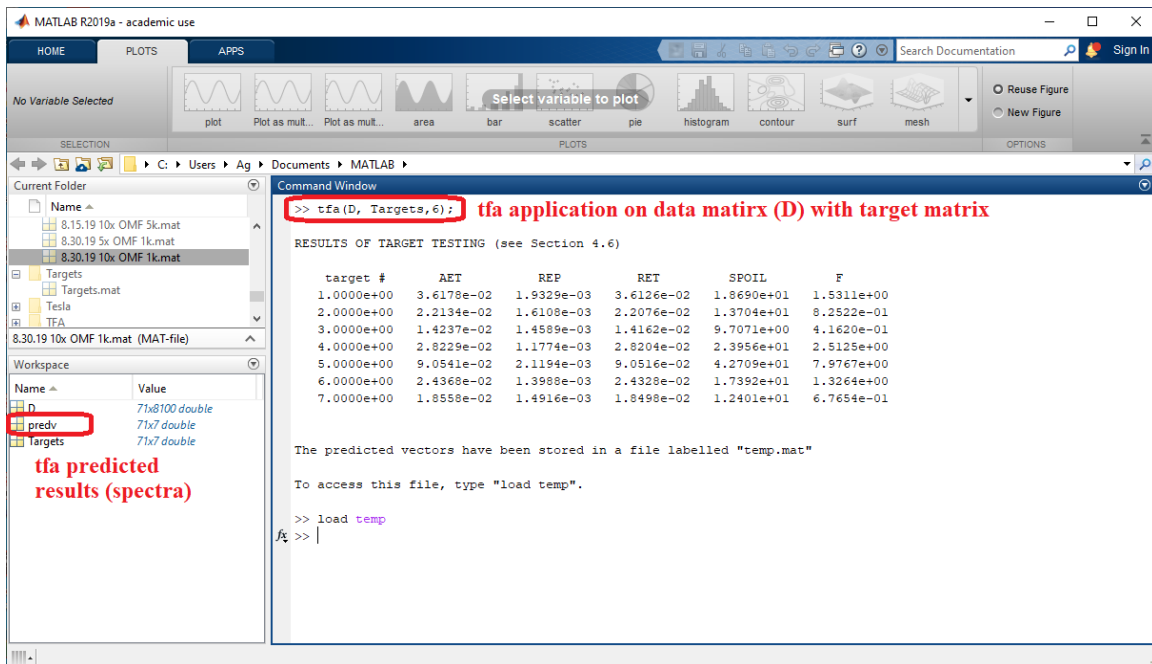


Figure A-14. Application of target factor analysis (tfa) on data matrix.

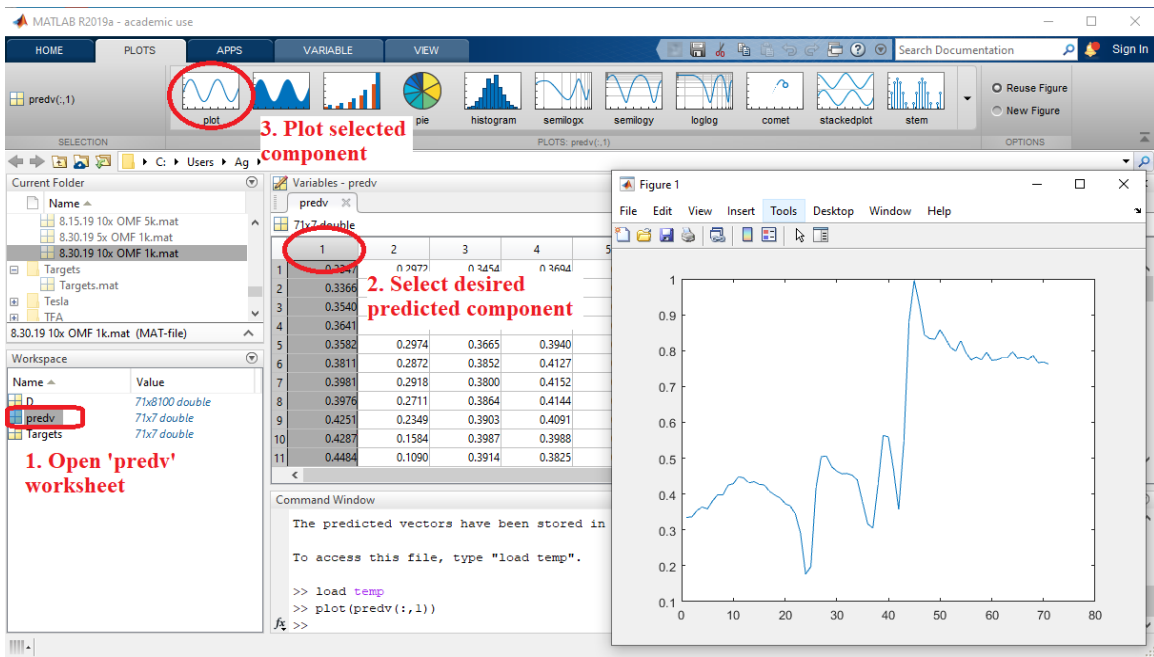


Figure A-15. Steps to visualize the decomposed abstract factors of 'u' matrix.

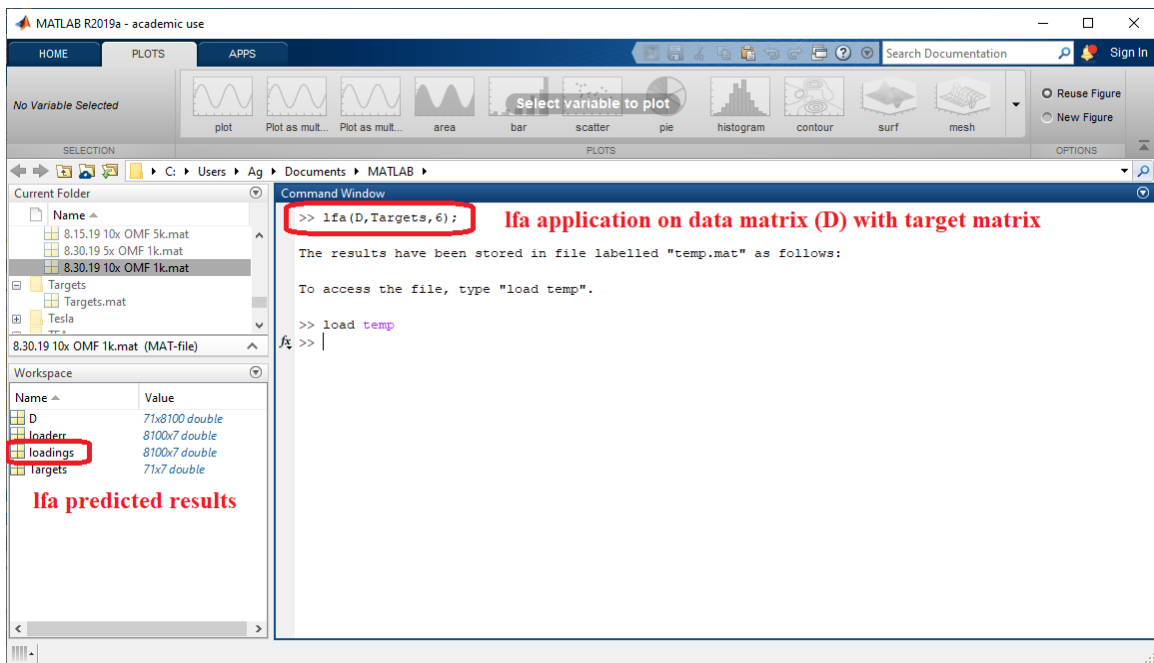


Figure A-16. Application of lfa on data matrix.

- 2) Load the lfa results by typing 'load temp' to add the predicted components to the Workspace. The predicted lfa spectra is contained in the 'loadings' file.
- 3) Open the 'loadings' worksheet, select the desired loading of component, and then, select 'create new variable from selection', as shown in Figure A-17.
- 4) Reshape the new loading component matrix using 'reshape' function, select the reshaped loadings matrix, and then, plot the component's distribution, as shown in Figure A-18.

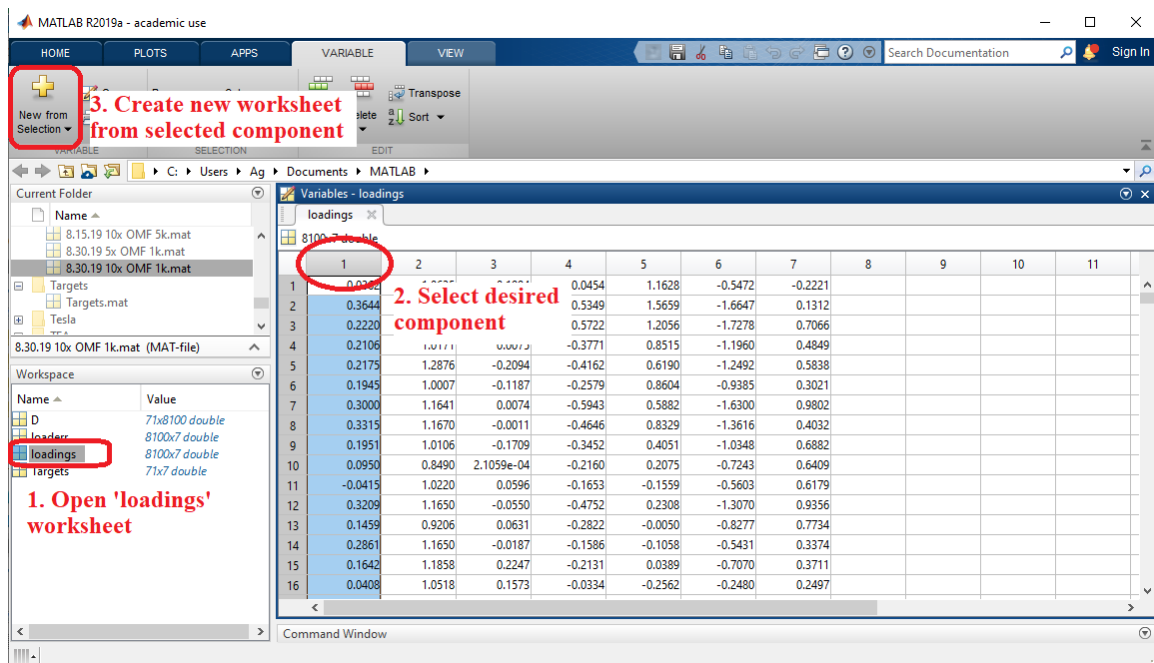


Figure A-17. Steps to select predicted components from 'loadings' matrix.

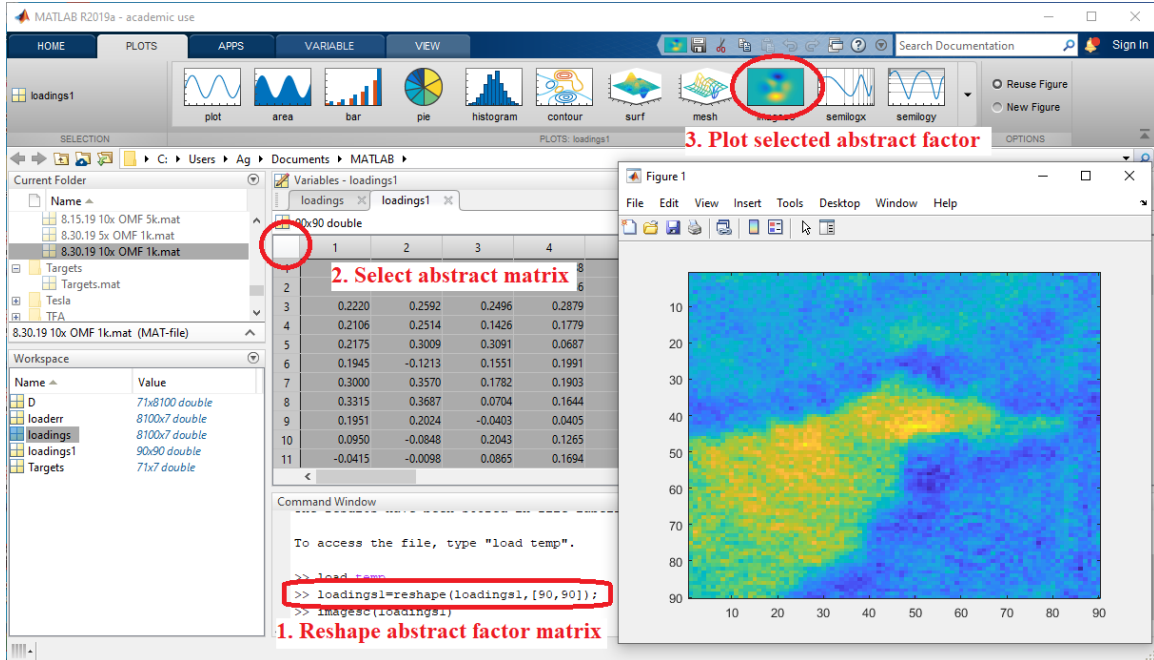
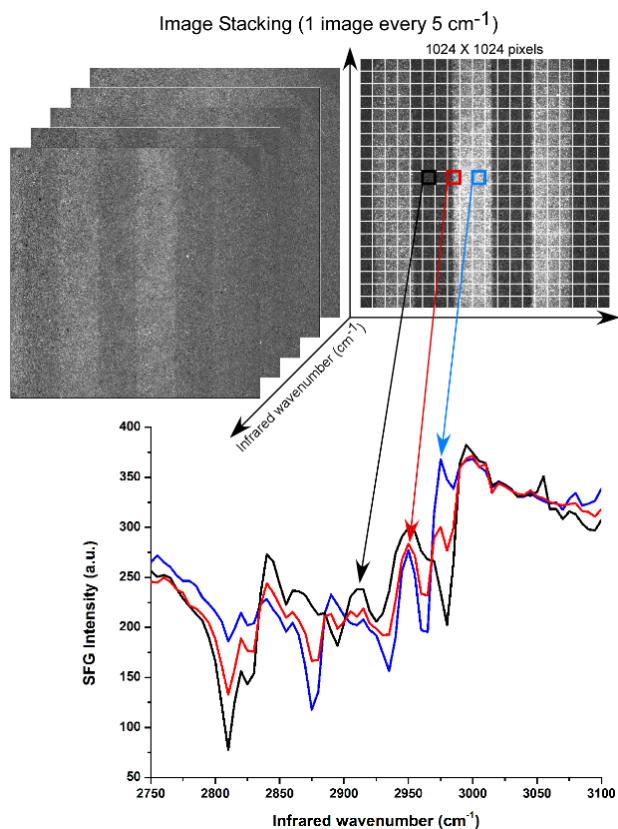


Figure A-18. Steps to produce component distribution map of selected component.

## **APPENDIX B**

# Sum Frequency Generation Imaging Microscopy of Self-Assembled Monolayers on Metal Surfaces: Factor Analysis of Mixed Monolayers.

## Supporting Information



**Figure B-1.** Illustration of image stacking and spectra extraction from 50-by-50 pixels ROIs. The SFG images are arranged into a stack according to decreasing IR wavenumber after which it is cut into user specific region of interest (ROIs) size and vibrational spectra is extracted from each respective ROI.

\* Reproduced in part with permission from *Anal. Chem.* **2019**, 91, 1269-1276, ©2019 American Chemical Society

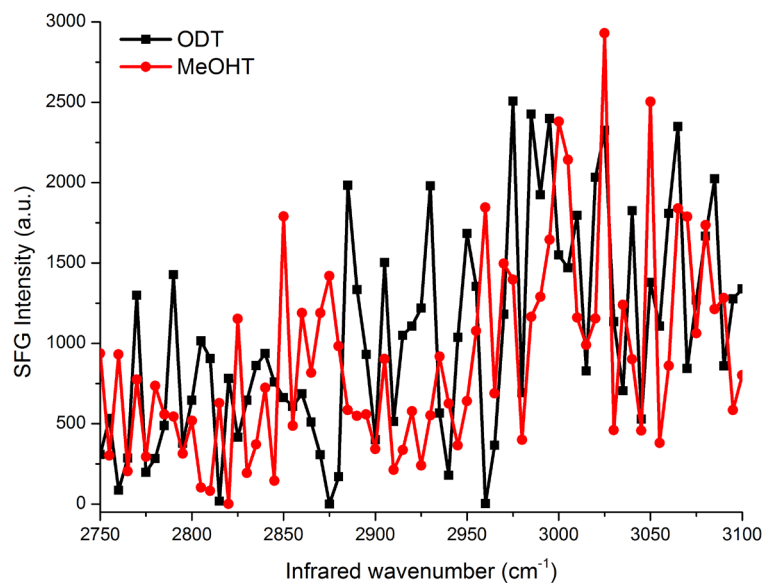


**Figure B-2.** SFG spectra of ODT and MeOHT extracted from 500 shots per image 6.5-by-6.5  $\mu\text{m}$  ROI.

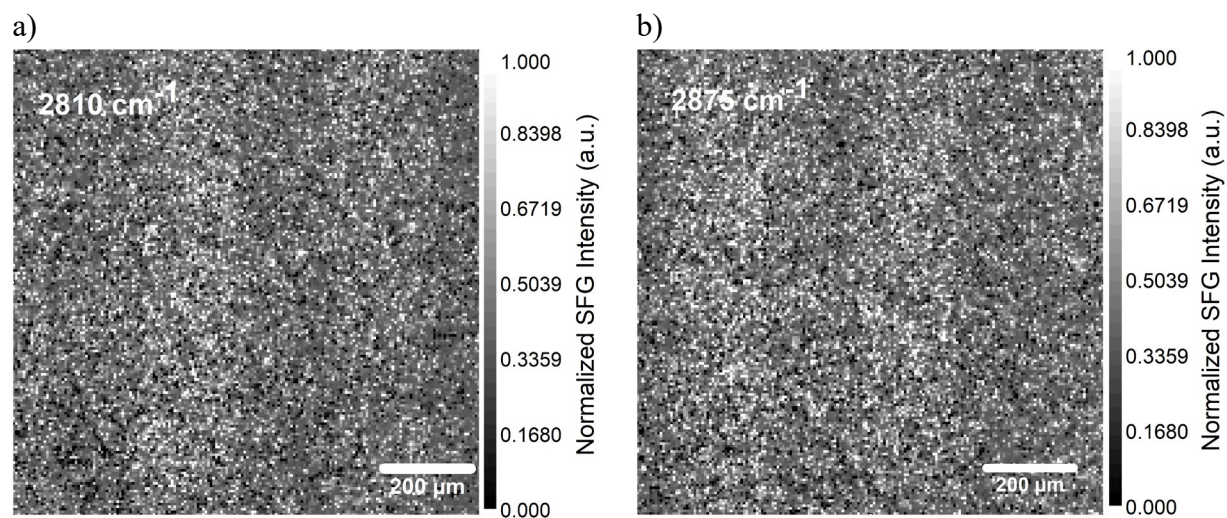


**Figure B-3.** 100 shot ODT—MeOHT sample SFG images at (a) 2810  $\text{cm}^{-1}$  and (b) 2875  $\text{cm}^{-1}$ .

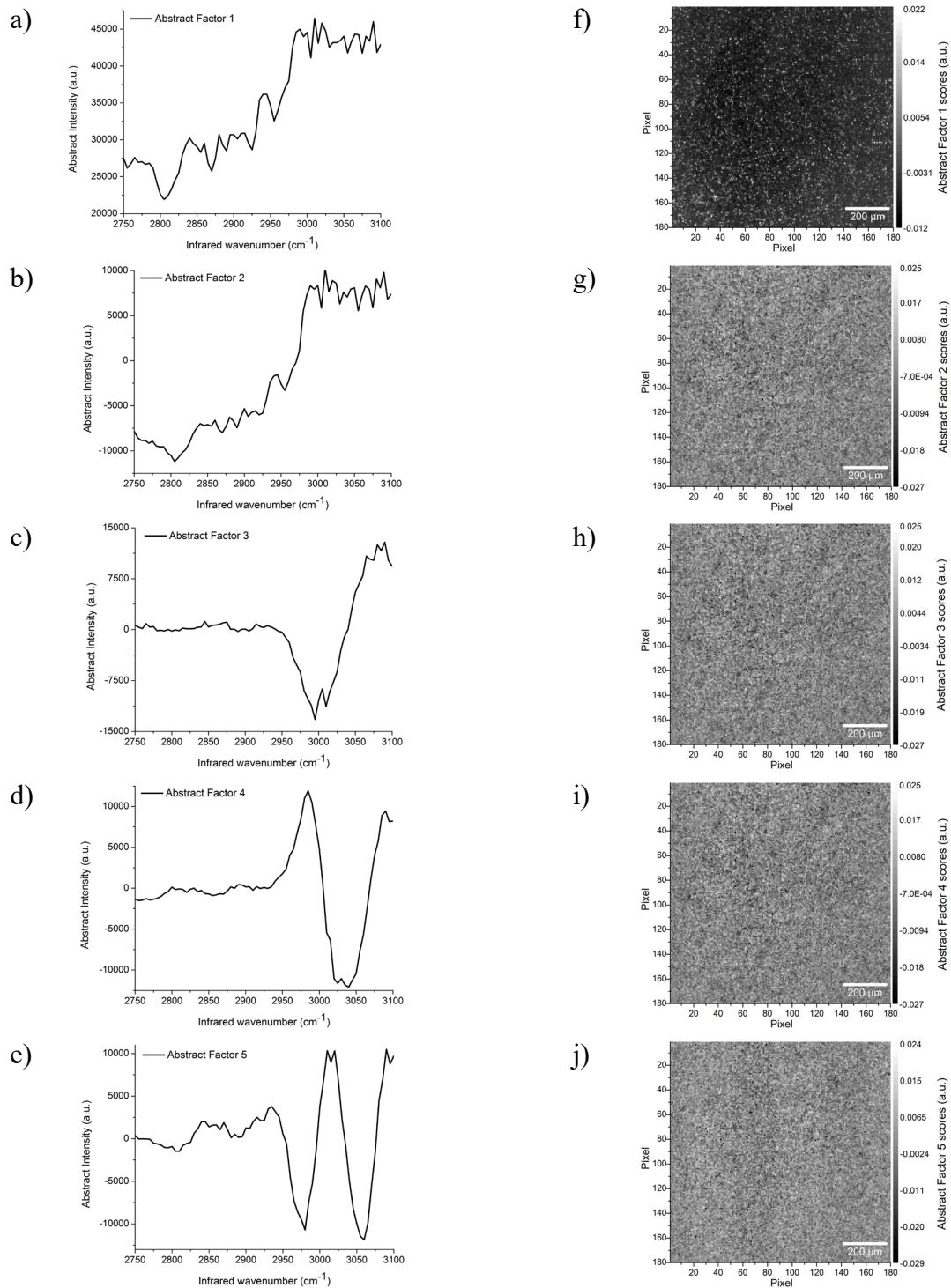


**Figure B-4.** First five abstract factors from row matrix (a-e) and column matrix (f-j) obtained by PFA of 100 shot ODT—MeOHT sample data matrix. The first two abstract factors resemble the combined average of the ODT and MeOHT SFG signal response on gold substrate with the beam profile. Abstract factors 3 through 5 resemble some change to the average spectra. None of the abstract factors resembles the difference spectra of ODT and MeOHT peak positions.

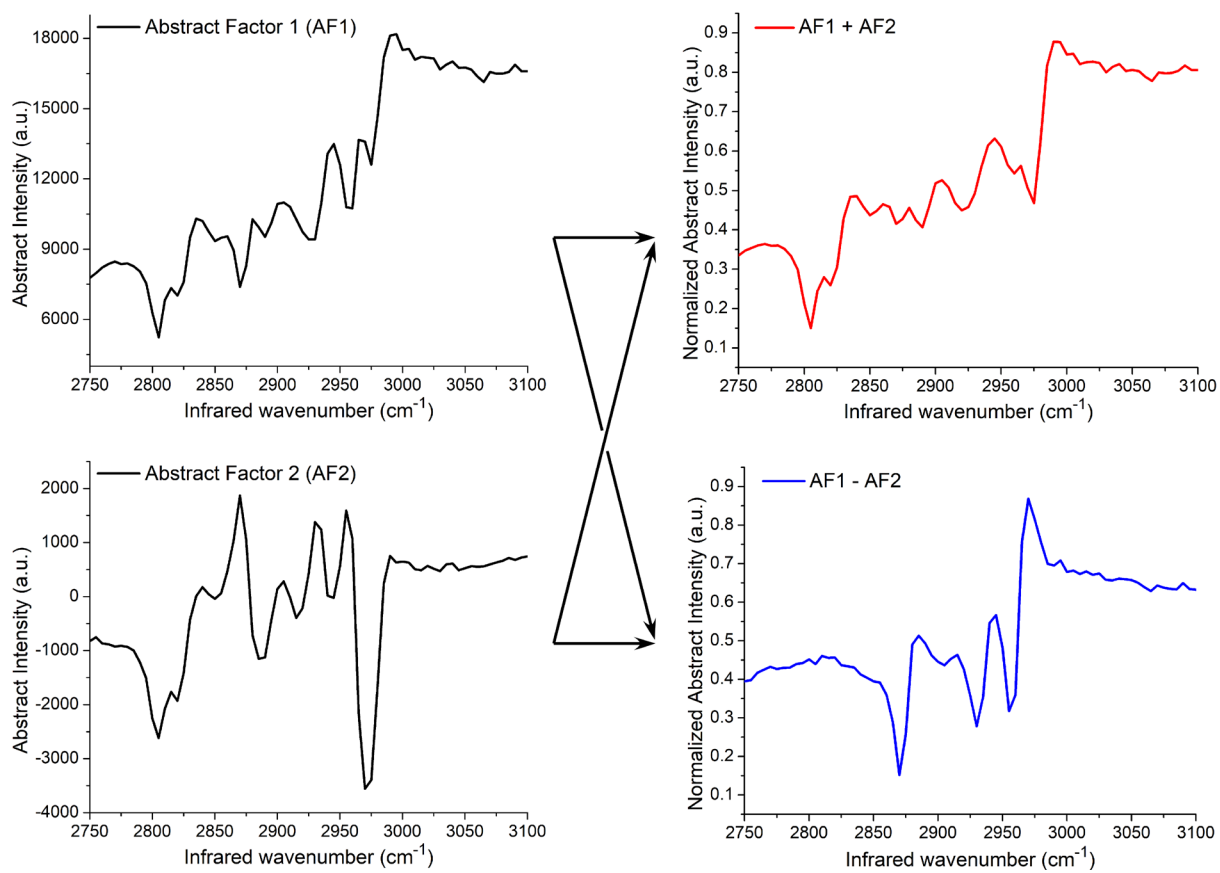


**Figure B-5.** Outline of target transformation of abstract factors into real factors by TFA. The real factors are obtained by adding the factors obtained by PFA using various weightings of the factors.<sup>1</sup>

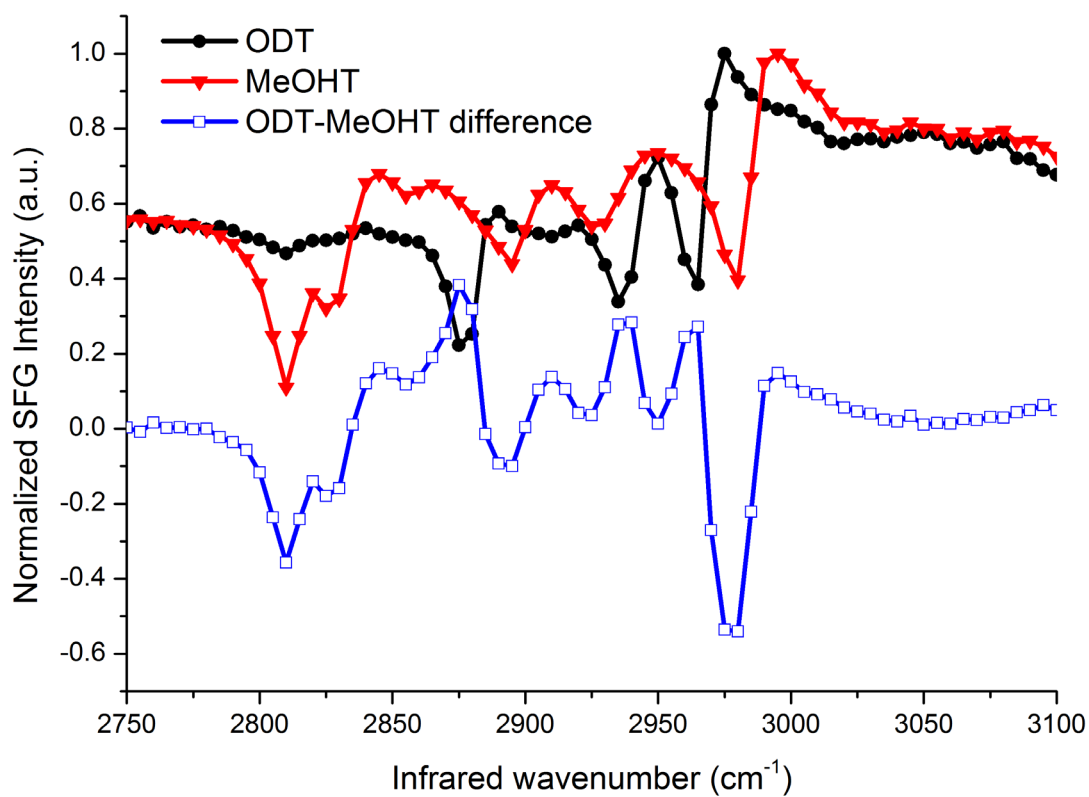


**Figure B-6.** Stamped ODT, backfilled MeOHT SFG spectra, and the difference of the two regions (backfilled – stamped).